# Structural Dynamics and Atomic Motion in Thin Films Studied by Ultrafast Electron Diffraction and Transient Optical Spectroscopy

by

DANIEL SALVATORE BADALI

B.Sc. (Honours), University of Toronto, 2011

M.Sc., Universität Hamburg, 2015

Dissertation submitted in partial fulfillment
of the requirements for the degree of
Doctor of Philosophy

Faculty of Mathematics, Informatics and Natural Sciences
Department of Physics
Universität Hamburg

2015
HAMBURG

Date of oral defense: November 24, 2015

The following reviewers recommend the admission of the dissertation:

Prof. Dr. R. J. Dwayne Miller

Max-Planck-Institut für Struktur
und Dynamik der Materie
CFEL (Bldg. 99), Room 2.099
Luruper Chausee 149
22761 Hamburg, Germany
Tel.: +49-(0)-40-8998-6200
Email: dwayne.miller@mpsd.mpg.de

Prof. Dr. Nils Huse

Max-Planck-Institut für Struktur
und Dynamik der Materie
CFEL (Bldg. 99), Room 2.131
Luruper Chausee 149
22761 Hamburg, Germany
Tel.: +49-(0)-40-8998-6266
Email: nils.huse@mpsd.mpg.de

Hiermit erkläre ich an Eides statt, dass ich die vorliegende Dissertationsschrift selbst verfasst und keine anderen als die angegebenen Quellen und Hilfsmittel benutzt habe.

I hereby declare, under oath, that I have written the present dissertation on my own and have not used other than the acknowledged resources and aids.

October 4, 2015 Daniel Salvatore Badali

This thesis is dedicated to my wife, Frans

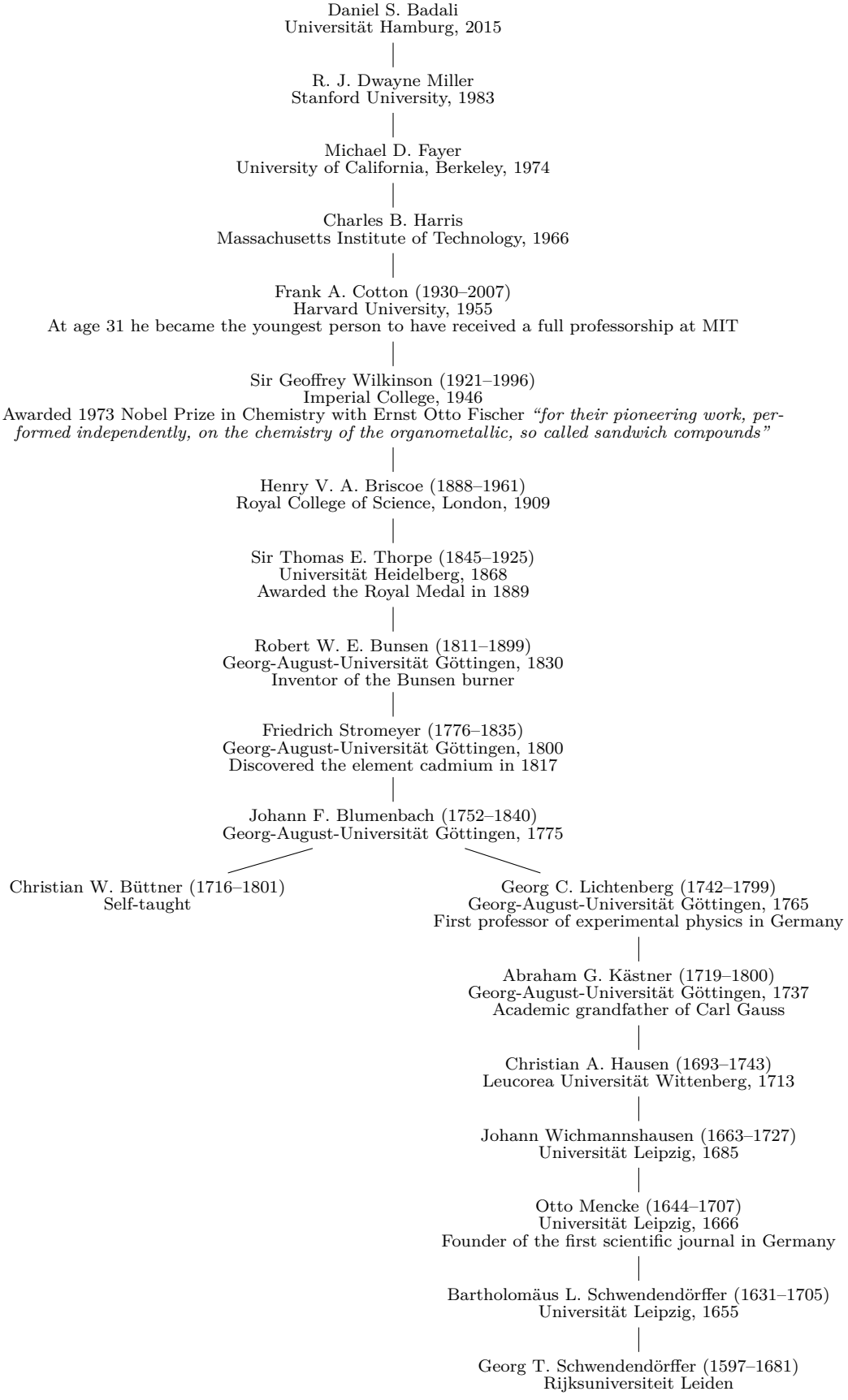
Daniel S. Badali
Universität Hamburg, 2015
R. J. Dwayne Miller
Stanford University, 1983
Michael D. Fayer
University of California, Berkeley, 1974
Charles B. Harris
Massachusetts Institute of Technology, 1966
Frank A. Cotton (1930–2007)
Harvard University, 1955
At age 31 he became the youngest person to have received a full professorship at MIT
Sir Geoffrey Wilkinson (1921–1996)
Imperial College, 1946
Awarded 1973 Nobel Prize in Chemistry with Ernst Otto Fischer "for their pioneering work, performed independently, on the chemistry of the organometallic, so called sandwich compounds"
Henry V. A. Briscoe (1888–1961)
Royal College of Science, London, 1909
Sir Thomas E. Thorpe (1845–1925)
Universität Heidelberg, 1868
Awarded the Royal Medal in 1889
Robert W. E. Bunsen (1811–1899)
Georg-August-Universität Göttingen, 1830
Inventor of the Bunsen burner
Friedrich Stromeyer (1776–1835)
Georg-August-Universität Göttingen, 1800
Discovered the element cadmium in 1817
Johann F. Blumenbach (1752–1840)
Georg-August-Universität Göttingen, 1775
Christian W. Büttner (1716–1801)
Self-taught
Georg C. Lichtenberg (1742–1799)
Georg-August-Universität Göttingen, 1765
First professor of experimental physics in Germany
Abraham G. Kästner (1719–1800)
Georg-August-Universität Göttingen, 1737
Academic grandfather of Carl Gauss
Christian A. Hausen (1693–1743)
Leucorea Universität Wittenberg, 1713
Johann Wichmannshausen (1663–1727)
Universität Leipzig, 1685
Otto Mencke (1644–1707)
Universität Leipzig, 1666
Founder of the first scientific journal in Germany
Bartholomäus L. Schwendendörffer (1631–1705)
Universität Leipzig, 1655
Georg T. Schwendendörffer (1597–1681)
Rijksuniversiteit Leiden

# Biography

Daniel Salvatore Badali was born on March 11, 1989, in Mississauga, Ontario, Canada to Catherine Badali (née Butler) and Salvatore Badali. Growing up with his brothers Matthew and Mark he participated in a number of extracurricular activities, such as athletics and music, although the highlight of these formative years was meeting his high school sweetheart Frans Terova, whom he married in 2012.

In 2011 Daniel obtained an Honours Bachelor of Science degree from the University of Toronto with a Specialist in Biological Physics and a Minor in Mathematics, graduating with High Distinction. During this time he participated in several research projects, including a stay at the prestigious Fields Institute for Research in Mathematical Sciences. For his undergraduate contributions to research he was awarded the inaugural 2011 Abdus Salam Award from the University of Toronto, in addition to the Moore Award in Physics and Petar Hein Award in Physics for academic success.

After spending a semester abroad in Germany, Daniel decided to pursue graduate studies at the University of Hamburg, in affiliation with the Max Planck Institute for the Structure and Dynamics of Matter and the Center for Free Electron Laser Science. In 2015 he was awarded a Master of Science degree (Sehr Gut). During this time he presented at a number of international conferences, and was awarded Best Oral Presentation at his symposium at the European Materials Research Society Spring Meeting. He additionally participated in various extracurricular activities, such as giving a public lecture at Hamburg's Nacht des Wissens (Night of Knowledge) and chairing the International Max Planck Research School Council.

Daniel intends to pursue his research career in the industrial sector.

# Acknowledgements

First and foremost I need to thank my incredible wife Frans. Without her encouragement and support I would have never moved to Germany in the first place, and so this thesis is dedicated to her. She had to deal with so much over the years; I think she knows more about physics and Germany bureaucracy that she (or anyone!) would ever want to know. This thesis is as much her milestone as it is mine.

The continuing support and love from my parents and brothers has been indispensable. Somehow my parents managed to survive with only seeing me a few times a year, although I think they enjoyed the excuse to adventure across the pond. Matthew never got tired of discussing physics or my research, and Mark made sure I realized there was more to life than science.

My supervisor R. J. Dwayne Miller has been an inspiration both scientifically and personally. By example he has shown me what it means to be a true scientist, and I greatly admire his endless passion and ability to motivate. Whenever my research was going slowly a short conversation with Dwayne would remind me why science is important and give me the encouragement to continue.

Speaking of inspiration, Régis Y. N. Gengler has been not only my mentor but my friend over the past years. He is an impressive scientist and I know that without his constant support I would not have gotten to where I am today.

Working with the members of Dwayne's group and the other students of IMPRS has been a blast, and I enjoyed our time outside of the lab as much as I did our time inside. I am also indebted to my collaborators and coauthors for their perseverance to seeing our work through to its end. In particular, I would like to thank Dr. Nicolas Erasmus for sharing the experimental data presented in Chapter 5.

Without the administrative support of the staff at CFEL, in particular Sonia Utermann, I would not have been able to navigate the treacherous waters of bureaucracy that led me here, so thank you all.

I would also like to thank Claudiu C. Gradinaru for first introducing me to the fascinating world of research. My scientific career would not have been launched without Claudiu's nurturing. He is always ready to support whatever adventure I decide to go on next, and I will never forget his continuing generosity.

Finally, I would like to acknowledge financial support from the Max Planck Society and the Natural Sciences and Engineering Research Council of Canada.

# Contents

# List of Figures

# List of Tables

# Abbreviations

**ASTRA** A Space Charge Tracking Algorithm

**BBO** $\beta$-Barium Borate

**CCD** Charge-Coupled Device

**CW** Continuous Wave

**FWHM** Full-Width at Half-Maximum

**GO** Graphene Oxide

**MCP** Microchannel Plate

**NMP** N-Methyl-2-Pyrrolidone

**rGO** Reduced Graphene Oxide

**SNR** Signal-to-Noise Ratio

**TEF** Transient Electric Field

**UED** Ultrafast Electron Diffraction

**UV** Ultraviolet

# Nomenclature

| | |
|---|---|
| $\Lambda_{\text{el/inel}}$ | elastic/inelastic mean free path |
| $\|\cdot\|_2$ | $\ell^2$-norm; if $\boldsymbol{x}$ is a vector with $n$ elements, then $\|\boldsymbol{x}\|_2 = \sqrt{\sum_{i=1}^{n} \|x_i\|^2}$ |
| $\mathbb{E}(\cdot)$ | Expectation value; if a random variable $X$ has a probability density function $f_X(x)$, then $\mathbb{E}(X) = \int_{-\infty}^{\infty} x f(x)\,\mathrm{d}x$ |
| $\mathcal{N}(x\|\mu, \sigma^2)$ | Normal distribution with mean $\mu$ and variance $\sigma^2$ $\mathcal{N}(x\|\mu, \sigma^2) = (2\pi\sigma^2)^{-1/2} \exp\left[\frac{(x-\mu)^2}{2\sigma^2}\right]$ |
| $\text{Poisson}(x\|k)$ | Poisson distribution with parameter $k$ $\text{Poisson}(x\|k) = k^x e^{-k}/x!$ |
| $\xi_\perp$ | transverse coherence length |
| $c = 299,792,458\,\text{m/s}$ | speed of light |
| $h = 6.626 \times 10^{-34}\,\text{kg}\,\text{m}^2/\text{s}$ | Planck's constant |
| $k_\text{B} = 1.38 \times 10^{-23}\,\text{kg}\,\text{m}^2\,\text{s}^{-2}\,\text{K}^{-1}$ | Boltzmann's constant |
| $m_e = 9.109 \times 10^{-31}\,\text{kg}$ | rest mass of an electron |
| $q = 1.602 \times 10^{-19}\,\text{C}$ | elementary charge |

# Abstract

Because of their unique structure, thin films provide an unprecedented view into the fundamental physics of a two-dimensional world. There is also an enormous demand for such materials in applied fields, and many thin films find use as platforms for device applications.

To further our understanding of such materials, this thesis investigates the properties of thin films on the time- and length-scales associated with atomic motions. To do this, two techniques with access to these extreme scales were used: transient spectroscopy, and ultrafast electron diffraction. Transient spectroscopy is equipped with the temporal resolution required to witness chemical dynamics; this fact is demonstrated in this thesis by an experiment which probes the ultrafast formation of graphene from an oxidized precursor. However, only ultrafast electron diffraction has the spatial resolution required to watch atoms move in real time.

Thin films add another layer of complexity to such already challenging experiments due to the fact that they typically have a minimal response to optical and electron probes as a result of their low-dimensionality. To address this issue, this thesis introduces several novel design principles in order to optimize ultrafast electron diffraction for studying thin films and monolayers. This culminates in the construction of a low-energy electron diffractometer, the first of its kind in the world. The successful demonstration of this machine to study the transient electric fields produced near a laser-irradiated graphene surface confirms that the electron diffraction can interrogate the two-dimensional world.

However, this device, as with all conventional ultrafast electron diffractometers, is poorly-suited to investigate irreversible reactions, a restriction that has recently been lifted with the advent of ultrafast streak cameras. Because streaking is a fairly new technique, there are many open questions as to how to interpret the streaked diffraction data. In this thesis, ultrafast streaking is put on firm theoretical grounds through the development of a new analysis approach that allows the entire time-dependent diffraction pattern to be recovered from a single streaked diffraction image. This development enables access to the entire range of possible thin film dynamics, both reversible and irreversible.

# Zusammenfassung

Wegen ihrer einzigartigen Struktur bieten dünner Schichten eine noch nie da gewesenen Einblick in der Grundlagenphysik einer zweidimensionalen Welt. Es gibt auch eine enorme Nachfrage nach solchen Materialien in angewandter Felder und viele dünne Schichten finden Verwendung als Plattformen für Elektronik.

Um unser Verständnis solcher Materialien weiter, untersucht diese These die Eigenschaften dünner Schichten auf die Zeit- und Längenskalen mit atomaren Bewegungen verbunden. Hierzu wurden zwei Techniken mit Zugang zu diesen extremen Skalen verwendet: transient Spektroskopie und ultraschneller Elektronenbeugung. Transiente Spektroskopie hat die zeitliche Auflösung benötigt, um chemische Dynamik zu beobachten; Dies wird in der vorliegenden Arbeit durch ein Experiment veranschaulicht das ultraschnelle Bildung von Graphen aus eine oxidierte Vorläufer untersucht. Allerdings hat nur die ultraschnelle Elektronenbeugung die räumliche Auflösung, Atome in Echtzeit bewegen zu sehen.

Dünnschichten erschweren solche bereits anspruchsvolle Experimente, dass sie eine kleine Reaktion auf optische haben und Elektron-aufgrund ihrer niedrigen-Dimensionalität Sonden. Um dieses Problem zu beheben, führt diese These mehrere neue Design-Prinzipien zur Optimierung der ultraschnellen Elektronenbeugung Studium von Dünnschichten und Monolayers. Dies gipfelt in den Bau von Niedrigenergie-Elektron-Diffraktometer, das erste in der Welt. Die erfolgreiche Demonstration dieser Maschine die transiente elektrische Felder produziert in der Nähe ein Laser bestrahlt Graphen-Oberfläche zu studieren bestätigt, dass die Elektronenbeugung die zweidimensionale Welt befragen kann.

Diese Maschine ist jedoch schlecht untersucht irreversible Reaktionen, ein Problem, das vor kurzem mit der Erfindung des ultraschnellen Streakkameras gelöst worden ist. Da Streifen eine neue Technik ist, gibt es viele offene Fragen zum gestreift Beugung Daten interpretieren. In der vorliegenden Arbeit ist ultraschneller Streifen setzen auf gute theoretische Gründe durch die Entwicklung eines neuen Analyse-Ansatzes, mit der das gesamte zeitabhängige Beugung Muster von einem einzigen gestreift Beugung Abbild wiederhergestellt werden kann. Diese Entwicklung ermöglicht den Zugriff auf die gesamte Palette der möglichen Dünnschicht-Dynamik, sowohl reversible und irreversible.

# 1. Transient Dynamics in Thin Films

> *"In research, if you know what you are doing, then you shouldn't be doing it."*
>
> — Richard W. Hamming

## 1.1. The Information Age and Science's Fascination with the Two-Dimensional World

The first electronic computer occupied over $150\,\mathrm{m}^2$ and cost over $\$\,6$ million (ref. 1), whereas modern microprocessors can be as small as $350\,\mathrm{mm}^2$ (ref. 2) and cost an average of $\$\,6$ (ref. 3). This six order of magnitude decrease in both size and cost is an impressive indication of the advancement made toward the miniaturization of technology. In an apt observation, Gordon Moore, of the eponymous law expressing that the number of transistors on a microchip doubles every two years, stated[4]

> *In terms of size you can see that we're approaching the size of atoms which is a fundamental barrier, but it'll be two or three generations before we get that far.*

While the timescale of manufacturing atomically thin electronics might be a few generations, materials science research has been toying with this fundamental limit for the last decade. This emphasis on materials with reduced dimensionality has been driven by a combination of purely academic interest and the miniaturization of technology; thus the information age is partly responsible for ushering in the era of the thin film: materials ranging from the smallest possible thickness (one atomic monolayer), to stacks of a few hundreds of such monolayers.

The fascination with thin films and monolayers has arisen in the wake of the discovery of graphene[5], the first truly two-dimensional material. Graphene, which will be described in more detail in Chapter 2 and will appear several times throughout this thesis, is only one carbon atom thick, or roughly $0.000\,000\,000\,3\,\mathrm{m}$. In addition to serving as a playground for fundamental physics due its multitude of bizarre properties[6–10], graphene has shown the potential to revolutionize many aspects of modern technology; Jonathan Coleman, one of the world leaders in the production of two-dimensional materials, went as far as saying, "For every application you can think of, there will be a two-dimensional material for you" (ref. 11). Moreover, graphene is seen as a prototype for other two-dimensional materials; a remarkable demonstration of this was the identification of over 550 types of ultra-thin films and "nanosheets" that can be synthesized with the same techniques developed for graphene[12].

These materials and other like them are ready to serve as the fundamental building blocks for future electronics and micro-technology.

The promise and usefulness of such materials is due to their unique two-dimensional structure. Dimensionality has long been a muse to physicists, stemming from the fact that many systems can be analyzed and solved in a reduced one-dimensional framework[13], to the seemingly unbounded multitude of dimensions in contemporary string theories (the most mature theories sport upward of 20 dimensions[14]). From a materials science point-of-view, the dimensionality* of a system profoundly influences its physical and electronic properties. The allotropes of carbon are a canonical example, with the properties in zero dimensions ($C_{60}$ and the other round fullerenes), one dimension (nanotubes), two dimensions (graphene), and three dimensions (graphite and diamond), all being vastly different[15]. Fig. 1.1 illustrates how the dimension of the allotrope can be controlled through the manipulation of graphene.

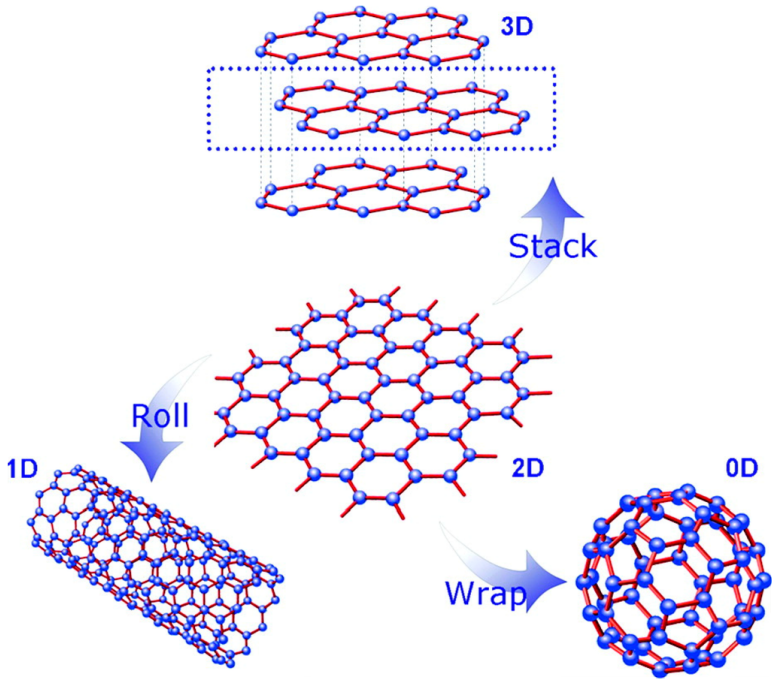


Figure 1.1.: *Illustration of how allotropes of carbon with varying degrees of translational symmetry (also known as dimensionality) can be constructed from graphene. Reprinted with permission from ref. 16. Copyright © 2012 American Chemical Society.*

While adding dimensions has previously been a purely academic exercise, the techniques developed for graphene have made reducing dimensionality experimentally accessible and a means of generating exotic behaviour from many materials. Inspired by the exciting potential and fascinating physics of thin films and monolayers, this thesis strives to further the understanding of such materials by delving deeper into this two-dimensional world.

* In this context, dimensionality refers to the number of perpendicular axes along which possess translational symmetry.

## 1.2. Faster Than Fast and Smaller Than Small: Transient Structural Dynamics

While thin film research still has many exciting venues to explore, the particular focus of this thesis will be on the atomic motions and rearrangements that are associated with chemical reactions and out-of-equilibrium dynamics. The motivation for this endeavour is that chemical reactions have long been a sort of "black box", where the input (reactants) and output (products) are known, but what happens in-between is a mystery. While treating reactions this way has led to some incredible results, Science has begun a quest to have look inside this black box. This field is known as *transition state chemistry*, and is well motivated by this statement by Nobel laureates John Polanyi and Ahmed Zewail[17]:

> *The transition state is neither one thing, namely, chemical reagents, nor the other, reaction products. Instead it illustrates the mystical event of trans-substantiation.*

While this is expressed rather whimsically, the authors are correct to be in awe. Transition states have eluded scientists for years, and it is just recently that technology has become sufficiently advanced to study them. The challenge with this venture lies in the inherent properties of chemical reactions. Put generally, chemical reactions are:

**Small:** Typical crystalline unit cells are on the order of 1 – 10 angstroms ($1\,\text{Å} = 10^{-10}$ m) in size. However, the structural changes that accompany a chemical reaction often involve the movement of a few atoms, and are associated with atomic displacements of $< 0.1\,\text{Å}$.

**Fast:** Transition states often exist for a few picoseconds, and some as short as a few tens of femtoseconds ($1\text{ fs} = 10^{-15}$ s).

These are extreme spatial and temporal scales, and are so beyond what we experience in our everyday life that it is challenging to fully appreciate them. To put the spatial scale into perspective, consider the fact that observing a $1\,\text{Å}$ change from a meter away is akin to standing on the moon and watching someone on Earth wave their hand. And while femtosecond lasers have become commonplace in laboratories all over the world, it is humbling to think that one second contains ten times more femtoseconds than the total number of years the entire universe has ever existed. It is an impressive feat of technology that such extreme scales are accessible at all.

To investigate such atomic dynamics in thin films, these challenges are compounded with the fact that thin films are notoriously difficult to study, because they:

1. are generally difficult to produce

2. are fragile to handle

3. have minimal response to traditional probes (i.e. they are almost optically transparent, they are thin enough that they hardly scatter radiation or matter waves, etc.)

4. are extremely sensitive to the surrounding environment (i.e. prone to adsorption)

Because of this, there is a need to develop new tools to approach this problem: a technique which has access to the ultrafast and ultrashort scales associated with chemical reactions, as well as sensitivity to extremely thin films.

## 1.3. Photons and Electrons as Ultrafast Probes

To capture a transient event, the probing device must have a temporal resolution faster than the timescale of the event. The consequences of this are easily seen in Fig. 1.2, which shows the same scene of a fountain photographed with two different exposure times. The left image was taken with a slow shutter speed (corresponding to a long exposure time), and the right image was taken with a fast shutter speed (corresponding to a short exposure time). It is evident that the left image was taken with insufficient temporal resolution, since the dynamics of interest (in this case, the falling water droplets) are blurred. This makes it impossible to trace out the trajectory of a single water droplet.

Figure 1.2.: *Photograph of fountain taken with slow shutter speed/long exposure time (left) and fast shutter speed/short exposure time (right)*[18]

In light of the discussion of the characteristics of atomic motions, time-resolved probes of

such dynamics must possess sub-picosecond temporal resolution. Fortunately, the invention of lasers capable of producing short bursts of light with durations on the femtosecond timescale led to the development of the workhorse of ultrafast measurements, the celebrated pump-probe method. In this technique, the dynamics of interest are initiated with a laser pulse that "pumps" the sample. This is a versatile way of perturbing the sample, since the pump laser can be used to deposit heat, initiate lattice vibrations, or selectively exciting an electronic transition, each of which can be carefully controlled by the choice of pump intensity, wavelength, size, and duration. At a later time, another laser pulse "probes" the sample and records the absorption properties of the sample. The power of this approach is that since the probe is has a duration on the order of femtoseconds, it only takes a "snapshot" of the sample at a specific time after the dynamics were initiated; therefore, by varying the time delay between the arrival of the pump and the probe, the time-dependent absorption of the sample can be traced through the entire dynamics. An entertaining illustration of this pump-probe technique is shown in Fig. 1.3, which shows Étienne-Jules Marey's famous 1894 experiment of taking a series of sequential photographs of a falling cat. In this case, the "pump" is the action of dropping the cat, and the "probes" are the photographs. The difference between this and the pump-probe experiments that are discussed in this thesis is that there is one pump event for each probe; that is, the cat would be dropped and then a single photograph would be taken. Then, the cat would be dropped again and, at a later time, another photograph would be taken, and so on.

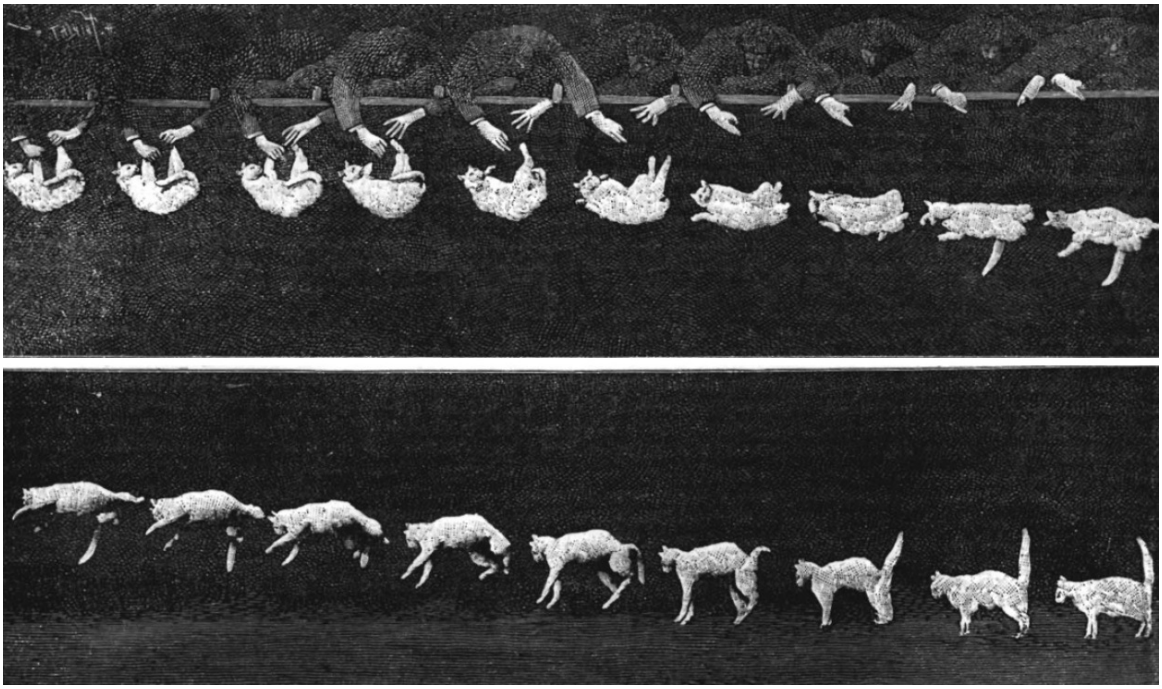

Figure 1.3.: *Images of a falling cat captured with chronophotography in 1894 (ref. 19)*

From an experimental point-of-view, there is the added benefit that both the pump and the probe pulses can be derived from the same laser source, and so this technique is completely insensitive to timing jitter. However, there are several limitations, the most severe being that transient absorption measurements contain no structural information. So while they are

well-suited for investigating the timescales associated with various dynamics in thin films, they lack the spatial resolution to track atomic trajectories.

The inadequacy of transient spectroscopy as a structural probe has led to the development of Ultrafast Electron Diffraction (UED), a related pump-probe method that uses short electron pulses as the probe. The required sub-angstrom spatial resolution comes from Louis de Broglie's 1924 prediction that all moving particles, including electrons, exhibit wave-like behavior[20], with wavelengths given by:

$$\lambda = \frac{h}{p} \tag{1.1}$$

where $h = 6.626 \times 10^{-34}\,\mathrm{kg\,m^2/s}$ is Planck's constant and $p$ is the particle's momentum. By accelerating electrons to extremely high momenta ($p > 10^{-23}\,\mathrm{kg\,m/s}$), the electrons can exhibit sub-angstrom wavelengths. The UED technique is additionally equipped with the desired sub-picosecond temporal resolution; much like with transient spectroscopy, this is again due to femtosecond lasers, since electrons pulses that are the same duration as laser pulses can be produced via the photoelectric effect by irradiating a metal cathode[21].

Although many recent reviews exist[22–24], it is beneficial to give a brief introduction to UED for completeness. In such experiments, a femtosecond laser is divided into two optical lines: one for the pump and the other for probe (analogous to optical pump-probe). The pump line is used to optically excite the sample, whereas the probe is sent to an electron gun to produce an electron pulse. A conventional electron gun consists of several components, some of the most important of which are a metallic photocathode (typically gold or copper) that is held at a negative voltage and a grounded anode plate with a small hole in its center through which the electrons pass (see Fig. 1.4). The gap between the cathode and anode results in high electric fields which accelerates the electrons to the required momentum. Both the electron gun and the sample are contained within a vacuum chamber, and the diffraction pattern is collected by an imaging detector. A detailed introduction into the experimental details of UED experiments will be presented in Chapter 3. In the same way temporal resolution is obtained in transient absorption measurements, by changing the delay between the pump and the probe, the diffraction pattern can be recorded at different time points during the dynamics, making it possible to record "movies" in a stroboscopic fashion. By comparing the locations and intensities of the diffraction peaks at each time point, the exact structural dynamics of the reaction can be determined with the resolution of the electron pulse duration. This technique therefore enables atomic motions to be recorded in real time with high spatial and temporal resolution.

The energy of the probe electrons in the UED setup ultimately determines what thickness of material the setup will be sensitive to. As will be argued extensively in Section 3.3.1, the ideal acceleration voltage to study thin films and monolayers is 1 – 10 kV. This is a previously unexplored energy regime for UED systems, which typically operate in the 50 – 200 kV range[21–24], and so existing machines are not optimized for exploring structural dynamics in thin films. To this end, a large portion of this thesis will be dedicated to the

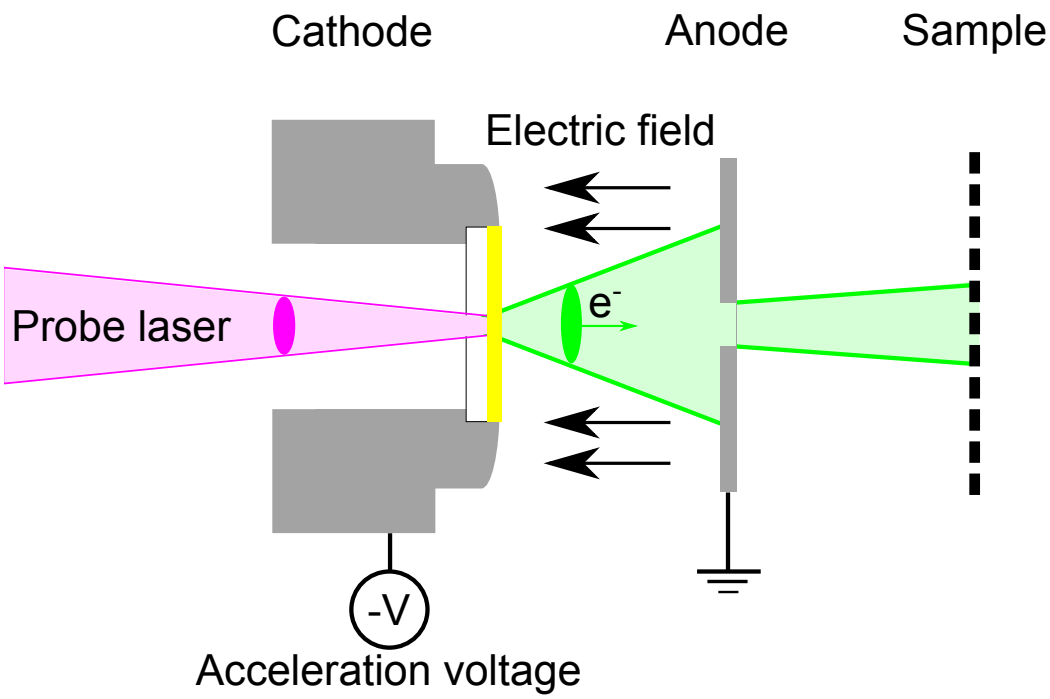


Figure 1.4.: *Cross-section through a typical ultrafast electron gun design. Light irradiates a cathode and produces electrons via the photoelectric effect, which are then accelerated by an electric field. At the exit of the gun, the electrons pass through a small aperture in the anode plate and propagate towards the sample.*

development and demonstration of "low-energy" UED, designed specifically to study thin films. A photograph and schematic of the novel UED setup, including all the supporting optics, is shown in Fig. 1.5.

There is an inherent challenge to working with short electron pulses: because electrons are negatively charged, dense bunches of them tend to expand due to space-charge effects, which degrades the temporal resolution of the experiment. This is particularly pronounced when working in the low-energy regime, because both longitudinal and transverse beam growth due to space-charge effects scales as $(1-\beta)^{-3/2}$ (ref. 25), where $\beta$ is the ratio of the electrons' speed to the speed of light. Because $\beta$ is proportional to the square root of the acceleration voltage, low-energy electrons suffer significantly from unwanted space-charge effects. Because of this, adapting the UED technique to study thin films requires some particular design considerations that are absent in traditional setups.

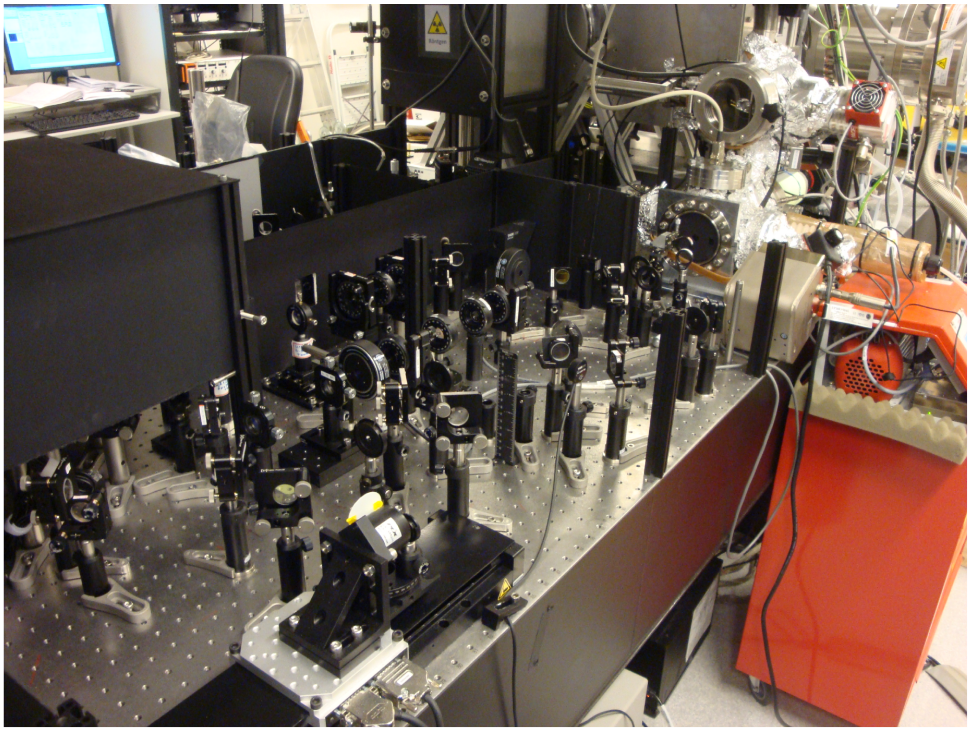

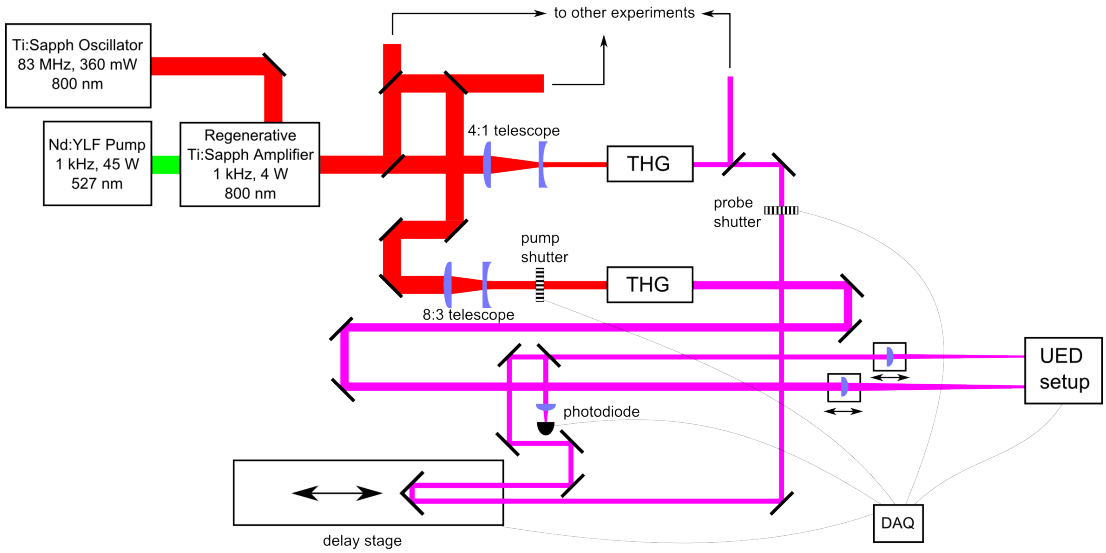


Figure 1.5.: *Photograph (top) and simplified schematic (bottom) of the optics associated with the ultrafast electron diffraction (UED) setup used in this thesis. THG: third harmonic generation, DAQ: data acquisition*

## 1.4. Contributions of This Thesis

This thesis is combined of several contributions which work toward the understanding of structural dynamics in thin films and the development of suitable tools to examine them. Each chapter is intended to motivate the next; Chapter 2 starts by using transient spectroscopy to study the ultrafast production of graphene from an oxidized precursor. While the timescale and the different species involved with the reaction are identified, very little can be inferred about the structural changes that occur. This is because, as stated above, structural information is generally inaccessible to spectroscopic measurements in the visible domain.

This leads to Chapter 3, which comprises of the bulk of the work presented in this thesis, and introduces a novel tool for measuring structural dynamics of thin films. By limiting the acceleration voltage to the low-energy regime (1 – 10 kV) in a compression-less UED system, it is shown that the sensitivity to films of thickness $< 10$ nm can be achieved while maintaining sub-picosecond temporal resolution.

Chapter 4 presents an application of the low-energy UED technique, where 6 kV electrons are used to probe the transient electric fields produced by photoionized graphene. In addition to gleaning some insight into the ionization process, this experiment serves to validate the new low-energy UED design and demonstrate its utility for investigating thin films and monolayers.

Returning back to the contents of Chapter 2, it would be ideal to be able to use UED to study the ultrafast production of graphene. However, the UED technique, in the pump-probe paradigm that is presented in Chapter 3 and Chapter 4, is only suitable for reversible reactions (those which can be repeated several thousands of times in a row without damaging or modifying the sample). This is an issue that severely restricts the types of thin films that can be studied, additionally excluding the experiment in Chapter 2. To mitigate this, Chapter 5 introduces the recently established technique of ultrafast streaking of diffraction patterns, which allows an entire molecular movie to be recorded with a single probe pulse. The contribution of this thesis to this technique is to develop the appropriate theory and analysis tools that have thus far been missing.

Within the framework of these chapters, this thesis strives towards the development of tools capable of examining structural dynamics in thin films. While the content of this thesis can be seen as progress towards this goal, there are many potential experiments that could contribute to the further understanding of the groundwork laid here. For instance, it would be worth demonstrating that a low-energy setup capable of the streaking is feasible, to open up the possibility of exploring irreversible dynamics in thin films. The ultrafast production of graphene, would be a good first potential candidate. This experiment, and others like it, would encourage Science to delve into the two-dimensional world, providing a deeper understanding of the properties and prospective uses of thin films.

# 2. The ultrafast chemistry of graphene oxide: Revealing the process behind photoreduction*

*"Satisfaction of one's curiosity is one of the greatest sources of happiness in life."*

— Linus Pauling

## 2.1. Introduction

A single word can encompass millions of dollars of research funding, thousands of publications, hundred of careers, and even a couple of Nobel prizes. This word is: *graphene*. Since its discovery just over a decade ago[5] graphene has been championed as having the potential to revolutionize almost every aspect of modern technology, and accordingly it is at the forefront of cutting-edge fundamental science. Such widespread uses has garnered graphene the attention of the international community, from both scientists and non-scientists.

The reason for all the attention is the plethora of unusual properties that graphene exhibits as a result of its unique two-dimensional structure. Graphene consists of carbon atoms arranged in a planar "honeycomb" hexagonal lattice as shown in Fig. 2.1 A, and the resulting electronic structure shows linear dispersion near the K points, which is uncommon in most solid state materials. This gives rise to several strange quantum effects, such as the quantum Hall effect[27,28] and the presence of massless Dirac fermions[29]. It addition, its unique structure equips it with a wide range of peculiar electrical[5,6,30], optical[31], and structural properties[32]. A summary of these and other exciting features can be found in the many reviews that have been written about graphene[6–10].

Because graphene is suitable for a wide-range of real-world applications, there is a need for rapid, facile, green, robust, and efficient methods to meet the industrial demands for high quality graphene. There are currently several production methods that are commonly used:

**Mechanical Exfoliation** This technique, also known as the "Scotch tape" method due to its historical implementation, involves the use of an adhesive tape to cleave bulk graphite

* Portions of this chapter were previously published as R. Y. N. Gengler, D. S. Badali *et al.*, *Nat. Comm* 2013 (ref. 26), and have been reproduced with permission. Copyright is held by Nature Publishing Group.

into few-layer graphene by repeatedly peeling off the top layer[5,33].

**Chemical Vapor Deposition (CVD)** In general, CVD refers to the exposure of a substrate to gaseous compounds which decompose on the surface to grow a thin film. Although there are several ways to achieve this for graphene, the most popular is the exposure of a nickel or copper substrate to a gaseous mixture containing $CH_4$ at about 1000 °C (ref. 34).

**Epitaxial Growth** Similar to CVD, epitaxial growth also involves the formation of graphene directly on a surface. It is quite straight forward, and high quality graphene can be obtained by simply heating and cooling a single crystal of SiC (ref. 35, 36).

**Reduction from Graphene Oxide (GO)** GO is an oxidized form of graphene, where the carbon atoms are arranged in the traditional honeycomb lattice, but oxygen-containing moities are present in the form of defects. There are several methods in which the oxygen can be removed, resulting in the recovery of graphene. This approach is discussed in detail below.

While each of these has its advantages and disadvantages (see Table 2.1), the final option, reduction from GO, shows significant promise. This is mainly due to the fact that GO, unlike graphene, is soluble in water, which opens the door to a number of established handling techniques from the field of solution chemistry. Additionally, GO can be readily prepared in large quantities, in a controlled fashion, by several techniques. The most prominent are methods due to Hummers and Offeman[37], and Staudenmaier[38], where a strong acid is used to simultaneously exfoliate and oxidize graphite flakes. It is the reduction of GO that will be the topic of this chapter.

Table 2.1.: *Overview of the performance of some of the most popular methods to produce graphene. Adapted from ref. 39.*

| | Quality | Size | Amount | Control | Ease |
|---|---|---|---|---|---|
| Mechanical exfoliation | ✓ | ✗ | ✗ | ✗ | ✓ |
| CVD | ✗ | ✓ | ✓ | ✓ | ✗ |
| Epitaxial growth | ✗ | ✓ | ✗ | ✓ | ✓ |
| Reduction of GO | ✗/✓ | ✗ | ✓ | ✗ | ✓ |

Because GO will play such a prominent roll in the following sections, it will be informative to discuss its structure in a bit more detail. The oxygen-containing groups in GO come in several forms[40–43]: the basal plane is decorated with both hydroxyl (C−OH) and epoxy (C−O−C) groups, with the proportion of the two dependent on method of production[44]. The edges of the flakes mainly contain carboxyl groups (C(O)OH). An illustration of a typical GO structure is shown in Fig. 2.1 B. After reduction, a fraction of the oxygen groups are removed[45], and the honeycomb lattice is partially recovered. However, the aromatic rings that previously contained oxygen are left damaged, typically forming pentagons and heptagons

with neighbouring rings[46]. Because the product of the reduction is not quite graphene, it has been termed Reduced Graphene Oxide (rGO). rGO does not fully regain all of the favorable properties of graphene, but considerable effort[47–49] has been made to repair the defects and recover true graphene. rGO is shown in Fig. 2.1 C.

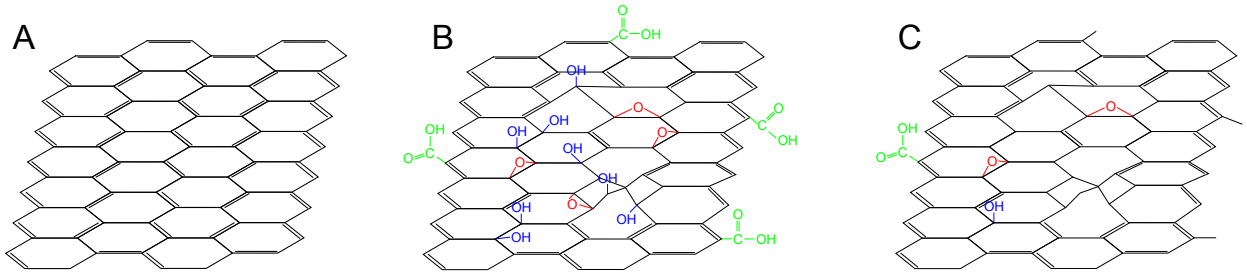


Figure 2.1.: *Illustration of the accepted structure of pristine graphene (A), graphene oxide (B), and reduced graphene oxide (C). Oxygen-containing moieties are present as defects from the well-known honeycomb lattice, with the main groups being hydroxyl (blue), epoxy (red), and carboxyl (green).*

Several schemes to reduce GO have been reported over the years, again with varying degrees of usefulness and scalability. The most popular are:

**Thermal** By heating GO sheets to high temperatures (>1000 °C), the oxygen-containing groups decompose into gases (typically CO and $CO_2$) and eventually escape from their bonding to the carbon plane[50]. The efficiency of this process is strongly dependent on the reducing environment, and it was found that exposure to various gases during reduction leads to favorable results[51,52]. However, thermal reduction results in a significant loss of carbon material (approximately 30 % of the starting GO mass[50]), and is not a possibility when the GO is part of an assembly or on a substrate that would be damaged by such high temperatures. Additionally, thermal reduction is typically a slow and energy-consuming process.

**Chemical** The reaction of GO with various chemical reagents can lead to reduction. The most popular reagents are hydrazine[53,54] ($N_2H_4$) and sodium borohydride[55] ($NaBH_4$). However, both of these chemicals are extremely environmentally unfriendly, and so this is not a particularly "green" approach.

**Photo-induced** The exposure of GO to various light sources in ambient conditions has been found to lead to the production of rGO (see the references contained in Table 2.2). This has been observed in both solid films and dispersions of GO with a high degree of control.

Of these, photo-induced reduction has shown promise to be a rapid and facile way of reducing GO while avoiding the use of harsh chemicals. Additionally, recent work using lasers as the light source has illustrated the potential of harnessing the high level of control over almost all optical characteristics (spatial profile, temporal profile, spectrum, etc.) offered by lasers. The

literature is full of various "recipes" in terms of the reduction conditions; this is elucidated in Table 2.2, which lists the experimental conditions of several of the pioneering works in light-induced reduction of GO. The deduced timescale of the reduction reaction ranges from sub-microsecond up to several hours.

Evidently, there is a lack of understanding of the exact chemical mechanism of the reduction. Several potential explanations exist: first, since relatively high powers are used, it is likely that a lot of the experiments listed in Table 2.2 involved photo-thermal reduction. From a more chemical standpoint, it is possible that the reduction consists of a direct mechanism (that is, the oxygen groups could directly absorb the illumination putting them in an excited, dissociative state). Alternatively, an indirect mechanism is possible, where the illumination modifies the environment (the dispersing solution, the substrate, etc.) which leads to reduction. Distinguishing between the possible reduction mechanisms and understanding their dynamics is challenging, but is important from both a fundamental and applied point of view.

TABLE 2.2.: *Literature survey of the experimental parameters used in some of the previous research using lasers to reduce graphene oxide*

| Reference | Wavelength | Repetition Rate | Pulse Duration | Exposure Time | Fluence/Power | Phase |
|---|---|---|---|---|---|---|
| [56] | 532 nm | Continuous Wave (CW) | – | 1 s | 20 mW | solid |
| [56] | 355/532 nm | 20 Hz | 9 ns | 20 s | 0 – 5 $MW/cm^2$ | solid |
| [57] | 790 nm | 80 MHz | 120 fs | 600 µs | 20 mW | solid |
| [58] | 663 nm | CW | – | ? | 1.6 $MW/cm^2$ | solid |
| [59] | 248 nm | 5 Hz | 30 ns | 6 µs | 300 mJ | solid |
| [60] | 532 nm | CW | – | 20 ms | 0.15 – 2.5 $MW/cm^2$ | solid |
| [61] | 9.4 µm | CW | – | ? | 4.8 $MW/cm^2$ | solid |
| [62] | 46.9 nm | ? | 1.5 ns | ? | 200 $mJ/cm^2$ | solid |
| [63] | 248 nm | 1 Hz | 20 ns | 0.2 – 24 µs | 20 – 80 $mJ/cm^2$ | solid |
| [64] | 248 nm | 5 Hz | 20 ns | 640 ns | 138 $mJ/cm^2$ | solid |
| [65] | 355/532 nm | 30 Hz | ? | 5 – 10 min | 5 – 7 W | dispersion |
| [66] | 280 – 450 nm | CW | – | 2 – 5 h | 67 $mW/cm^2$ | dispersion |
| [67] | 248 nm | 5 Hz | ? | 0.5 h | 300 mJ | dispersion |
| [68] | 248 nm | 5 Hz | 20 ns | 5 min | 833 $mW/cm^2$ | dispersion |
| [69] | 280 – 450 nm | CW | – | 5 min – 24 h | 636 $W/cm^2$ | dispersion |
| [70] | 800 nm | 1 kHz | 100 fs | ? | 58 $mJ/cm^2$ | dispersion |
| [61] | 400 nm | 1 kHz | 100 fs | 1 min | 4.1 $mJ/cm^2$ | dispersion |
| [71] | 300 – 1000 nm | CW | – | 2 h | 450 W | dispersion |

This chapter is devoted to examining the underlying chemical mechanism of the Ultraviolet (UV) reduction of GO in water. To access the fundamental timescale of the reaction, a pump-probe experiment using ultrafast laser pulses was conceived in which a flowing aqueous dispersion of GO is irradiated by a UV femtosecond pulse (the pump), followed by a second femtosecond visible pulse (the probe). The reduction of GO is accompanied by a significant spectral change, as highlighted by the "before" and "after" photographs in Fig. 2.2 (also see Fig. 2.3). As such, by measuring the change in absorption of the probe pulse, the evolution of the spectral changes during reduction can be followed in real time. In the following sections, the results of the experiment will be used to motivate the introduction of a chemical pathway that accounts for the observed UV photoreduction in both solids and dispersions.

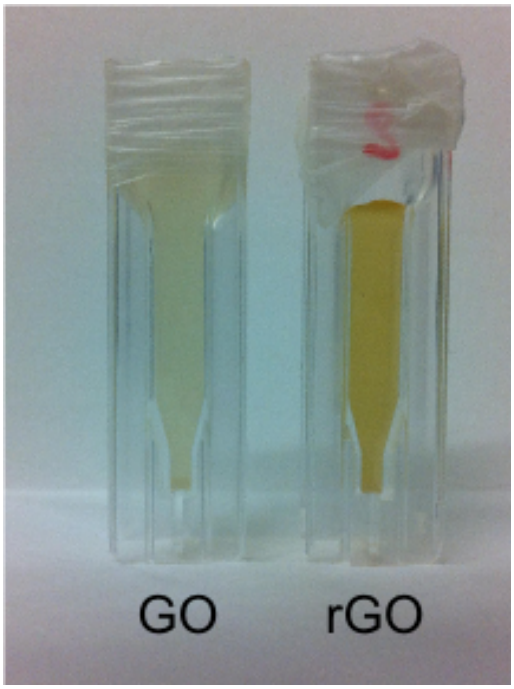


Figure 2.2.: *Photograph of dispersions of graphene oxide (GO) and reduced graphene oxide (rGO) in water. The rGO was formed by exposing a dispersion identical to the one on the left to an ultraviolet laser overnight.*

## 2.2. Preparation and Characterization of Graphene Oxide and Reduced Graphene Oxide*

GO flakes were prepared by the Staudenmaier method[38], which, as mentioned in the Introduction, consists of using a strong acid to simultaneously exfoliate and oxidize graphite

* The production of the GO flakes and both the Raman and XPS measurements discussed in this chapter were performed by the group of Prof. Dimitrios Gournis at the University of Ioannina (see ref. 26). These results will be described here for completeness.

flakes. Aqueous dispersions were prepared by mixing the flakes in ultrapure, demineralized, deionized water (18.2 MΩ cm) and sonicating overnight in a sonicator bath (Bandelin Sonorex RK 510, 400 W). Very high loading of GO was required in order to achieve a sufficiently high optical density to give a measurable signal. This high loading ($\sim$ 10 mg/mL) led to precipitation of non-exfoliated GO flakes in the prepared dispersion, therefore the supernatant was separated using centrifugation (10 min at 3000 rpm in a Hermle Z 206 A). The final concentration ($\sim$ 2 mg/mL) of the supernatant was measured by drying a small volume in air and weighing the residual solid material.

The GO and the product of the photoreduction (rGO) were characterized by a variety of methods to firmly establish the initial and final states of the reduction reaction. To obtain the rGO, a volume of aqueous GO dispersion was irradiated overnight with the ultraviolet pump laser that was used in the time-resolved measurements (see Section 2.3). The solution was continuously stirred with a magnetic stirring rod to ensure homogeneous illumination of the entire volume. Such a long exposure time was chosen to allow for the vast majority of the GO to become reduced.

From the corroboration of the independent characterization methods presented below it can be concluded that the sample produced after ultraviolet irradiation is truly rGO.

### 2.2.1. Ultraviolet-Visible Absorption Spectroscopy

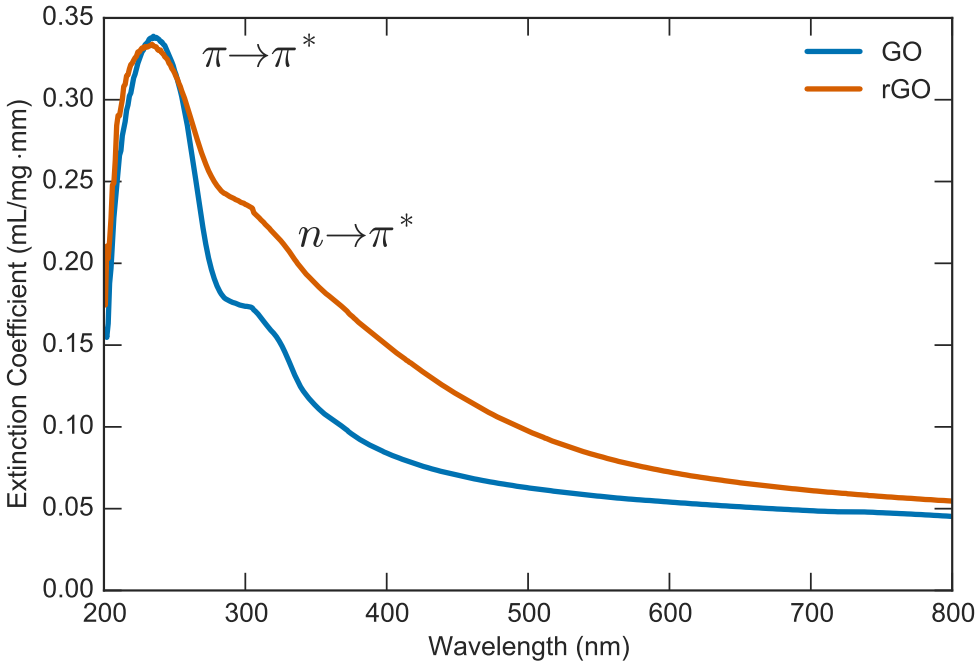


Figure 2.3.: *Ultraviolet-visible absorption spectra of aqueous dispersions of graphene oxide (GO) and reduced graphene oxide (rGO)*

Due to the presence of the oxygen-containing moieties, GO is expected to have a significantly different electronic structure from both bulk graphite and single-layer graphene. To examine the electronic structure of the GO prior to reduction, ultraviolet-visible (UV-vis) spectroscopy was used to probe the electronic transitions. Fig. 2.3 shows the resulting spectrum (measured on a Shimadzu UV-2600 spectrophotometer), displaying the large $\pi \rightarrow \pi^*$ transition around 231 nm that is characteristic of the aromatic carbon structure[72]. Also present is a significant shoulder around 300 nm due to the $n \rightarrow \pi^*$ transition in the oxygen-containing groups[72,73]. The UV-vis spectrum of the rGO shows an overall increase in absorption in the 280 – 800 nm range, which is indicative of the presence of more aromatic domains[66]. The decrease in the $n \rightarrow \pi^*$ shoulder corresponds to the removal of some of the oxygen-containing groups.

## 2.2.2. Raman Spectroscopy

Raman spectroscopy was performed to further characterize the quality of the GO and rGO. Spectra were recorded with a micro-Raman system RM 1000 RENISHAW using a laser excitation line at 532 nm (Nd-YAG) with a power of 1 mW. A 1 mm focusing spot was used in order to avoid photodecomposition of the sample. Minute quantities of GO or rGO dispersions were drop-casted onto a glass substrate and left to dry in air before transfer to the measurement apparatus.

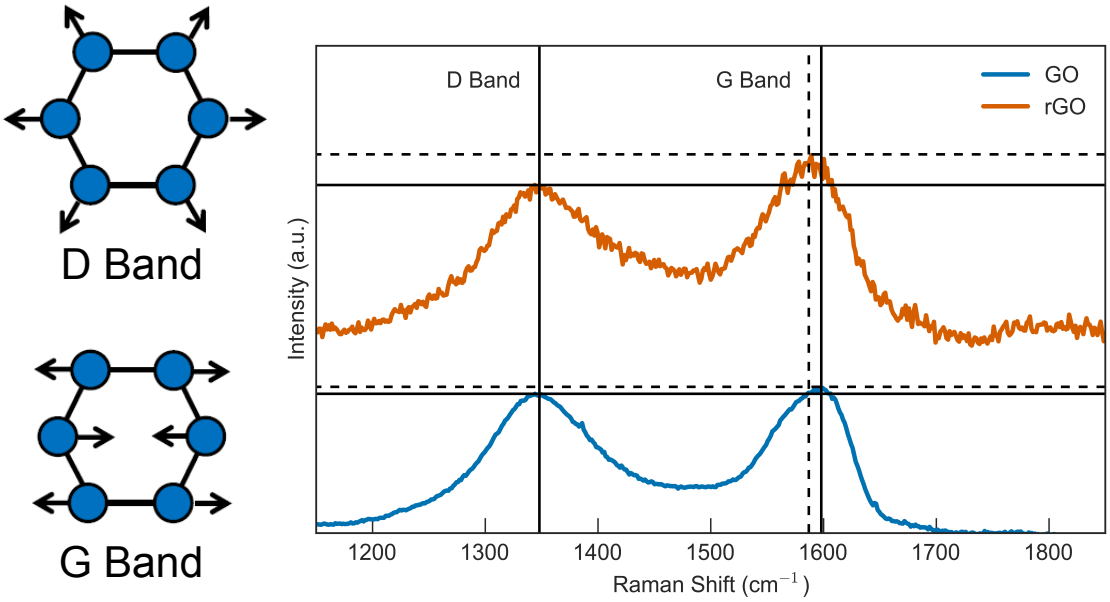


Figure 2.4.: *Raman spectra of graphene oxide before (GO) and after (rGO) photoreduction*

Raman spectroscopy measures the energy in vibrational modes, and so is highly sensitive to the local environment within the GO. For instance, the D band, involving the "breathing" of the aromatic rings, is Raman inactive, but is visible in GO due to the presence of defects in the form of the oxygen-containing groups. The G band however, involving in-plane optical vibrations, is present in both GO and graphene. The ratio of the intensity of the D and

the G bands is inversely proportional to the size of the "graphene-like" domains ($sp^2$-bonded clusters) in the GO[74]. Fig. 2.4 displays the Raman spectra from before (GO, blue) and after (rGO, orange) ultraviolet irradiation. For the starting material (GO), the characteristic D and G bands are at 1348 and 1598 $cm^{-1}$, respectively, and the D/G band intensity ratio is 0.94. The rGO spectrum shows a slightly shifted G band and a reduced D/G intensity ratio of 0.83. This observation, explained by a graphitization of the sample as described by Yang *et al.*[75], is in good agreement with the extended literature[76–79]. However, the D/G intensity ratio is highly dependent on the quality of the starting GO and the reduction method employed[77], and so X-ray Photoelectron Spectroscopy (XPS) was used to quantify the degree of reduction as it constitutes a more direct probe.

### 2.2.3. X-Ray Photoelectron Spectroscopy

XPS identifies the elemental composition of a sample by measuring the energies of all chemical bonds present. Measurements were performed under ultrahigh vacuum conditions with a base pressure of $5 \times 10^{-10}$ mbar in a SPECS GmbH instrument equipped with a monochromatic Mg $K_\alpha$ source (1253.6 eV) and a Phoibos-100 hemispherical analyzer. The preparation of the sample was identical to that used in the Raman measurements except with a doped silicon substrate. Binding energies were corrected using the $C \rightarrow C^*$ transition at 284.75 eV as a reference.

As is evident from the spectra in Fig. 2.5, the vast majority of carbon atoms in GO are bonded to oxygen in a variety of functional groups (mainly hydroxyl and epoxy), consistent with the present picture of the structure of GO (see Fig. 2.1 B). This confirms that the GO is significantly oxidized. The removal of the oxygen content after the photoreduction is obvious and observable as a dramatic decrease of the C−O (286.25 eV), C=O (287.25 eV) and C(O)OH (288.75 eV) peaks. By quantifying the relative intensities of the constituent peaks, it was found that a restoration of the pure C−C bond from 8 % to 66 % was obtained by photoreduction.

## 2.3. Optical Pump-Probe Setup

Satisfied that exposure to UV laser light leads to the production of rGO, the dynamics of the reduction mechanism were studied in optical pump-probe experiments that were performed in transmission mode in the configuration shown in Fig. 2.6. The primary laser source was a 1 kHz regenerative femtosecond laser system that provided 40 fs pulses at 800 nm (Legend Elite Duo, Coherent Inc.). The 400 nm probe and 266.$\overline{6}$ nm pump were produced from the second and third harmonics (respectively) of the fundamental beam using $\beta$-Barium Borate (BBO) nonlinear crystals. The process of producing these harmonics will be examined in depth in Section 3.3.2, and so will not be discussed further here, except to state that the

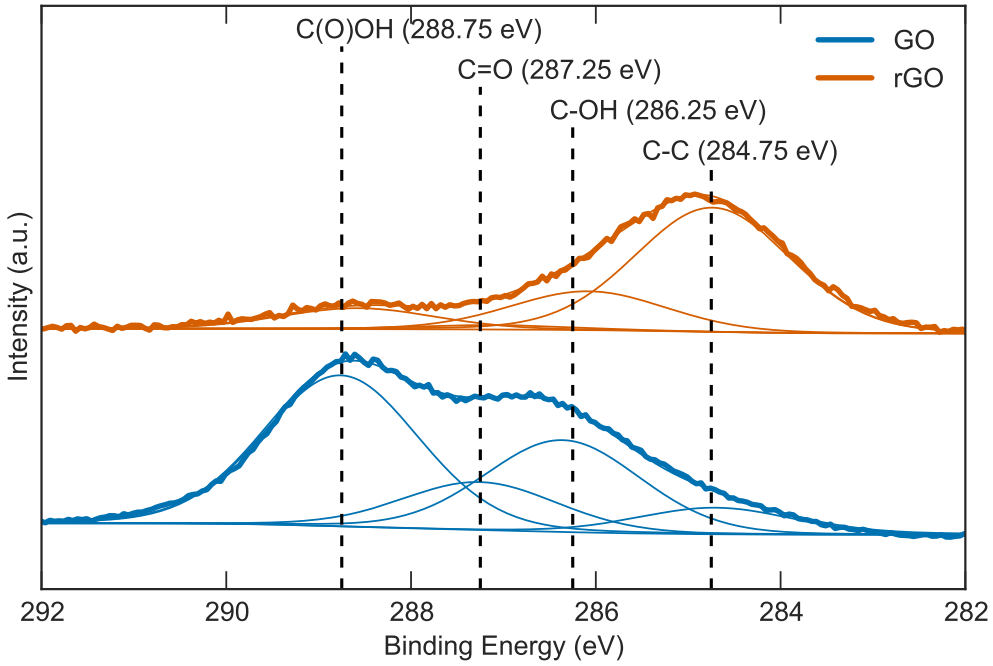


Figure 2.5.: *X-ray photoelectron spectroscopy of graphene oxide (GO) and reduced graphene oxide (rGO)*

expected pulse durations (full-width at half-maximum) are about 70 fs at 400 nm and 90 fs at 266.$\overline{6}$ (see Section 3.3.2 for simulations of harmonic generation). Some experiments used a broad-band, white light probe, which was produced by focusing the fundamental into a 2 mm thick piece of sapphire.

The pump and probe were focused into the sample at incident angles of 31° (pump) and 50° (probe) with respect to the surface normal of the sample cell with spot diameters of 220 µm (pump) and 80 µm (probe). The transmission through the sample was detected using a photodiode and a lock-in amplifier after modulating the pump with a 500 Hz optical chopper. When the white light probe was used, the detector was replaced with a fiber-coupled spectrometer (AvaSpec-2048, Avantes). The pump power was 800 mW at 500 Hz (1.6 mJ per pulse), and the probe power was kept as small as possible while still providing relatively good signal-to-noise (typically $\sim$ 15 µW). As the reduction is irreversible, all experiments were performed with the sample flowing through an ultraviolet fused-silica optical cell with a 1 mm pathlength. The flow rate was on the order of 3 mL/min.

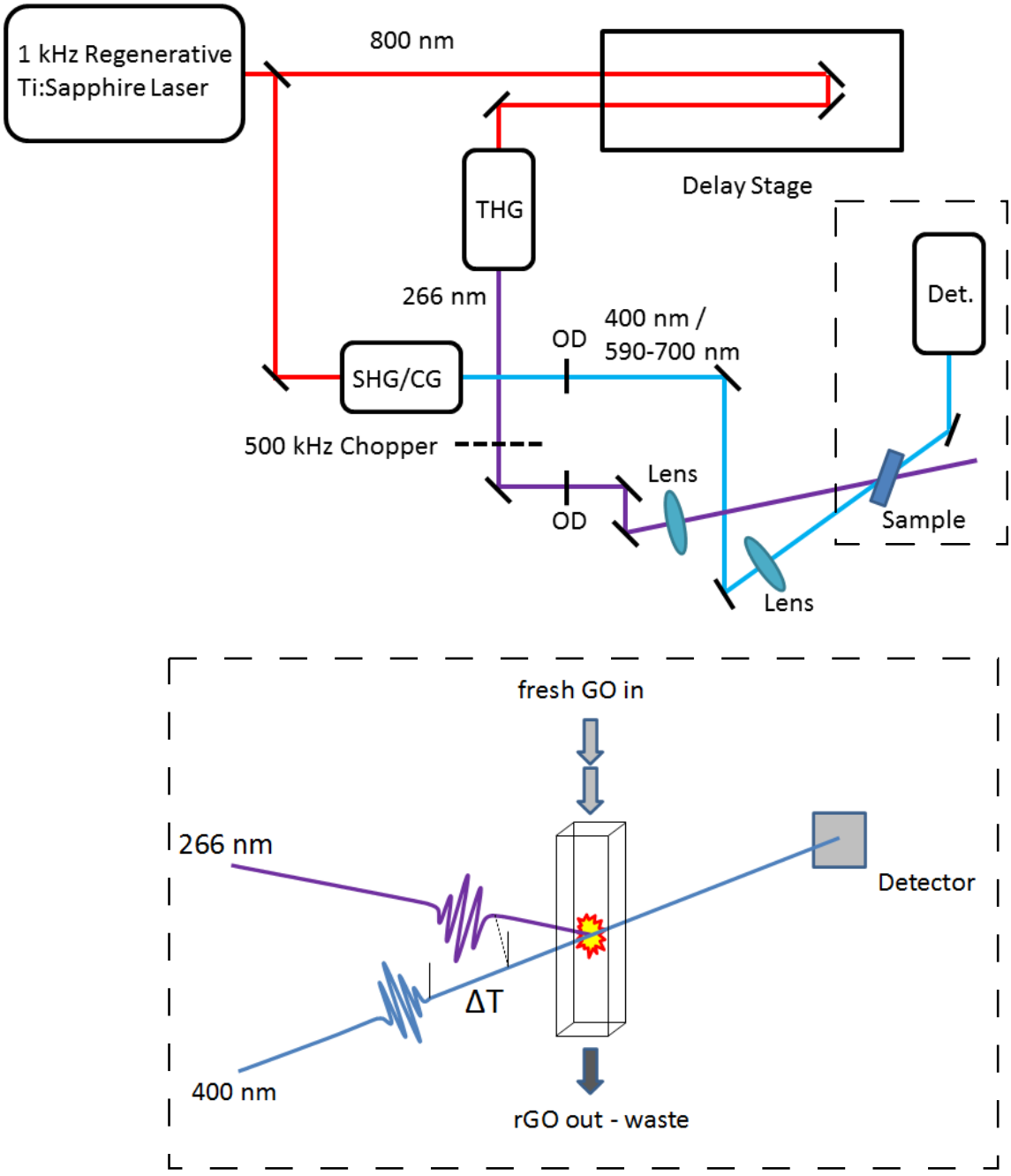


Figure 2.6.: *(Top) Illustration of the optical system used to perform pump-probe experiments. SHG: second harmonic generation, CG: continuum generation, THG: third harmonic generation, OD: optical density filter, Det: detector (either a photodiode or a spectrometer). (Bottom) Drawing of the transient absorption setup highlighting the flow cell.*

The pump and probe path-lengths from the laser output aperture to the sample position were carefully measured with a ruler and the arrangement of the optics was chosen so that these lengths were roughly equal. To identify the delay stage position corresponding to the temporal overlap, a pump-probe experiment was performed on a sample with an immense response to the UV pump. The large change in the transmission signal facilitated the identification of the temporal overlap. For this purpose, the organic solvent N-Methyl-2-Pyrrolidone (NMP) was used. Being polar, UV-irradiation of NMP results in the production of solvated electrons and the corresponding characteristic increase in absorption.

Rough spatial alignment was achieved by observing the fluorescence produced by the pump and probe beams hitting a piece of paper at the sample position (in the cuvette full of water). The pump was moved until overlap was achieved as observed in an optical microscope. The presence of the liquid within the cell was found to be important to account for the refraction through the liquid in the true experiment. The alignment was then fine-tuned by maximizing the NMP response.

## 2.4. Transient Absorption of the Reduction of GO

This section will present the core experimental results of this chapter, starting with the transient change in the absorption spectrum shown in the top panel Fig. 2.7. At positive delay times there is a strong but spectrally non-uniform change in absorption. Two regions of increased absorption can be seen, one at lower wavelengths ($< 660\,\text{nm}$) and the other at higher wavelengths ($> 740\,\text{nm}$). These features can be explained as the consequence of a combination of two processes illustrated in the lower panel of Fig. 2.7: the first is an overall absorption increase that is more heavily weighted toward lower wavelengths associated with the GO to rGO transition (see the spectra in Fig. 2.3). The second is the well-known wavelength-dependent increase of absorption in UV-irradiated water that peaks at 750 nm (ref. 80). This signal originated from the ultrafast formation of solvated electrons as the product of UV photolysis of the water molecules. Because the observed transient absorption signal during the reduction reaction contains a significant contribution from the solvent, these results hinted that reduction may be caused by an indirect mechanism involving the local environment.

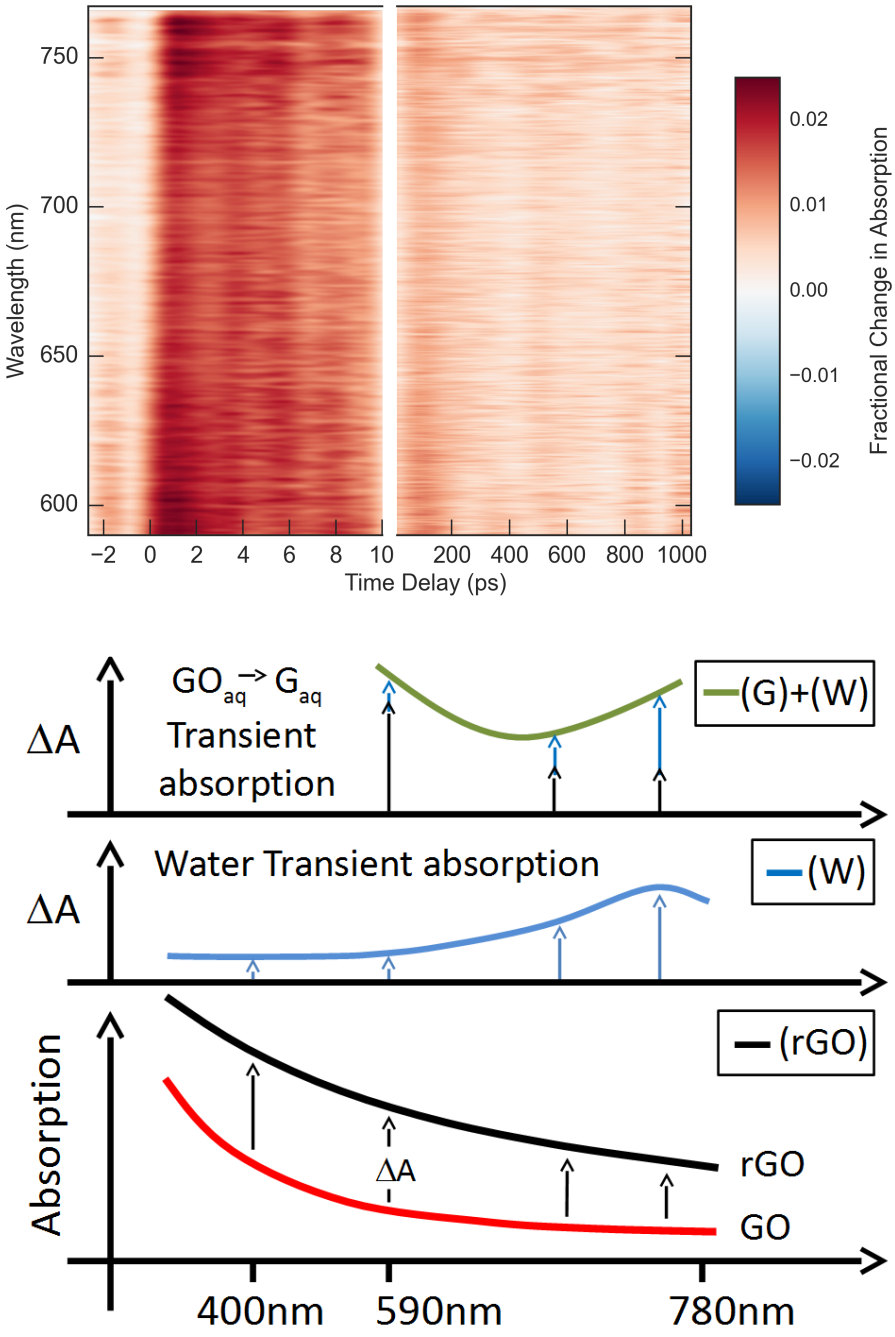


FIGURE 2.7.: *Transient differential absorption spectroscopy of a* $2\,\mathrm{mm\,mg^{-1}}$ *graphene oxide dispersion in water with a* 266 nm *pump and white light probe (590 –* 760 nm*) (top). Sketch of the processes resulting in the transient differential absorption spectra. The contribution of reduction overlaps with the rising transient absorption signal of (W) water with contributions from (G) reduced graphene oxide (bottom).*

To pursue this possibility, further pump-probe experiments were performed with a 400 nm probe, enabling increased signal-to-noise relative to the white-light probe discussed above. Such measurements are displayed in Fig. 2.8, showing the concentration-dependent transient absorption measurements of GO in water. For all concentrations, a steep rising peak followed by a rapid decay ($< 2$ ps, Fig. 2.8 A) and a slower decay ($< 250$ ps, Fig. 2.8 B) can be observed. This behaviour is again due to multiple contributions from the water and GO. The initial rise corresponds to the excitation of water via two photon absorption and the photo-excitation and ionization of GO. The excited state of water leads to the generation of $OH_{aq}$, $H_3O^+_{aq}$, and solvated electrons ($e^-_{aq}$) within 1 ps (ref. 80). It is proposed that the solvated electrons act as the reducing agent. Any ionization of GO will likewise generate solvated electrons but this electron source term constitutes an oxidation step. Only the solvated electrons generated in the water region lead to a net surplus of electrons with respect to the GO valence occupancy that in turn can drive the overall reduction process. The slow decay (for $t < 250$ ps) of the absorption transient results from a decrease in the population of the mobile solvated electrons due to either interaction with GO or recombination with parent ions. The overall proposed reaction is

$$\begin{aligned} GO + H_2O + 2h\nu &\longrightarrow GO^* + H_2O \\ &\xrightarrow{0.5-1\,\text{ps}} GO + OH_{aq} + H_3O^+ + e^-_{aq} \xrightarrow{1-250\,\text{ps}} rGO + H_2O \end{aligned} \qquad \{2.1\}$$

The data contained in Fig. 2.8 A and B are consistent with this model. The long-lived component of pure water corresponds to a residual absorption increase of $\sim 1.5 \times 10^{-3}$ after 1 ns and is assigned to a fully thermalized species of solvated electrons[81–84]. The increased residual absorption change of GO-containing samples, when compared with pure water, results from the additional absorption of newly formed rGO. A quantification of these results was obtained by comparing the residual of the transient absorption with fully rGO absorption extracted from Fig. 2.3. This analysis shows a reduction of $\sim 2\,\%$ after 250 ps. Multiple UV laser pulses will therefore be necessary to fully reduce the sample. From Fig. 2.8 C, one sees that the final absorption (proportional to the quantity of rGO produced) increases linearly with the GO concentration indication that the reduction efficiency is concentration independent.

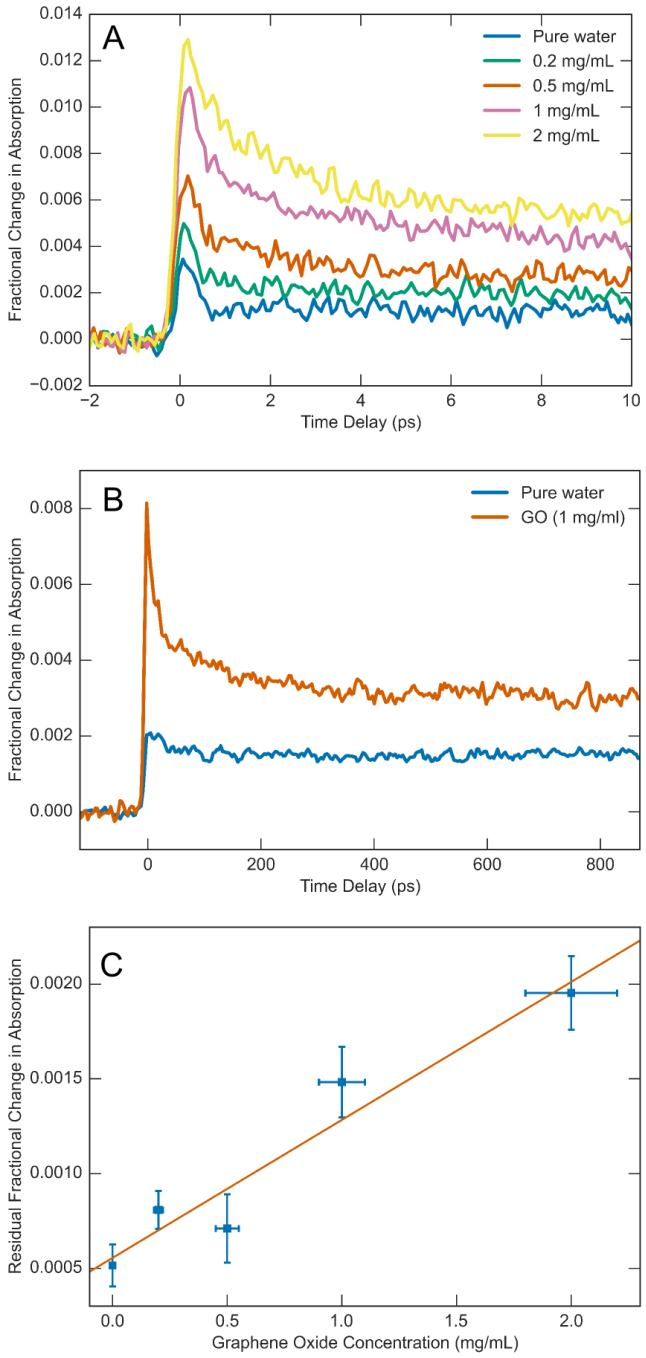


FIGURE 2.8.: *Transient differential absorption of ultraviolet-irradiated aqueous graphene oxide (GO) dispersions at* 400 nm. *(A) Titration of the GO concentration dependence of the dynamics, in water, ranging from* $0\,\mathrm{mg\,mL^{-1}}$ *to* $2\,\mathrm{mg\,mL^{-1}}$ *on a* 10 ps *time scale. (B) Long time scale dynamics of a* $1\,\mathrm{mg\,mL^{-1}}$ *GO dispersion versus pure water. (C) Plot of the residual absorption value in* $\Delta OD$ *versus graphene oxide concentration. The vertical error bars are the standard deviation of the calculated values displayed. Each point represents the average intensity of the last* 2 ps *(from* 8 – 10 ps*), thus the error bars represent the noise level. The horizontal error bars represent an estimated* 5 % *experimental error on the measure of the absolute GO concentration.*

## 2.5. Possible Reduction Pathways

To accurately interpret and understand the presented results, it is important to explore the possible reaction pathways leading to the reduction of GO. As stated previously, the possibilities are thermal reduction, direct reduction involving the optical excitation of GO, or an indirect mechanism involving contributions from the local environment. The proposed reaction, Reaction 2.1, falls into the indirect category, but the other possibilities must be considered as well.

### 2.5.1. Laser-Induced Temperature Increase

Because the reaction under consideration is initiated by an intense laser source, the possibility of thermal reduction needs to be considered. To estimate the temperature rise of the GO flakes caused by the ultraviolet laser exposure, the illumination volume is modeled as a cylinder of radius $R$ and length $L$, where $R$ is the pump laser's focal radius and $L$ is the path length through the cuvette. The temperature increase $\Delta T$ per laser shot can be conservatively estimated by dividing the energy deposited into the excitation volume by the heat capacity of GO:

$$\Delta T = \frac{pQ}{c_{GO}\pi R^2 L C_{GO}} \tag{2.1}$$

where $p$ is the fraction of ultraviolet light absorbed by GO, $Q$ is the laser pulse energy and $C_{GO}$ and $c_{GO}$ are the concentration and heat capacity of GO, respectively. The heat capacity is assumed to be similar to that of graphite, and so a value of $c_{GO} = 2\,\mathrm{J/gK}$ can be used[85,86]. The fraction of absorbed light was found to be $p \approx 0.43$ from the static absorption spectrum, giving a temperature increase of $\Delta T \approx 4.5\,\mathrm{K}$ per laser shot. Additionally, possible heat transfer to the bath was not accounted for in this simple model, and this would serve to decrease the GO temperature. As the sample is continuously refreshed through flow, accumulative heating is excluded. Such a temperature is far below previously reported thermal treatments leading to any observable reduction[77], which typically consist of temperatures in the 1000 °C range.

### 2.5.2. Direct versus Indirect Reduction

Having ruled out thermal reduction, the remaining possibilities are a direct or indirect mechanism. If occurring, the direct photoreduction of GO would consist of the photoionization of the GO as ultraviolet pump (4.65 eV) is far from any resonant excitation of any C−O or C=O bonds, but near the work function of GO (4.9 eV, ref. 87). However, photoionization would

lead to the creation of an electron-hole pair and consequently further oxidize the sample, not reduce it.

Based on this argument, it is unlikely that direct processes contribute significantly to the reduction. Although our results are consistent with the interpretation of solvated electron-mediated reduction, to conclusively support the proposed mechanism an additional control experiment was performed. A so-called electron scavenger (a species that is well known in the field of radiochemistry) was used to 'capture' the solvated electrons thereby removing the source of excess electrons. For this purpose, 0.75 % (v/v) acetone was mixed in a $2\,\mathrm{mg\,mL^{-1}}$ aqueous GO dispersion. Time-resolved differential absorption data (Fig. 2.9) shows the evolution of the reaction. One can see a significant decrease in the intensity over the whole trace in comparison to a pure GO dispersion. This behaviour demonstrates the fact that solvated electrons, produced in water after ultraviolet excitation, are rapidly quenched in the presence of acetone[84]. As acetone and GO are both present in the solution, a competition takes place for the capture of solvated electrons. The existence of these two reaction pathways diminishes the overall yield of the rGO production (Fig. 2.9). These results testify that the excess electrons provided by the water ionization are imperative for the ultraviolet photoreduction of GO.

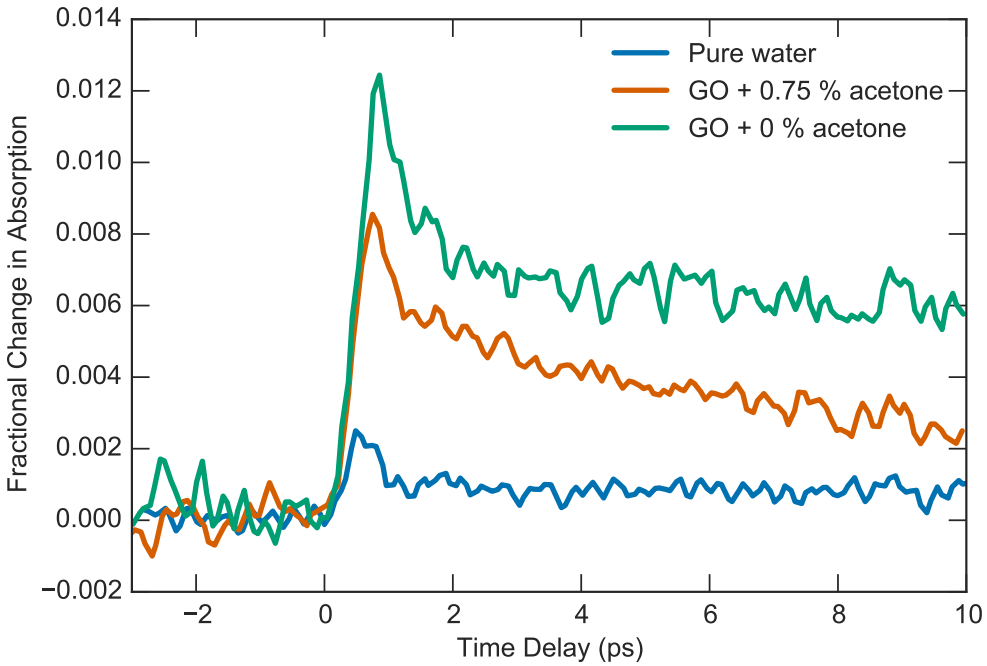


Figure 2.9.: *Transient differential absorption of a* $2\,\mathrm{mg\,mg^{-1}}$ *graphene oxide (green) without acetone, (orange) with* 0.75 % *acetone and (blue) pure water.*

## 2.6. Conclusions and Outlook

This chapter demonstrated that the photoinduced transformation of GO to rGO is an indirect process, mediated by the involvement of solvated electrons produced by the ultraviolet photoionization of the solvent. The sequence of events in Reaction 2.1 testifies to the non-thermal nature of the reduction in that it is the chemical potential of the solvated electrons that drives the reduction and not simple heating effects on barrier crossing.

It is possible that these results also provide an explanation for some of the solid-state experiments listed in Table 2.2, as certain substrates can provide a surplus of electrons which have shown the potential for driving reactions on adjacent materials[88]. Thus these results call for new investigations of the reduction dynamics of GO in the solid state. However, such experiments are beyond the scope of this thesis; instead, the following chapters will explore how to measure the time-dependent structural changes in reactions such as the reduction of GO.

# 3. Ultrafast, Low-Energy Electron Diffraction of Thin Films

*"It's still magic even if you know how it's done."*

— Terry Pratchett

## 3.1. Introduction

While the previous chapter demonstrated the power of transient spectroscopy for studying the dynamics of thin films, such optical techniques lack direction information about what is happening on a structural level. For instance, in the reduction of GO studied in Chapter 2, it would be insightful to know how the structure of the GO evolves during the reduction; for instance, how does the removal of the oxygen-containing moieties influence the positions of the neighbouring carbon atoms? Such information would be challenging to infer from optical experiments.

To this end, this chapter will introduce the technique of ultrafast electron diffraction (UED), and extend its capacity to the low-energy regime to enable the study of the thin films and monolayers that are the focal point of this thesis. This is achieved by the design and construction of a novel UED system operating at low energies (1 – 10 kV). The successful realization of this machine required the introduction of several new design principles that expand on the traditional UED setup. Detailed simulations of electron beam propagation in the machine were conducted to provide a baseline to compare with the measured performance.

Prior to introducing the experimental details of the UED setup, it should be noted that electron crystallography is a rich and established field, and so the customary introduction to its detailed theory will be omitted for brevity. Instead, the reader is referred to references[89–93] for a thorough exposition. However, to motivate some of the design principles in the following sections, certain fundamental concepts will be introduced for completeness, with the understanding that this serves only as a superficial introduction.

## 3.2. Elements of Ultrafast Electron Crystallography

The most important parameter in any diffraction experiment is the wavelength of the probe. In fact, the very short wavelength of fast electrons was the reason for their use in crystal-

lographic experiments in the first place. But what is a suitable wavelength for an electron crystallography experiment? To address this question, consider an electron with wavelength $\lambda$ scattering from the $(h, k, l)$ planes of a crystal. The scattering angle $\theta_{hkl}$ satisfies Bragg's law[94]:

$$\sin\theta_{hkl} = \frac{\lambda}{2d_{hkl}} \tag{3.1}$$

where $d_{hkl}$ is the interplanar spacing. Since the values of $\sin\theta_{hkl}$ are bounded by $[-1, 1]$, this imposes a stringent requirement on possible values of the electron's wavelength, namely

$$\lambda < 2d_{hkl} \tag{3.2}$$

Erring on the smaller side and taking 1 Å a typical length scale for the periodicity in a crystal, this means that electrons must have sub-angstrom wavelengths in order to be used for crystallography. Fortunately, this is readily achieved by accelerating electrons to extremely high speeds; the de Broglie wavelength of an electron accelerated by a potential $U$ is, accounting for relativistic effects[95],

$$\lambda = \frac{2\pi}{k} = \frac{h}{\sqrt{2m_e qU + \frac{q^2U^2}{c^2}}} \tag{3.3}$$

where $k$ is the electron's wavenumber, $h$ is Planck's constant, $q = 1.602 \times 10^{-19}\,\mathrm{C}$ is the elementary charge, $m_e = 9.109\times10^{-31}\,\mathrm{kg}$ is the electron's rest mass, and $c = 299,792,458\,\mathrm{m/s}$ is the speed of light in vacuum. This function is plotted in Fig. 3.1, which demonstrates that electrons accelerated by potentials of a few tens of kilovolts have wavelengths comparable to the atomic spacing in matter, and so are suitable for use crystallographic experiments.

In addition to the wavelength of the probe, there are several other characteristics that are imperative for a successful ultrafast diffraction experiment. The first of these is the *transverse coherence length*, $\xi_\perp$. An intuitive picture of the coherence length can be thought of as follows: in an ideal experiment, the incident electron's wave is a plane wave, so that all of the unit cells in the illuminated region of the sample scatter in-phase; this maximizes the constructive interference, resulting in the best quality diffraction pattern. However, even the best quality electron beams have some dispersion, and so deviate from an ideal plane wave. In this case, only scatterers that are near each other produce interference. The transverse coherence length provides a measure of how well an electron beam can produce interference from scatterers that are far apart, and can be defined as[96]

$$\xi_\perp = \frac{\lambda}{2\pi\sigma_\theta} = \frac{\hbar}{\sigma_{p_\perp}} \tag{3.4}$$

where $\sigma_\theta$ is the half-angle of the divergence of the beam, and $\sigma_{p_\perp}$ is the (local) uncorrelated

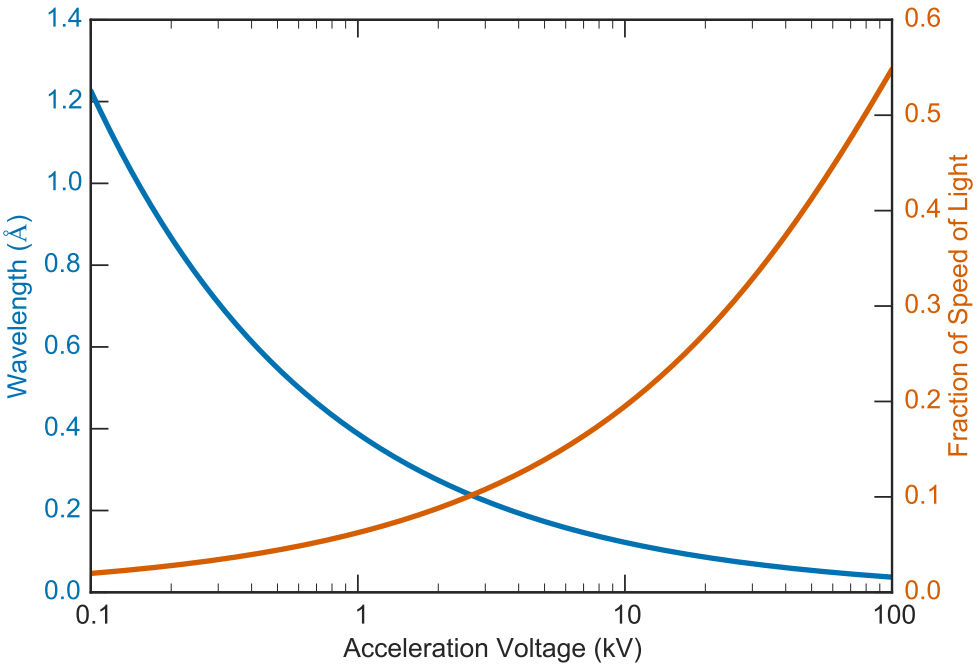


Figure 3.1.: *The dependence of the wavelength and speed on the acceleration voltage of electrons in an electron crystallography, accounting for relativistic effects*

momentum spread. To see what role this plays in UED experiments, consider an illustrative case in which electron diffracts from a simple cubic lattice with a lattice constant $a$. In the limit that the incident electron is a plane wave, the diffraction pattern (in reciprocal space) will be[92]

$$I(\mathbf{q}) \propto \prod_{i=1}^{3} \frac{\sin^2\left(N_i \frac{q_i a}{2}\right)}{\sin^2\left(\frac{q_i a}{2}\right)} \tag{3.5}$$

where $\mathbf{q}$ is the electron's wavevector and $N_i$ denotes the number of illuminated unit cells along the $i^{\text{th}}$ axis. This function is plotted in Fig. 3.2, which shows the dependence of the peak width on the number of unit cells. It is evident that the more unit cells that contribute to the interference process, the sharper the diffraction peaks. It is therefore favorable to have as many unit cells illuminated in phase as possible. Because the transverse coherence length characterizes the distance over which the incident electron wave is roughly planar, $\xi_\perp \propto N_i$ and so a larger transverse coherence length results in sharper diffraction peaks. While this discussion was limited to the simple case of a cubic crystal, the results hold more generally; in fact, regardless of the type of lattice, in an idealized experiment devoid of any instrumental broadening, the width of the Bragg peaks in reciprocal space are exactly equal to the inverse of the transverse coherence length[97–99].

Although there are many additional experimental parameters that play an important role in the quality of a UED experiment, the final one that will be discussed here is the pulse

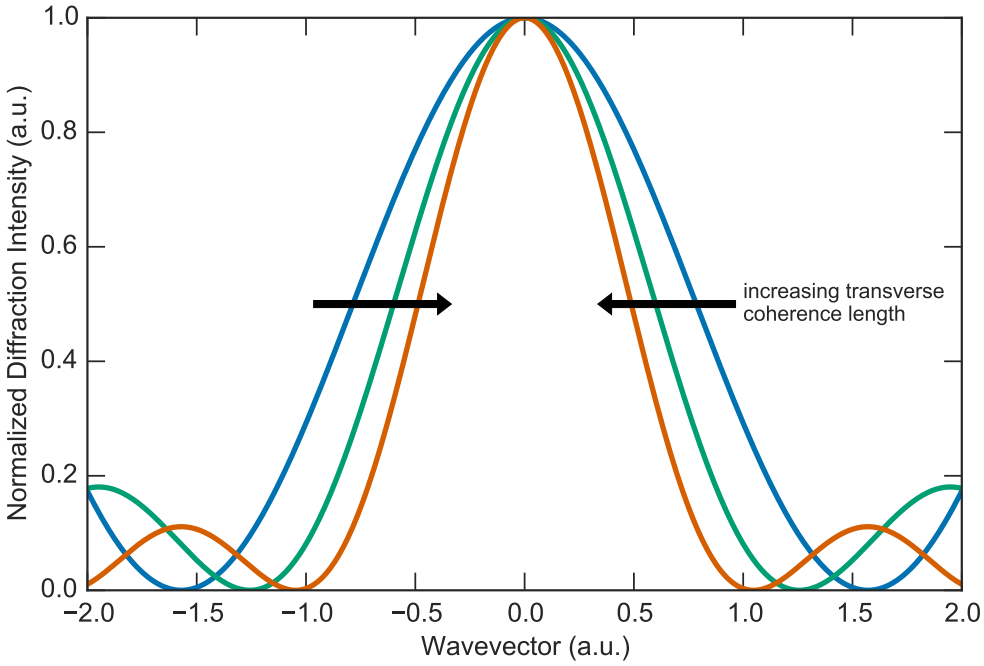


Figure 3.2.: *The dependence of the width of a Bragg peak on the transverse coherence length of the probe in an electron crystallography experiment*

duration of the electron bunch, which has the strongest influence in the temporal resolution of the experiment. To introduce the time-dependent diffraction pattern, it is first stated that the generalized form of Eq.(3.5), corresponding to an arbitrary crystal, is approximately $I(\mathbf{q}) \propto |F(\mathbf{q})|^2$, where, in the vicinity of the $(h,k,l)$ reflection, is[93]

$$F(\mathbf{q}) \approx F(hkl) = \sum_{i=1}^{n} f_i \exp\left[-2\pi i \left(hx_i + ky_i + lz_i\right)\right]. \tag{3.6}$$

$F(hkl)$ is known as the *structure factor* of the $(hkl)$ reflection, and depends on,

1. the total number $n$ of atoms in each unit cell,

2. the position $\mathbf{r}_i = x_i\mathbf{a} + y_i\mathbf{b} + z_i\mathbf{c}$ of the $i^{\text{th}}$ atom in the unit cell, where $(\mathbf{a},\mathbf{b},\mathbf{c})$ is the basis of the crystal, and

3. the chemical type of each atom in the unit cell through the *atomic scattering factor* $f_i$, which governs the scattering strength of the $i^{\text{th}}$ atom.

All UED experiments to date have either been unimolecular reactions (i.e. $\mathrm{A} \rightarrow \mathrm{B}$), or transient perturbations out of equilibrium (i.e. $\mathrm{A} \rightarrow \mathrm{A}^* \rightarrow \mathrm{B}$), and the experiments presented in the following chapters are no exception. Such dynamics manifest themselves as time-dependence of the structure factor, and so either $f_i \rightarrow f_i(t)$, corresponding to the excitation

of the $i^{\text{th}}$ atom, or $\mathbf{r}_i \to \mathbf{r}_i(t)$, corresponding to the displacement of the $i^{\text{th}}$ atom, or both. In any case, it is therefore imperative that the time resolution of the experiment be sufficient to sample the time-dependent diffraction pattern $I(\mathbf{q}, t) = |F(hkl, t)|^2$.

The core concepts of wavelength, coherence length, and pulse duration are fundamental to the field of UED, and their introduction here will inform and give context to the discussion of the design principles of the novel UED setup presented in the following section.

## 3.3. UED of Thin Films: Design Principles and Experimental Parameters

UED setups borrow from many technical fields such as optics, ultrahigh vacuum science, high voltage electronics, and materials science. A successful experiment is reliant on the concerted performance of all these constituent components. The specifics of each of these components and a justification for their design concepts will be outlined in this section, with particular emphasis places on their impact on the experimental parameters introduced in the preceding section.

### 3.3.1. Electron Gun

#### Acceleration Voltage

The choice of the appropriate electron energy is key to the design of a successful UED machine. By nature of Eq.(3.3) the acceleration voltage determines electron's wavelength, but it also influences many other aspects of the experiment. In general, higher energy offers improves temporal resolution and coherence properties, but at the cost of small scattering angles and low scattering cross-sections. On the other hand, low energy electrons travel slowly and so are more prone to space-charge effects, but at the same time scatter more efficiently from thinner samples. The general guiding principle for the design of a UED machine is to find the most appropriate balance between these factors. Ideally the energy is chosen so that the wavelength satisfies Eq.(3.2) and also encourages

1. high temporal resolution (short electron pulses)
2. high spatial coherence
3. high probability of elastic scattering
4. low probability of inelastic scattering

While the first two of these are also strongly influenced by the electron optics and the photoemission process (see Section 3.3.1), the latter two are determined solely by the sample's chemical composition and the acceleration voltage. Because of this, the following paragraphs will introduce a general rule-of-thumb for choosing the electron energy when applying UED to study thin films.

The theory of electron diffraction can broadly be characterized into two camps: *kinematic* diffraction, which only considers single scattering events, or *dynamic* diffraction, where multiple scattering is accounted for. Although the dynamic diffraction theory offers a more realistic description of the true physics, the kinematic theory culminates in a simple relationship between the scattered intensities and the scattering potential, which facilitates analysis of UED data. As such, UED experiments try to operate in the kinematic regime.

Since multiple scattering is composed of independent, sequential scattering events, the probability that an electron scatters $n_{\text{el/inel}}$ times (either elastically or inelastically) when passing through a sample of thickness $t$ is given by a Poisson distribution[100]:

$$P(n) = \frac{1}{n!}\left(\frac{t}{\Lambda(E)}\right)^n \exp\left(-\frac{t}{\Lambda(E)}\right) \tag{3.7}$$

where the subscripts "el/inel" have been dropped for brevity. In this expression, $\Lambda_{\text{el/inel}}(E)$ is the corresponding elastic/inelastic mean free path, which depends on the kinetic energy $E$ of the probe electrons, and represents the average value which the electron travels between scattering events. The average number of scattering events, $\bar{n}_{\text{el/inel}} = t/\Lambda_{\text{el/inel}}(E)$, is thus determined by the ratio of the sample's thickness to the mean free path. Therefore to ensure that the UED experiments remain in the kinematic regime (that is, $\bar{n}_{\text{el}} \leq 1$), it is preferable to choose the electron's kinetic energy such that the condition

$$\Lambda_{el}(E) \geq t \tag{3.8}$$

is fulfilled. This ensures that the electron undergoes at most only one elastic scattering event as it traverses the sample (on average). Additionally, because the ratio of elastic to inelastic events is always larger than one[101], this means that, on average, no inelastic scattering occurs. This avoids electron-induced sample damage, as well as improving the quality of the diffraction data by reducing the diffuse background due to inelastic scattering.

There is one caveat to the condition defined in Eq.(3.8); if the electron energy is too large, $\Lambda_{\text{el}}(E) \gg t$, implying $\bar{n}_{\text{el}} \to 0$, meaning that most electrons do not scatter at all. This would not make for a very efficient UED experiment! As such, it is instead preferable that $\Lambda_{\text{el}}(E) \approx t$, so that most electrons scatter elastically once.

Fig. 3.3 plots both the elastic and inelastic mean free paths for electrons in several common materials. The mean free paths were calculated using the definition

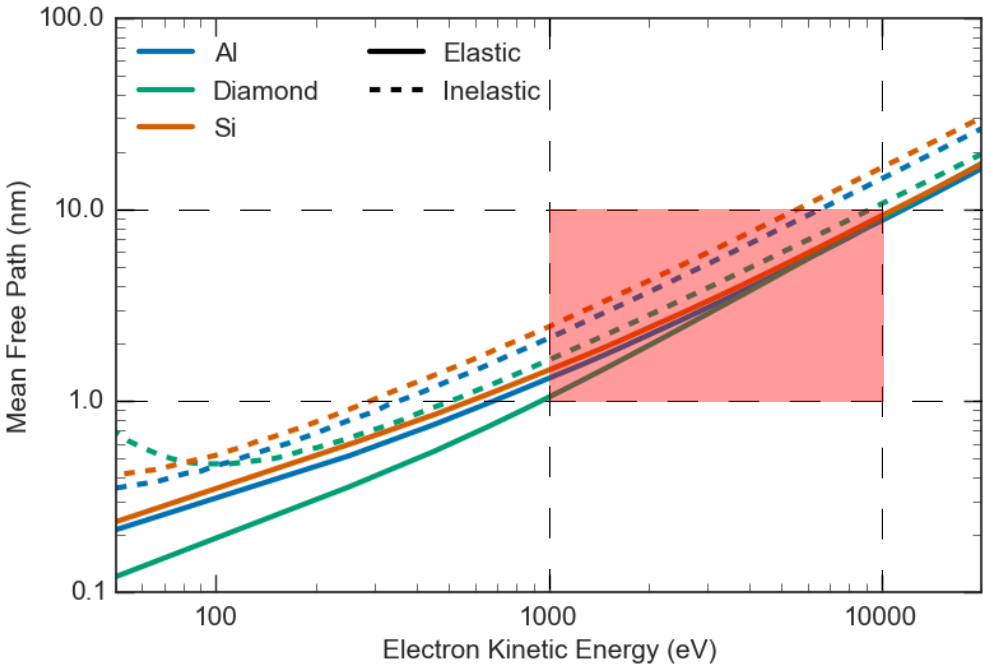


FIGURE 3.3.: *Comparison of the energy dependence of the elastic (solid lines) and inelastic (dashed lines) mean free path of several materials. The shaded area indicates the operating region for ultrafast electron diffraction of thin films and monolayers. The mean free paths were calculated using Eq.(3.9) with elastic scattering cross sections from ref. 102, inelastic scattering cross sections from ref. 103, and number densities from ref. 104.*

$$\Lambda_{\mathrm{el/inel}}(E) \equiv \frac{1}{\eta \sigma_{\mathrm{el/inel}}(E)} \tag{3.9}$$

where $\eta$ is the number density of the sample (number of scatterers per unit volume) and $\sigma_{\mathrm{el/inel}}$ is the elastic/inelastic scattering cross section. Because the targets of the UED system presented in this chapter are extremely thin films and monolayers, the sample thickness is on the order of a few nanometers. Taking 1 nm as a typical thickness (corresponding to a few monolayers), condition Eq.(3.8) thus requires $\Lambda_{\mathrm{el}}(E) \geq 1\,\mathrm{nm}$, which, according to Fig. 3.3, limits the the electron's kinetic energy to $> 1\,\mathrm{keV}$. In light of this, the UED system presented in this chapter is designed to operate in the range $1 - 10\,\mathrm{kV}$ and it was this that guided the design of the electron gun presented in the following sections.

### Photocathode

The electron beam is produced by photoemission from a metal cathode. In a widely adopted model[105], this can be envisioned to occur in three steps:

1. Optical excitation of an electron in the cathode material

2. Transport of the excited electrons to the cathode-vacuum interface. Scattering due to phonons, electrons, and impurities occurs during this step. In metal cathodes, electron-electron scattering is the dominant mechanism.

3. Escape through the energy barrier into the vacuum

Gold was chosen as the photocathode material for two reasons: first, due to the design of the UED setup, the photocathode is illuminated from the back. While this is known to produce slightly inferior beam properties compared to front-illuminated photocathodes[106], the small cathode-anode spacing of the electron gun design inhibits front-illumination (see Section 3.5). For back-illumination, it is preferable to have a thin cathode as this minimizes the scattering in the material (Step 2), thus enabling the creation of a better quality electron beam. In a simple model, the relationship between the film thickness $D$ and the photoemission yield is[107]

$$I \propto \frac{\alpha\Lambda}{1-\alpha\Lambda}\left[e^{-\alpha D} - e^{-\frac{D}{\Lambda}}\right] \tag{3.10}$$

where $\alpha$ is the absorption coefficient at the probe wavelength and $\Lambda$ is the inelastic mean free path of electrons in the cathode. Using typical value for UV light and gold[108], this function is peaked around about 10 nm. Gold facilitates this requirement since it is relatively easy to produce amorphous gold films down to a few tens of nanometers with thermal evaporation deposition.

The second reason for choosing gold can also be explained in reference to the three-step model: in order for electrons to escape the energy barrier in Step 3, they must be excited with energy above the barrier height (which, in this case, is the work function less any lowering due to the Schottky effect). As will be presented in the following section, the probe laser in the UED setup was the third-harmonic of a Ti-sapphire laser with a wavelength of $266.\overline{6}$ nm, corresponding to a photon energy of $E_{ph} = 4.65$ eV. Thin, amorphous gold has an effective work function of around 4.3 eV (ref. 107, 109), and so electrons can be given sufficient energy to escape into the vacuum.

It is important to note that if the electrons have energies significantly above the effective work function of the material, the emitted electron beam will have a relatively large energy spread. Since this translates to reduced temporal resolution and coherence length, among other things, it is desirable to have a cathode material with a work function very close to the probe laser's photon energy. To explore this further, a chromium cathode (with a work function around 4.5 eV, ref. 110) was tried, but was observed that it oxidized so quickly under ambient conditions (during the transfer from the evaporation deposition machine to the UHV chamber) that it did not produce electrons. Gold was found to be dramatically more robust and longer lasting.

A quartz (UV fused silica) substrate was used to mount the thin gold cathode. This was chosen over the traditional sapphire substrate[21] because of quartz's much higher transmission of UV light. Unfortunately, gold does not adhere to quartz (or sapphire) very well, and so a thin, 3 nm layer of chromium was first coated on the substrate. The gold thickness was 20 nm. Coating was performed in an evaporation deposition machine, in which a pellet of the desired metal was heated in a vacuum, resulting in a vapour that the substrate was exposed to. The rate of film growth was measured with a quartz oscillator (INFICON).

#### Anode

For the range of acceleration voltages used in the UED machine, significant distortions in the electron beam shape were observed when using a traditional anode, which is simply a flat metallic plate with a small aperture in it. The inhomogeneous penetration of the accelerating electric field into the aperture is known to cause a defocusing effect[111] which accounts for the observed distortions. To mitigate this, the finest available mesh (2000 lines per inch, Ted Pella) was laid over the anode's aperture. Each hole in the mesh has a similar lensing behaviour, but the overall effect, resulting from the contribution from all the holes in the mesh, results in significantly less divergence[109]. In fact, it was found that this completely removed the observed distortions. This effect is only relevant on the energy-scale considered here (i.e. $< 10$ kV), since high-energy electrons pass the anode region so quickly that they are unaffected by its defocusing effect.

### 3.3.2. Optics

Optical lasers serve two purposes in UED setups: first, they are responsible for the generation of the electron pulses from the cathode via the photoelectric effect. Second, they trigger the dynamics in the sample under study. By the same principle that guarantees no jitter in optical pump-probe experiments (see Chapter 1), both these pump and probe beams were derived from the same laser source.

The laser used with the UED setup presented in this chapter consisted of a Ti-sapphire oscillator (Micra-5, Coherent Inc.) and a single-pass regenerative amplifier (Legend Elite, Coherent Inc.). This system output 4 mJ per pulse at a fundamental wavelength of 800 nm and could operate at repetition rates up to 1 kHz. The pulse duration at the output of the amplifier was 40 fs (full-width at half-maximum), as quoted by the manufacturer and confirmed in an independent frequency-resolved optical gating (FROG) experiment[112].

### Probe Arm

Because the electrons are produced via the photoelectric effect, the quality of the probe laser directly influences the quality of the electron beam. Therefore, it is important that the properties of the probe beam at the cathode be well characterized.

As mentioned in the previous section, the probe laser arm was derived from the third harmonic of the fundamental, resulting in a wavelength of $(800/3)\text{nm} = 266.\overline{6}\,\text{nm}$. This was achieved by nonlinear processes in a series of birefringent crystals (see Fig. 3.4). After passing through an 8:3 telescope, the fundamental was passed through a 100 µm $\beta$-Barium borate (BBO*) crystal cut at 29.2° to enable Type I Second Harmonic Generation (SHG), producing extraordinary 400 nm light. To achieve Third Harmonic Generation (THG), the fundamental was then mixed with the resulting 400 nm in a second 100 µm BBO but at 44.3° to enable Type I Sum Frequency Generation (SFG). This required the use of a 1 mm calcite plate to compensate the group velocity delay between the 800 nm and the 400 nm, and a dual wavelength waveplate, resulting in a $\lambda/2$ phase-shift at 800 nm and a $\lambda$ phase-shift at 400 nm to get the desired polarization. Although it involved slightly more supporting optics, this scheme was chosen over Type II SFG (in which case the waveplate is unnecessary) due to the higher effective nonlinear coefficient for BBO, resulting in more efficient THG.

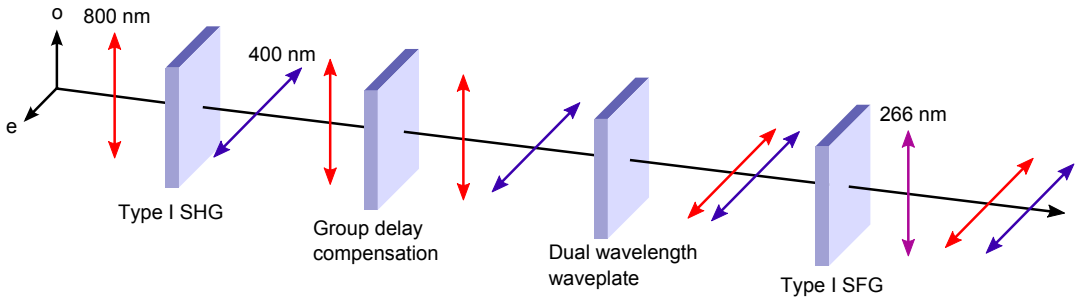


Figure 3.4.: *Illustration of the third-harmonic generation scheme used for the pump and probe arms. The fundamental (800 nm), polarized along the ordinary axis, passes through a thin BBO nonlinear crystal cut for Type I phase matching to produce the second-harmonic (400 nm). The mismatch between the beam's group velocities is then compensated with a calcite crystal, and the polarization of the (400 nm) is rotated with a dual wavelength waveplate. The third-harmonic ($266.\overline{6}$ nm) is finally produced via Type I sum frequency generation in a second BBO.*

To get an estimate of the probe laser's pulse duration and the efficiency of the THG, this whole process was simulated in SNLO[113], which uses a split-step Fourier method to solve the nonlinear Schödinger equation. The optical properties of the BBO used in the simulation are listed in Table 3.1, and the results of the simulation are shown in Fig. 3.5. The simulations show a conversion efficiency of 7.5 %, which exactly matches what was measured experimentally. The simulated pulse duration directly after the THG setup is about 30 fs Full-Width

* All the optics used for THG were purchased from Newlight Photonics.

at Half-Maximum (FWHM), although this value is very sensitive to dispersion, as mentioned below.

The pulse duration at the photocathode must account for any additional dispersion due to the UV probe propagating through the focusing lens, vacuum chamber window, and cathode substrate. These were all made of UV fused silica, which has a group-velocity dispersion (GVD) $D$ of 196.48 $\mathrm{fs}^2/\mathrm{mm}$ (ref. 114). For an initial FWHM pulse duration of $\tau_0 = 30\,\mathrm{fs}$, the pulse duration at the cathode is[115]:

$$\tau = \tau_0 \sqrt{1 + \left(\frac{4\ln(2)DL}{\tau_0^2}\right)^2} \tag{3.11}$$

where $L \approx 9\,\mathrm{mm}$ is the combined thickness of all the components. Performing the calculation gives a final FWHM pulse duration of $\sim 165\,\mathrm{fs}$.

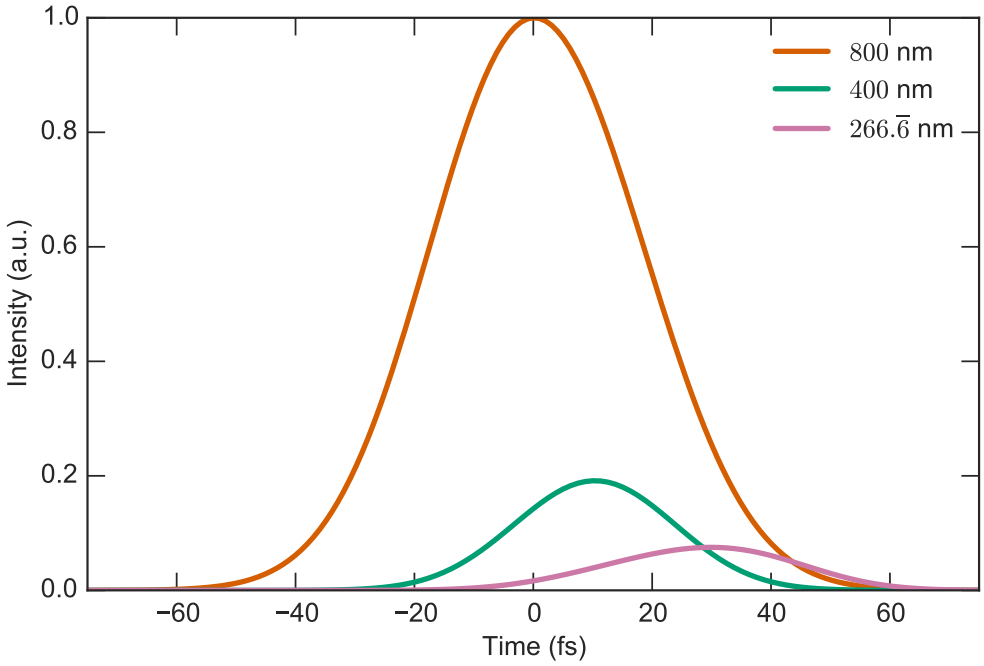


Figure 3.5.: *Simulated second and third harmonic pulses of a femtosecond laser passing through thin BBO crystals with SNLO. See the main text and Table 3.1 for the parameters of the simulation.*

It is evident from Fig. 3.4 that a significant amount of fundamental and second-harmonic are still present in the beam after THG. To filter these unwanted components, the probe beam was reflected off of a series of highly reflecting UV beam splitters (CVI Melles Griot, $> 99\,\%$ at 270 nm and $< 0.5\,\%$ at both 405 nm and 810 nm). The effect of the spectrum on the number of reflections is shown in Fig. 3.6. From this it is evident that at least 4 reflections are required to have a sufficiently filtered UV probe beam.

Table 3.1.: *Optical properties of β-Barium borate (BBO) at room temperature*

| | Type I SHG | | | Type I SFG | | |
|---|---|---|---|---|---|---|
| | $800.0 + 800.0 = 400.0$ | | | $800.0 + 400.0 = 266.\overline{6}$ | | |
| Polarization | o | o | e | o | o | e |
| Phase velocities (c/) | 1.660 | 1.660 | 1.660 | 1.660 | 1.693 | 1.682 |
| Group velocities (c/) | 1.685 | 1.685 | 1.743 | 1.685 | 1.783 | 1.906 |
| Group delay dispersion ($fs^2$/mm) | 75.1 | 75.1 | 195.9 | 75.1 | 215.2 | 437.1 |
| Phase-matching angle | | 29.2° | | | 44.3° | |
| Nonlinear coefficient, $d_{eff}$ (pm/V) | | 2.0 | | | 1.87 | |
| Crystal thickness, (µm) | | 100 | | | 100 | |

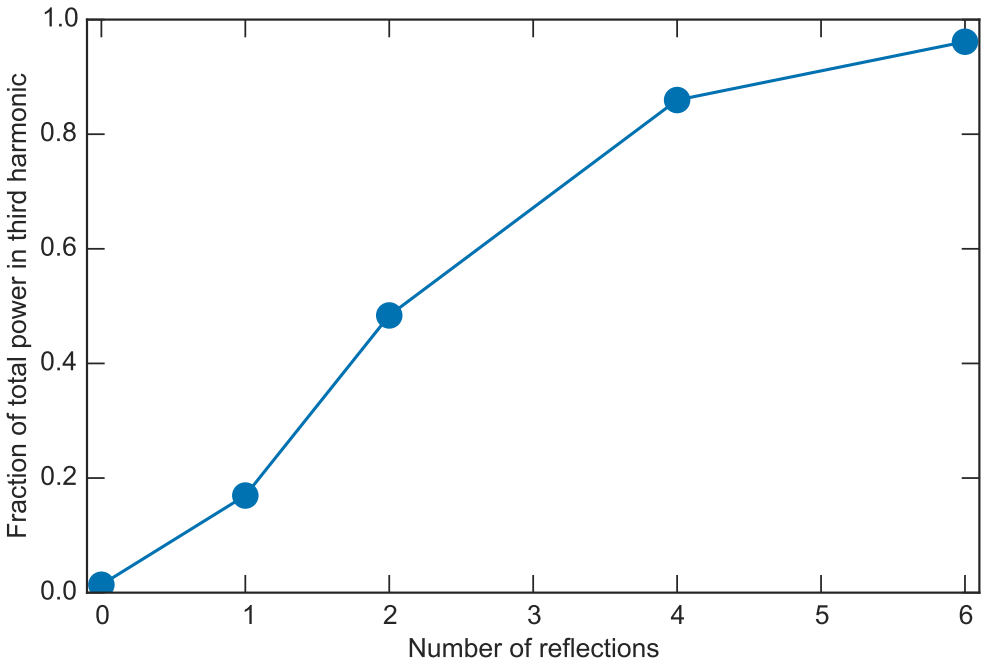


Figure 3.6.: *The effect of the number of reflections from ultraviolet beam splitters on the fraction of the total power contained in the third harmonic (*$266.\overline{6}$ *nm)*

The probe laser's spot size on the cathode can be calculated in the framework of Gaussian optics. For a beam of $1/e^2$ radius $w$ illuminating a lens of focal length $f$, the radius at the focus will be[116]

$$w_0 = \frac{w}{\sqrt{1 + \left(\frac{\pi w^2}{\lambda R}\right)^2}} \tag{3.12}$$

where $R$ is the radius of curvature of the beam just after the lens. This is determined by the lens equation $R^{-1} = R_0^{-1} - f^{-1}$, where $R_0$ is the radius of curvature of the incident

beam. For a well-collimated beam, $R \approx -f$. For the probe laser of $266.\overline{6}$ nm focused through an $f = 300\,\text{mm}$ lens and a measured radius of 1.1 mm (at $1/e^2$ intensity), it is found that the spot size on the cathode has a radius of $w_0 \approx 23\,\mu\text{m}$. The corresponding standard deviation and FWHM* are given by 11.5 µm and 27 µm, respectively. This size was not verified experimentally due to the difficulty of measuring the beam size in the cathode plane. However, the electron beam size was measured (see Section 3.5), which is ultimately the quantity of interest.

### Pump Arm

The wavelength of the pump must be tuned so that the photon energy is resonant with desired transition in the sample. The experiments discussed in Chapter 4, which used the UED machine presented here, required UV wavelengths, and so the third harmonic of the fundamental was used. This was achieved using the same scheme that was used for the probe (see Fig. 3.4), and so will not be discussed again here. Some experiments additionally used the fundamental directly.

Because most sample's dynamics are highly dependent on the excitation fluence, it is important to know the size of the pump in the sample plane. This was measured by a variation of the well-known knife-edge method, in which the laser's power is measured as part of the beam is blocked with a sharp blade. As the blade is translated across the beam, the power measurement traces out the accumulated intensity of the beam. In the case of the system presented here, mounting a knife-edge was not possible, and so a 70 µm diameter aperture was scanned across the beam instead. Mathematically, this process can be described as follows: suppose the intensity distribution can be written as $I(x, y) = I_0 \exp\left[-(x^2 + y^2)/w_0^2\right]$ where $I_0$ is the peak intensity and $w_0$ is the beam waist (twice the standard deviation), and a circular aperture with diameter $d$ can be represented by the transmission function $t(x, y) = 1$ if $\sqrt{x^2 + y^2} \leq d/2$ and $t(x, y) = 0$ otherwise. As the aperture is translated along one of the axes, say the $x$-axis, the measured power is then

$$P(x_0) = \int_{-\infty}^{\infty} \int_{-\infty}^{\infty} I(x, y) t(x - x_0, y)\, \mathrm{d}x\, \mathrm{d}y \tag{3.13}$$

The results of such a measurement are shown in Fig. 3.7, with Eq.(3.13) having been numerically integrated to obtain the fit. It was found that, at the sample position, the pump beam FWHM was $\sim 310\,\mu\text{m}$, corresponding to a standard deviation of $\sim 130\,\mu\text{m}$.

* For a beam with a $1/e^2$ radius of $w$, the standard deviation and FWHM are given by $0.5w$ and $\sqrt{2\ln(2)}w$, respectively.

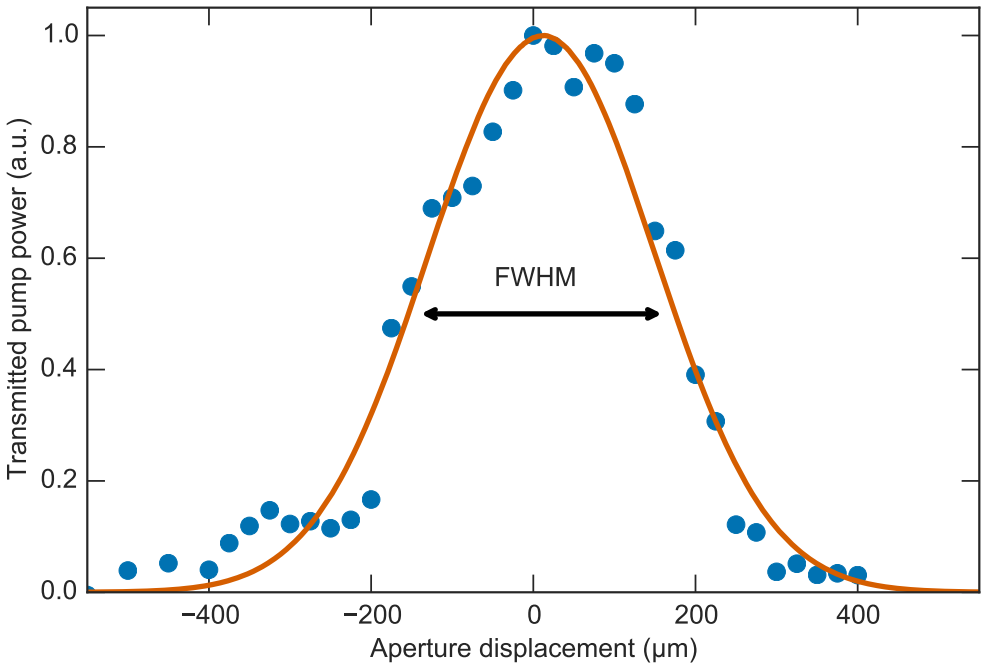


Figure 3.7.: *Transmitted power of the pump laser passing through an aperture scanned across the beam*

### 3.3.3. Delay Stage

As with the optical pump-probe experiment presented in Chapter 2, time resolution is achieved in UED experiments by varying the arrival time between the pump and the probe. In practice, this is accomplished by increasing the path length of one of the laser arms by reflecting the beam from a retroreflector mounted on a linear translation stage. The probe beam was chosen to be delayed so that if the pump wavelength was changed for different experiments, the retroreflector would not need to be replaced with another with a more suitable material.

It is imperative that the delay stage be extremely well aligned so that the electron bunch properties are agnostic to the delay stage position. Otherwise it would be extremely challenging, if not impossible, to associate time-dependent changes in the diffraction pattern to changes in the electron beam or dynamics in the sample. Alignment was achieved by mounting an iris in front of the retroreflector and trying to obtain the same power transmission through the iris at all delay stage positions. It was not uncommon to see a small amount of decreased laser intensity when the delay stage was moved from one end to the other due to beam divergence; however, with careful alignment, this change was $< 1\,\%$ over 300 mm.

### 3.3.4. Ultrahigh Vacuum Chamber

There are three reasons why UED experiments must be performed in ultrahigh vacuum (UHV) conditions:

1. An extremely high electric field, on the order of $10^6\,\mathrm{V/m}$ or higher, is present between the cathode and the anode due to the small gap between them. As a consequence of this, any residual gas in the chamber can lead to "breakdown", a phenomenon in which the vacuum suddenly changes from an insulating to a highly conducting state and arcing occurs. Such arcing can strip the gold coating from the cathode or damage the power supply by creating a short circuit.

2. As the electron bunches propagate toward the sample, they can undergo scattering with any residual gas molecules in the chamber. This has detrimental effects on the bunch's pulse duration, coherence length, and size, all of which degrade the quality of the experiment. As such, it is desirable that the electrons do not interact with the residual gas at all. The average distance that an electron propagating through a gas at pressure $P$ and temperature $T$ travels before it scatters is the mean free path[117]

$$\Lambda = \frac{k_\mathrm{B}T}{4\pi\sqrt{2}r^2P} \tag{3.14}$$

   where $k_\mathrm{B} = 1.38 \times 10^{-23}\,\mathrm{kg\,m^2\,s^{-2}\,K^{-1}}$ is Boltzmann's constant and $r$ is the radius of the gas molecules. This distance must be significantly larger than the source-detector separation, and because it is a statistical quantity, several order of magnitude larger is preferable. As an illustrative calculation, at a pressure of $P = 10^{-6}\,\mathrm{mbar}$ an electron's mean free path in nitrogen is $\sim 400\,\mathrm{m}$.

3. In addition to the probe properties, the sample properties can be significantly influenced when exposed to inadequate vacuum levels. In particular, the sample's surface quickly becomes contaminated with adsorbate. This is governed by the Hertz-Knudsen formula for the flux $F$ of gas molecules onto the sample's surface[118]:

$$F = \frac{\alpha P}{\sqrt{2\pi m k_\mathrm{B}T}} \tag{3.15}$$

   where $m$ is the molecular mass of the gas. Since this has units of $\mathrm{molecules\times m^{-2}\,s^{-1}}$, it can be used to estimate how long it takes for the sample to be fully covered by a monolayer of gas molecules. Assuming every molecular that hits the surface sticks, and taking $10^{19}$ molecules/$\mathrm{m^2}$ as a typical monolayer coverage[119], it only takes $1\,\mathrm{s}$ for a monolayer to form at $10^{-6}\,\mathrm{mbar}$, and $10^4\,\mathrm{s}$ at $10^{-10}\,\mathrm{mbar}$.

Adequate vacuum pressure of $10^{-8}\,\mathrm{mbar}$ satisfying the above three conditions was achieved by pumping with a turbo pump backed by a roughing pump (HiCube 80, Pfeiffer Vacuum)

in combination with an ion pump (25S Titan, Gamma Vacuum, typical operating current = 10 µA). For optimum conditions, the chamber was baked overnight to $< 100\,^{\circ}\mathrm{C}$. To avoid having to regularly vent the chamber, a load-lock system was used to mount and transfer samples. During this process the chamber was flushed with an overpressure of $N_2$ gas (just over 1 atm) to minimize the amount of contaminants entering the chamber. This significantly reduced the pumping time required to achieve the desired level of vacuum once the chamber was closed again.

Because of the high voltages applied to the cathode and detector (see the following section), the chamber must be conditioned in order to avoid arcing. The following procedure was performed after every time the chamber had been exposed to atmosphere: once moderate vacuum pressure has been achieved ($< 10^{-6}$ mbar), the voltages were incrementally increased every 30 minutes (in steps of 0.5 kV on the cathode and phosphor screen and 0.1 kV on the microchannel plate). This was continued until the target voltages had been reached. Additionally, current to the cathode was limited to 0.03 mA to minimize the damage if arcing occurred.

### 3.3.5. Detection System

Detection of the diffracted electrons takes place in several sequential steps. First, the electrons are amplified through a Microchannel Plate (MCP), to compensate for the low number of electrons used in a typical experiment and to improve signal-to-noise. In addition, MCPs are known to increase the spatial resolution of detection[120].

The electrons were then converted to visible photons by a phosphor scintillator, and finally imaged with Charge-Coupled Device (CCD) camera, which was cooled to $-20\,^{\circ}\mathrm{C}$ to reduce electronic noise in the readout of the chip. The scintillator was coupled to the CCD sensor with a free-space lens as opposed to a fiber taper. While the former method is known to have poor coupling efficiency (typically $< 20\,\%$, ref. 121), lens coupling is distortion free and maintains the optical resolution. Noise due to ambient light in the room was minimized by building an enclosure around the phosphor screen, lens, and camera.

The scintillator was a P43 phosphor ($Gd_2O_2S$:Tb) powder which had a decay time of a few hundred microseconds[122]. To avoid residual fluorescence that would decrease the time resolution of the experiment, measurements were taken at a repetition rate of 1000 Hz. P43 phosphor was chosen for several reasons: its peak emission closely matches the peak sensitivity of the CCD chip ($\sim 550$ nm), it provides significantly higher conversion efficiency than other phosphors[123], and it has high spatial resolution due to its small grain size ($\sim 1$ µm, ref. 123).

To propagate the electrons through the MCP to the phosphor screen, an electric field was applied across the detection stack. Typical working voltages were 1.89 kV on the back of the MCP and 3.9 kV on the phosphor screen. Resistors (10 MΩ for the MCP and 40 MΩ for the phosphor) were placed between voltage source and target to limit the current in case of

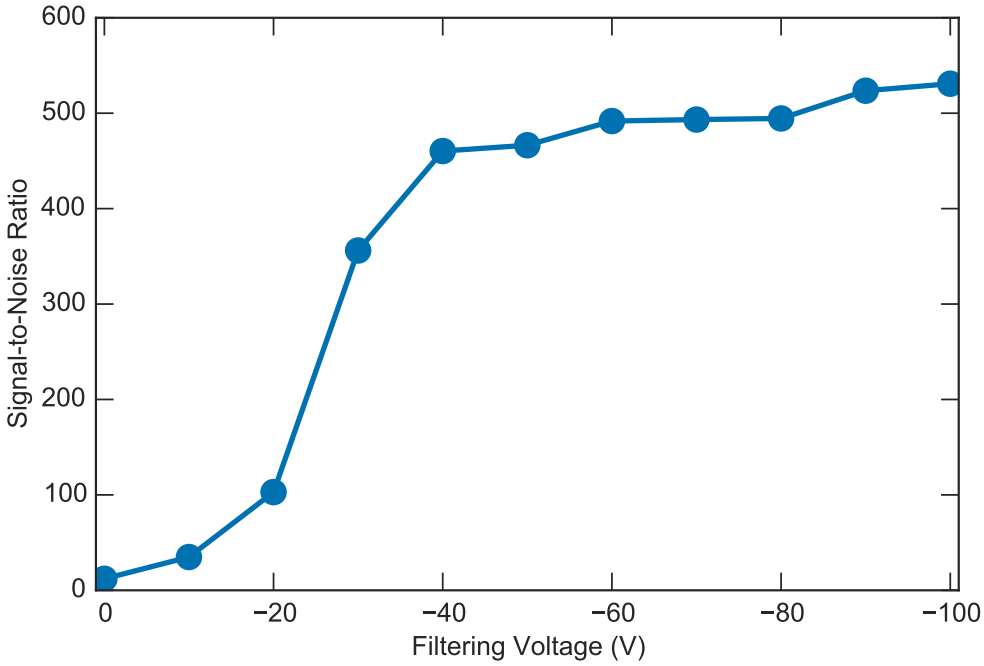


FIGURE 3.8.: *The dependence of the signal-to-noise ratio (defined as the intensity of the direct electron beam divided by the standard deviation of the noise) on the filtering voltage applied to the front of the microchannel plate*

arcing. A slight bias voltage of around −40 V was applied to the front face of the MCP to filter electrons with extremely low energy that are produced by stray pump light hitting metal surfaces within the chamber. This was found to dramatically reduce the noise, especially at high pump powers (see Fig. 3.8).

### 3.3.6. Timing and Data Acquisition

In principle, the order in which the images are measured should not matter; that is, the same dynamics should be observed if the pump-only, or probe-only, or pump-and-probe image is acquired first. Similarly, it should be inconsequential whether several complete runs are measured and then averaged, or if the data at each time delay is averaged several times prior to moving to the next delay time. Unfortunately, there is a consequence: due to long-term fluctuations in the laser power, these can lead to significantly differences in the quality of the experiment. This is demonstrated in Fig. 3.9, which shows fluctuations in the electron beam intensity for two different measurements sequences. As a conclusion, all experiments were performed in the "run first" mode. For the same reason, the data acquisition sequence at each time delay (pump, pump-probe, probe) was chosen to minimize the time between measurements involving the same laser pulse. Both of these approaches served to mitigate the influence of long-term drift in the laser power.

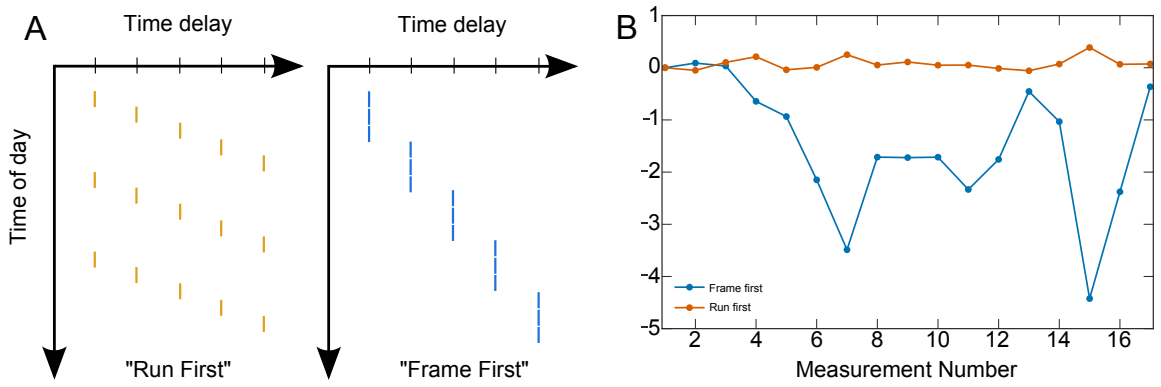


Figure 3.9.: *The variation in the electron beam intensity over a series of measurements (B) for two different data acquisition sequences (A)*

## 3.4. Simulations

To glean insight into the evolving phase-space distribution of the electron bunch and to have estimations of beam characteristics that are experimentally inaccessible, detailed simulations of the electron beam were performed with A Space Charge Tracking Algorithm (ASTRA)[124]. ASTRA is a sophisticated software suite that performs fully relativistic, non-quantum simulations of particle propagation through external electric and magnetic fields, while accounting for space-charge effects and other complex phenomena such as secondary electron emission and mirror charges at the cathode. A detailed description of its algorithm is available in the manual[124]; briefly, ASTRA performs $4^{\text{th}}$ order Runge-Kutta (RK4) time integration in a discretized, three-dimensional space. The full equation of motion of the position $\mathbf{r}_i$ of the $i^{\text{th}}$ electron is:

$$\frac{d^2\mathbf{r}_i}{dt^2} = \underbrace{\frac{q^2}{4\pi\epsilon_0 m_e}\sum_{j\neq i}^{N}\frac{1}{|\mathbf{r}_i-\mathbf{r}_i|^2}}_{\text{space-charge effects}} + \underbrace{\frac{q}{m_e}\left(\mathbf{E}+\mathbf{v}\times\mathbf{B}\right)}_{\text{external fields}} \tag{3.16}$$

where $\mathbf{E}$ and $\mathbf{B}$ are the external electric and magnetic fields, respectively, and $N$ is the total number of electrons. The RK4 method is commonly used in $N$-body simulations due to its speed, simplicity, and accuracy. To implement it, a phase-space coordinate $\mathbf{u}_i(t) = (\mathbf{r}_i(t), \mathbf{v}_i(t))$ is defined, and the trajectory in phase space evolves according to:

$$\frac{d\mathbf{u}_i}{dt} = f(\mathbf{u}_i,t) = \left(\mathbf{v}_i,\ \frac{q^2}{4\pi\epsilon_0 m_e}\sum_{j\neq i}^{N}\frac{1}{|\mathbf{r}_i-\mathbf{r}_i|^2} + \frac{q}{m_e}\left[\mathbf{E}(\mathbf{r}_i,t)+\mathbf{v}_i\times\mathbf{B}(\mathbf{r}_i,t)\right]\right) \tag{3.17}$$

The RK4 method approximates (3.17) as:

$$\vec{u}_i^{n+1} = \vec{u}_i^n + \frac{h}{6}(k_1 + 2k_2 + 2k_3 + k_4) \tag{3.18}$$

where the superscript $n$ denotes the iteration number, $h$ is a defined time step, and:

$$k_1 = f(\mathbf{u}_i^n, t^n) \tag{3.19a}$$
$$k_2 = f\left(\mathbf{u}_i^n + \frac{k_1}{2}, t^n + \frac{h}{2}\right) \tag{3.19b}$$
$$k_3 = f\left(\mathbf{u}_i^n + \frac{k_2}{2}, t^n + \frac{h}{2}\right) \tag{3.19c}$$
$$k_4 = f(\mathbf{u}_i^n + k_3, t^n + h) \tag{3.19d}$$

The input to the ASTRA simulation is the initial distribution of the electron bunch at the cathode, which is estimated from the measured properties of the probe laser beam. Spatially, the initial electron bunch was taken to be an uncorrelated, two-dimensional normal distribution with a FWHM of 27 µm, identically matching the spatial profile of the probe laser. The initial momentum distribution can be characterized under the confines of the three-step model for photoemission introduced in Section 3.3.1; doing so gives[125]:

$$\left(\sigma_{p_\perp}^0\right)^2 = \frac{\iiiint g(E,\theta,\phi) f(s,E,\theta,E_{ph}) p_\perp^2 \,\mathrm{d}E\,\mathrm{d}s\,\mathrm{d}(\cos\theta)\,\mathrm{d}\phi}{\iiiint g(E,\theta,\phi) f(s,E,\theta,E_{ph})\,\mathrm{d}E\,\mathrm{d}s\,\mathrm{d}(\cos\theta)\,\mathrm{d}\phi} \tag{3.20}$$

where $\sigma_{p_\perp}^0$ is the initial standard deviation of the transverse component of the momentum, $g(E,\theta,\phi)$ is the transition probability for an excited electron of energy $E$ to escape, $f(s,E,\theta,E_{ph})$ is the fraction of electrons per unit distance at a depth $s$ below the surface which survive scattering, and $(\theta,\phi)$ are the angular coordinates of the electron relative to the cathode's surface normal. Under the assumptions of the three-step model, the escape probability is governed by the fact that the distribution of occupied states in the cathode is given by the Fermi-Dirac function $f_{FD}(E)$. Explicitly, $g(E,\theta,\phi) = [1 - f_{FD}(E + E_{ph})]\, f_{FD}(E)$. In this case, the integrals in Eq.(3.20) can be calculated analytically to give

$$\sigma_{p_\perp}^0 = \sqrt{\frac{m_e\,(E_{ph} - \phi_{eff})}{3}} \tag{3.21}$$

This theory was used to randomly distribution the initial momenta of the electron bunch, the results of which are shown in Fig. 3.10. Also presented in this figure are the initial distributions of the other pertinent parameters for the simulation.

Temporally, the emission of the electrons from the cathode was taken to match the pulse profile of the probe laser, and so was taken to be normal with a 165 fs full-width at half-maximum (see Fig. 3.10 and refer to Fig. 3.5 for the temporal profile of the probe laser). A

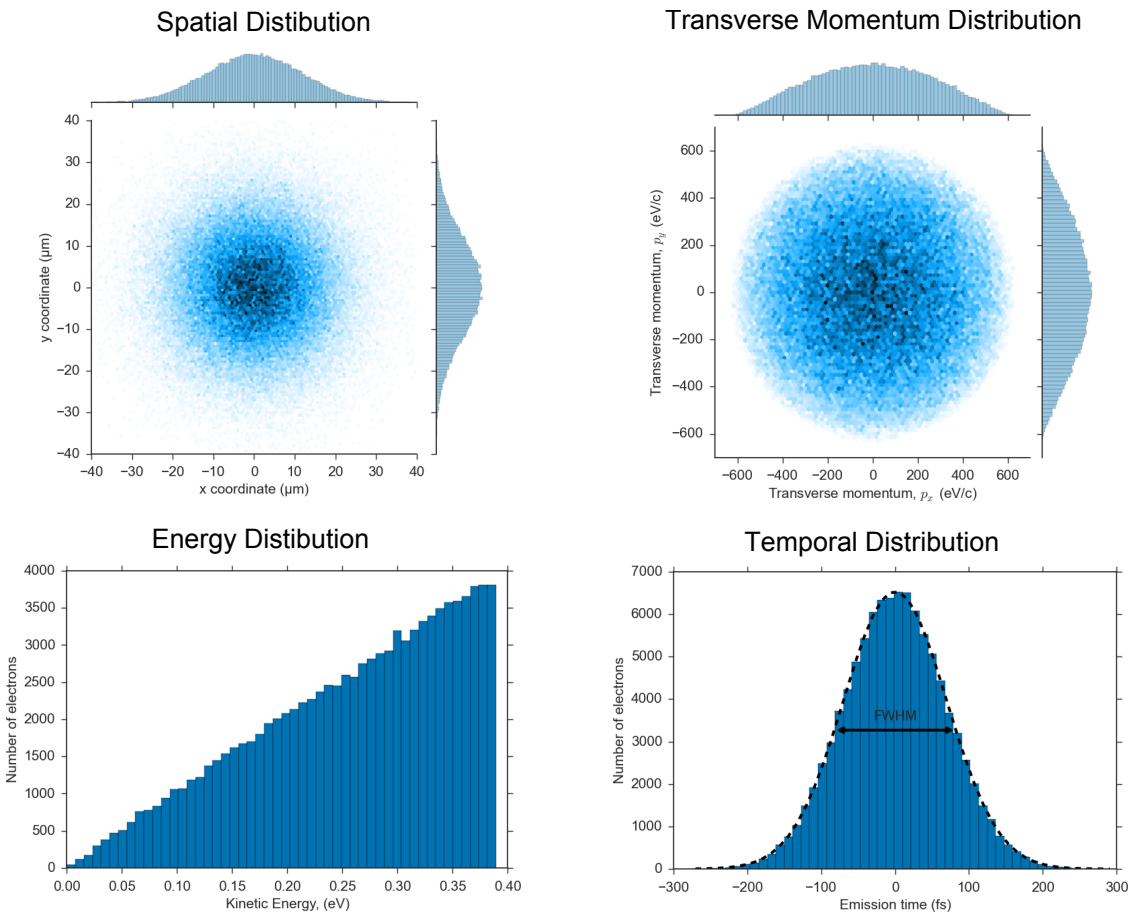


Figure 3.10.: *Simulated distributions of the initial parameters (at the cathode) of an electrons bunch in the ultrafast electron diffraction chamber. These values were used as the input for ASTRA.*

summary of the parameters used in the simulation can be found in Table 3.2.

Simulations were performed for various numbers of electrons in the bunch, ranging from $10^3 - 10^5$, and also with acceleration voltages in the range of 1 – 10 kV. Two of the most important beam parameters, the pulse duration and the transverse coherence length, where calculated at the sample position from the results of the simulation and are shown in Fig. 3.11.

The top panel, showing the electron bunch's pulse duration at the sample, reveals that it is possible to obtain sub-picosecond durations for low acceleration voltages if the number of electrons per pulse is kept low, as this minimizes the broadening due to space-charge effects. This is a promising result, and suggests the UED setup introduced in this chapter can achieve femtosecond temporal resolution with acceleration voltages of a few kilovolts ($> 1$ kV).

The transverse coherence length, presented in the bottom panel of Fig. 3.11 highlights the importance of the anode aperture on improving the electron beam properties. Because the aperture is so small (40 µm in diameter), a significant portion of the electrons are lost when

Table 3.2.: *Parameters for the simulation of the ultrafast, low-energy electron diffractometer using ASTRA*

| Parameter | Value |
|---|---|
| Laser pulse duration (FWHM) | 165 fs |
| Laser spot size on the cathode (FWHM) | 27 µm |
| Cathode-anode distance | 1 mm |
| Anode thickness | 0.25 mm |
| Anode-sample distance | 0.5 mm |
| Anode aperture radius | 20 µm |
| Electrons per pulse | $10^3 - 10^5$ |
| Charge per pulse | 0.1 – 10 fC |
| Acceleration voltage | 1 – 10kV |

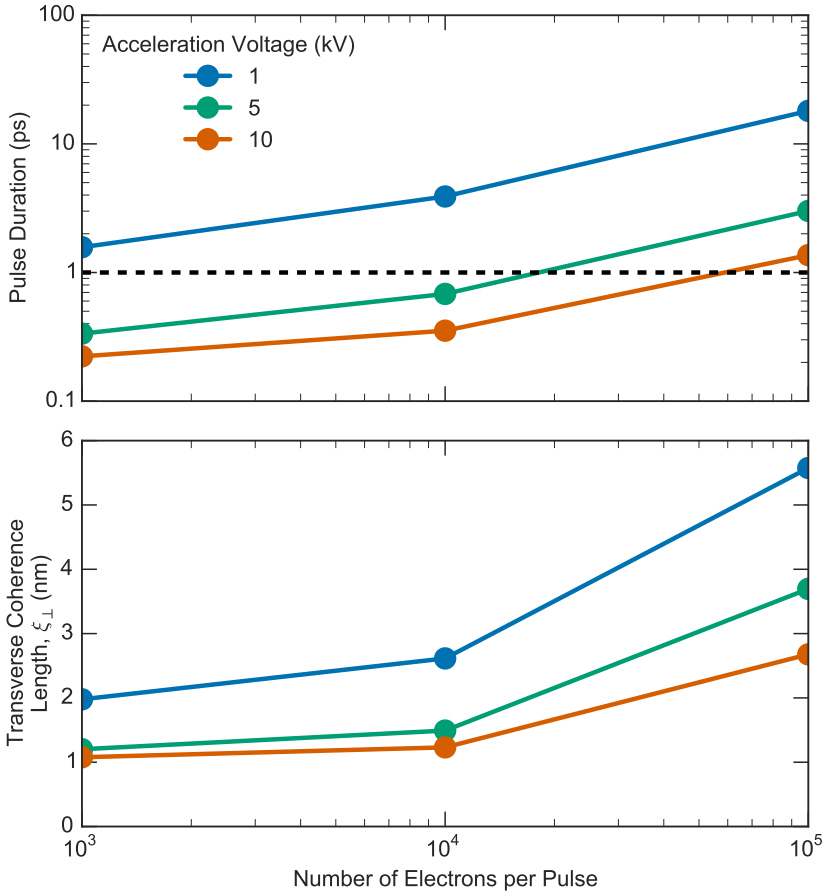


Figure 3.11.: *Electron bunch parameters at the sample location simulated by ASTRA*

the beam passes through the anode. The result is that the beam divergence significantly decreases, since only the electrons in the center of the beam survive (that is, those which are traveling the most in parallel). This can be used to explain why lower energy electron pulses

have a higher coherence length: because low energy electrons travel more slowly, they have significantly more time to broaden (recall the discussion in Section 3.3.1). As a consequence, the central portion of a low-energy beam is composed of less divergent electrons relative to a higher energy beam. This fact also explains the trend that more electrons results in a higher coherence length, since higher electron density means more divergence before the anode.

## 3.5. Experimental Apparatus and Characterization

Armed with the design principles outlined in Section 3.3 and the simulations of Section 3.4, this section will present the experimental UED system and the characterization of its properties. The final electron gun design, presented in Fig. 3.12, incorporates all the aspects mentioned above, such as the mesh over the anode plate. The gun was mounted on a linear translation stage to enable a variable source-sample distance. This is important for finding the spatial overlap (which will be discussed below) and also to have control over the electron pulse duration at the sample. The distance between the cathode and anode was fixed at 1 mm by a spacer, and, by using the translation stage, the gun could be position so that the sample holder was in contact with the anode. This resulted in an $\sim 0.5$ mm gap between the anode and the sample. Because of the small cathode-anode separation distance, the accelerating DC electric field was on the order of $1 - 10$ MV/m depending on the cathode bias.

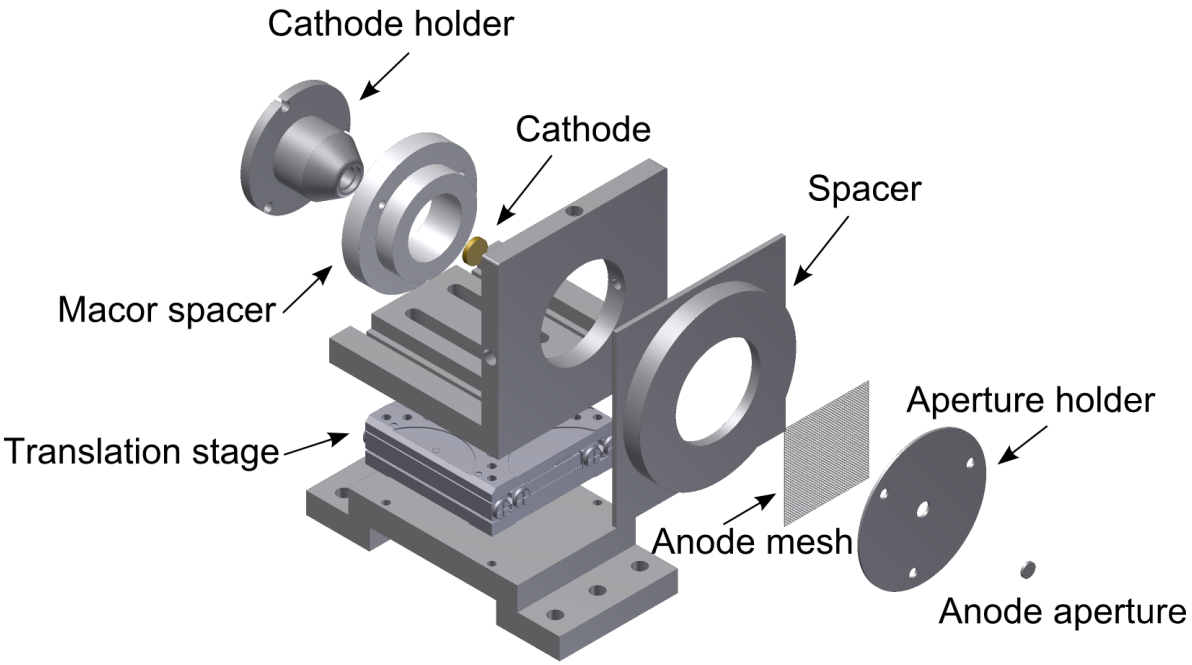


Figure 3.12.: *Simplified exploded drawing of the electron gun*

Fig. 3.13 shows a photograph of the experimental UED chamber. All aspects of the design, such as the vacuum pumps and load-lock system, are present. Not visible in this picture

are an ion gauge used to continuously monitor that vacuum pressure, and a series of power supplies to provide high voltage to the electron gun, MCP, and phosphor screen.

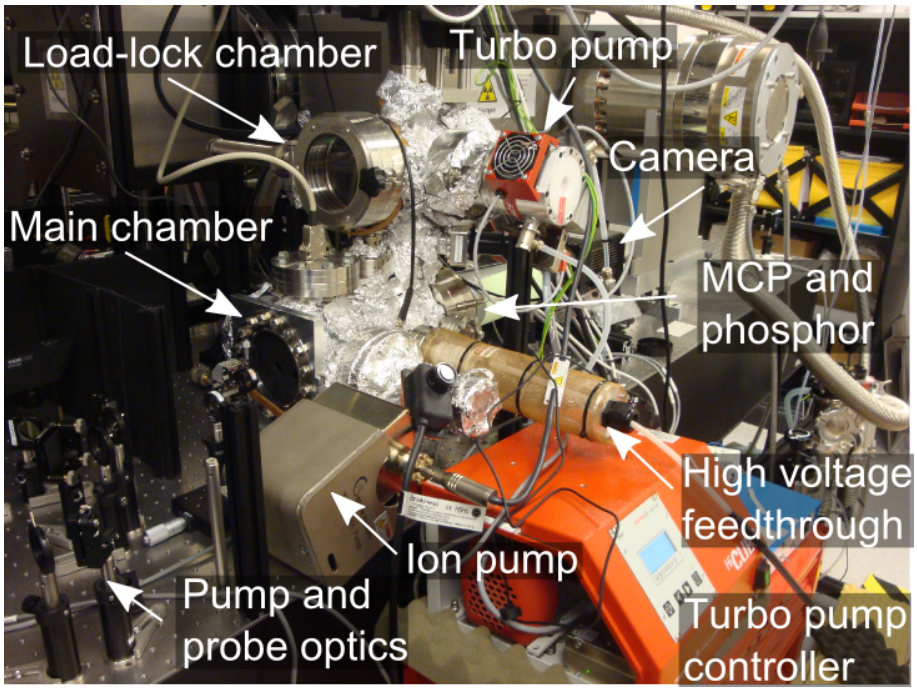


Figure 3.13.: *Photograph of the ultrafast low-energy electron diffractometer setup with each individual component identified*

A typical diffraction pattern from graphene mounted on a copper mesh coated with lacey carbon is shown in Fig. 3.14 (B). To provide a point of reference on the quality of the diffraction, Fig. 3.14 (A) shows a diffraction pattern from the same sample taken in a Philips CM12 transmission electron microscope (TEM) operating at 80 kV. It is evident that the UED system presented here is capable of comparable diffraction quality and signal-to-noise. The diffraction spots are slightly larger, indicative of a small transverse coherence length of the UED system compared with the TEM. However, the UED system can obtain such quality images with sub-picosecond time-resolution (see Fig. 3.11). For graphene, diffraction past the third order was observed.

The following sections will present some characterizations of the system, all of which were performed with an acceleration voltage of 6 kV.

### 3.5.1. Electron Beam Size

The size of the electron beam was measured in a manor identical to the way the pump beam was measured in Section 3.3.2. The results of this measurement are shown in Fig. 3.15, and by fitting with Eq.(3.13) it was found that the standard deviation of the beam was $\sim 30\,\mu m$ (standard deviation), corresponding to a FWHM of $\sim 70\,\mu m$.

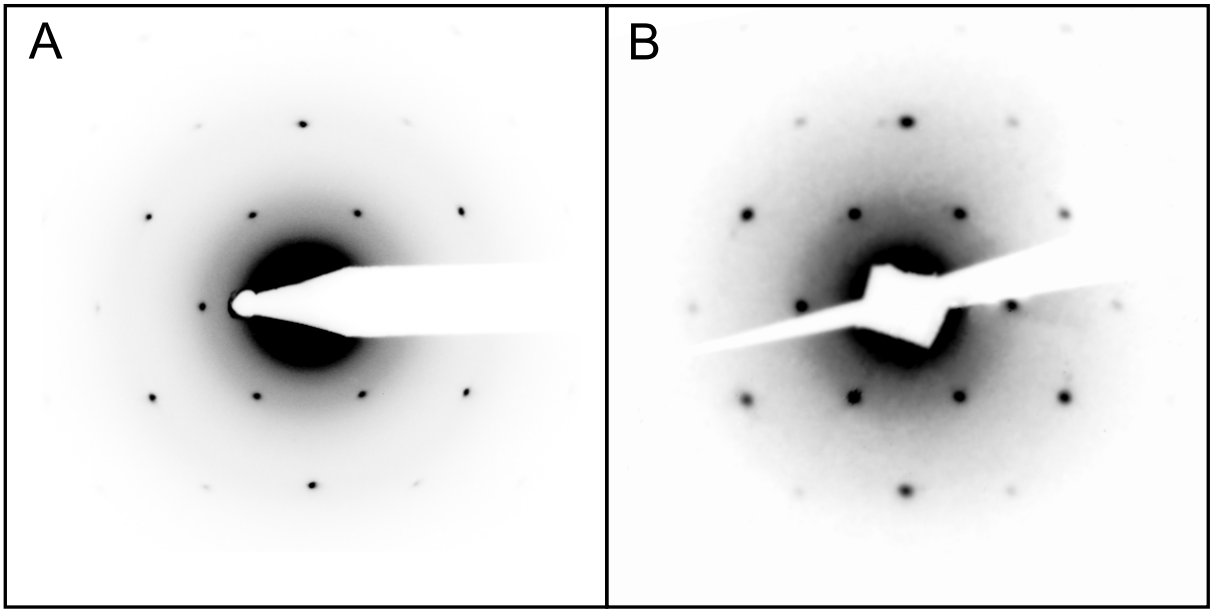


Figure 3.14.: *Comparison of the diffraction pattern of graphene on a copper mesh coated with a lacey carbon film taken with (A) a transmission electron microscope and (B) the ultrafast low-energy electron diffractometer*

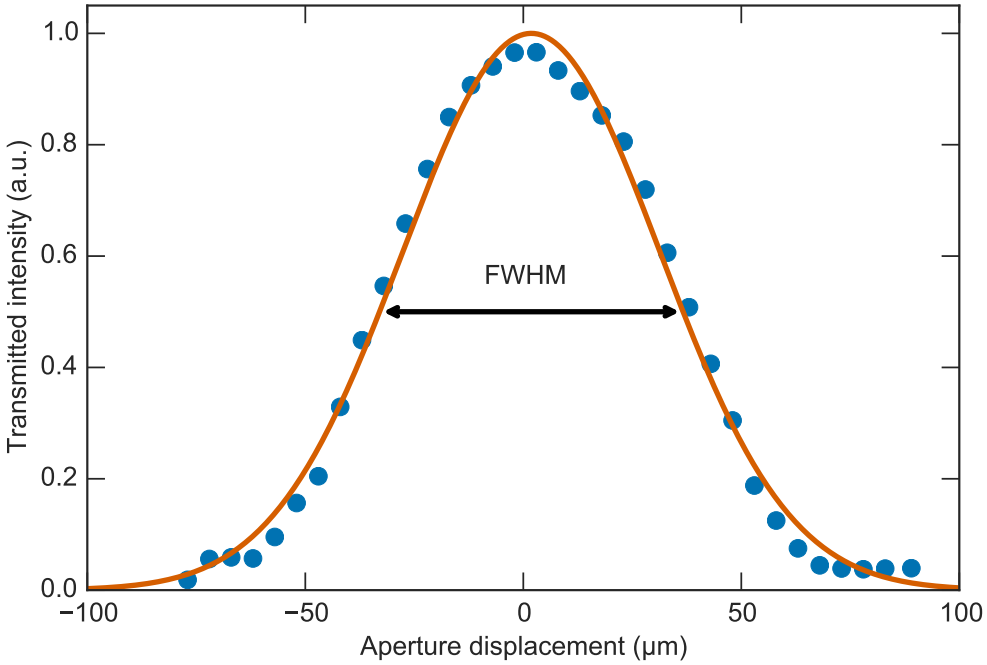


Figure 3.15.: *Transmitted power of the electron beam passing through an aperture scanned across the beam*

### 3.5.2. Transverse Coherence Length

The transverse coherence length can be estimated from the diffraction pattern of a sample with a known structure as follows: recalling the discussion in Section 3.2, the transverse coherence length is roughly the length-scale over which the sample is coherently illuminated. If this corresponds to $N$ unit cells, then $\xi_\perp = Na$, where $a$ is the unit cell parameter of the sample. According to Eq.(3.5), the location of the diffraction peaks are governed by the Bragg condition (when the denominator of the intensity vanishes):

$$q_m^{Bragg} = \frac{2m\pi}{a}, \quad m \in \mathbb{Z} \tag{3.22}$$

Here $m$ is the diffraction order, and it is important to note that the peak position does not depend on the number of unit cells $N$ in the coherence area. On the other hand, the width of a peak *does* depend on $N$; to see this, observe that the zeros in the diffraction pattern occur when the numerator of Eq.(3.5) is zero:

$$q_n^{min} = \frac{2n\pi}{Na}, \quad n \in \mathbb{Z} \tag{3.23}$$

where $n$ is not an integer multiple of $N$. If the peak is sufficiently narrow that it can be represented as a triangle, then its FWHM can be estimated as $\Delta q_m \approx (q_{m+1}^{min} - q_{m-1}^{min})/2 = 2\pi/Na$. Notably, the peak width does not depend on the diffraction order, and so all peaks should all have the same width $\Delta q$.

If the ratio of the distance between neighbouring peaks (say the $m^{\text{th}}$ and $(m+1)^{\text{th}}$) to the peak width is constructed, an interesting result is obtained:

$$\frac{q_{m+1}^{Bragg} - q_m^{Bragg}}{\Delta q} = N \tag{3.24}$$

Finally, a method to measure the transverse coherence length of the electron beam has been arrived at: recalling that the number $N$ was defined as the number of unit cells within the coherence length, if the quantity defined in Eq.(3.24) is measured, then the transverse coherence length can be calculated as $\xi_\perp = a\frac{q_{m+1}^{max} - q_m^{max}}{\Delta q}$.

This analysis was performed on a typical diffraction pattern from graphene, shown in Fig. 3.16 (A), using the two peaks shown in the highlighted rectangle. Calculating the FWHM of the peaks in the line profile (Fig. 3.16 (B)) results in a coherence length of $\sim 3.3\,\text{nm}$. Of course this value needs to be taken with a grain of salt due to the approximations in its calculation. That being said, it is comparable to state-of-the-art UED machines[22], and, since it spans tens of unit cells for most inorganic solids, is sufficient for UED experiments. The measured value very closely matches the ASTRA results (see the lower panel of Fig. 3.11), a fact which both validates the simulation and the measurement.

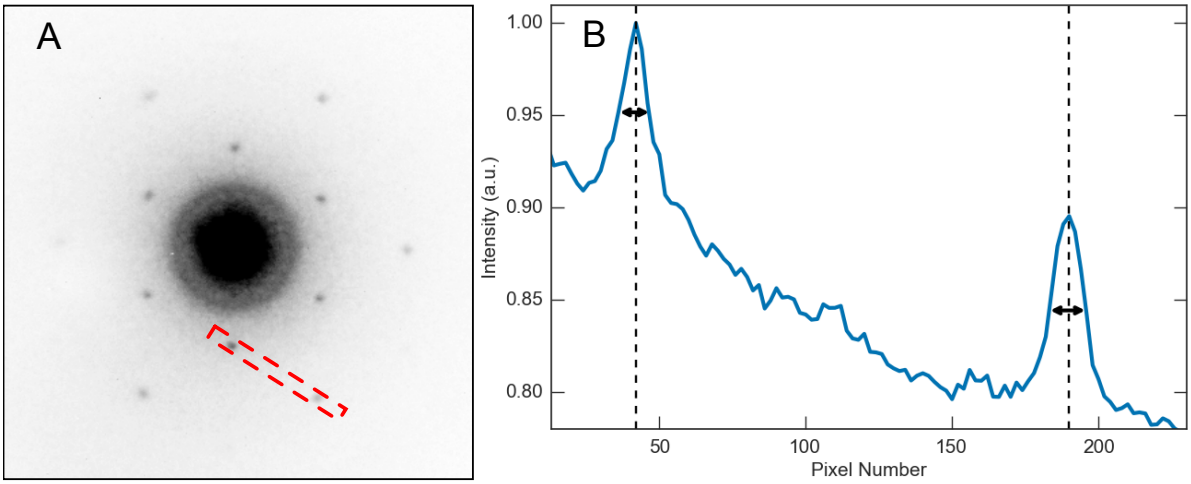


Figure 3.16.: *Method to measure the transverse coherence length of the ultrafast electron diffractometer. A diffraction pattern from a sample with a known crystal structure (in this case, graphene) is shown in (A). The widths and locations of neighbouring Bragg peaks were used to estimate the transverse coherence length (B).*

### 3.5.3. Spatial and Temporal Overlap

A suitable procedure was devised to align the pump laser to obtain spatial overlap between the pump and the probe electrons. First, a small aperture was mounted into the sample holder and positioned to maximize the intensity of the transmitted electron beam. In this way, the location of the aperture marks the electron beam's position in the sample plane. A 70 µm diameter aperture was used for this purpose. Then, the pump laser was aligned so that it too passed through the aperture (this was done by retracting the electron gun from the sample and looking for scattering of the pump from the back of the anode, which would only be possible if the pump had first passed through the aperture). In this way, it could be assured that the pump and probe overlapped in space at the sample position.

To find the temporal overlap, that is, the position of the delay stage for which the pump and probe arrive at the sample simultaneously, the established ultrafast plasma formation technique was used[126,127]. Although this process will be the subject of an entire chapter (Chapter 4), the underlying physics will be briefly presented here: when a metal surface is irradiated by an intense femtosecond laser, one of the processes that occurs is the ultrafast formation of a plasma in the form of a cloud of liberated electrons escaping the surface. Because this moving cloud produces strong electric fields, an electron beam passing through this region can be significantly deflected.

Using this process, it was possible to measure the deflection angle of the electron beam passing through a 300 lines-per-inch copper mesh irradiated by a 800 nm pump. The observed behaviour is known to be fairly independent of the mesh size[127], and it has been

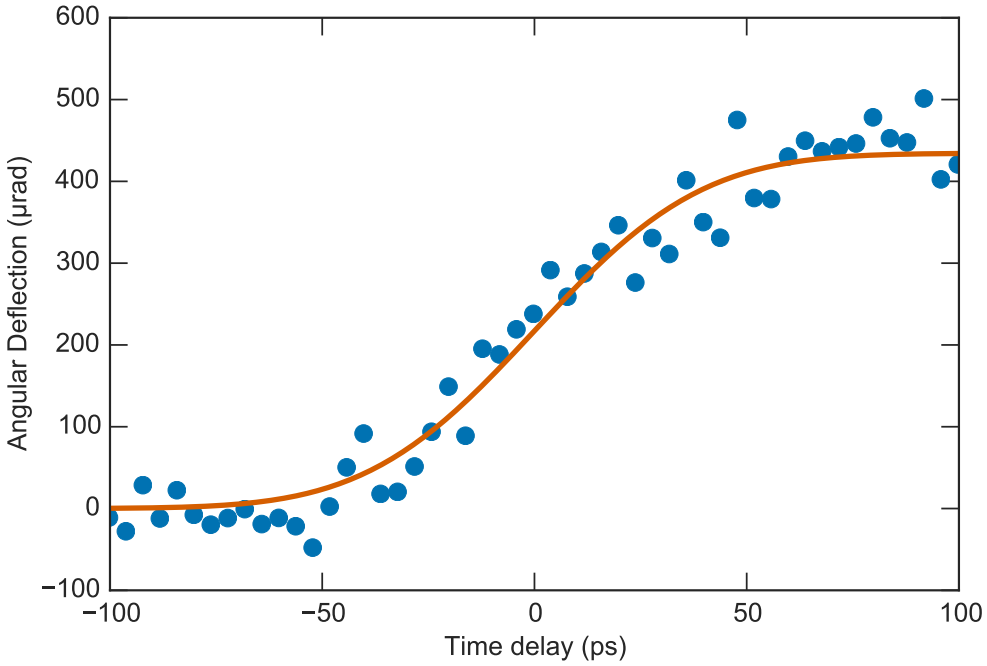


Figure 3.17.: *Method for finding the temporal overlap in an ultrafast electron diffraction experiment: observation of the transient deflection of the direct electron beam as a result of ultrafast plasma formation generated by irradiating a copper mesh with an intense femtosecond laser*

demonstrated[128] that multiphoton photoemission is more efficient at extracting charge from a metal surface than single-photon ionization using a UV pump. The results of this measurement, using a pump fluence of about 4 mJ/cm, are shown in Fig. 3.17. If the formation of the plasma was an instantaneous event and could be represented as a step function, then these dynamics could be modeled as a step function convoluted with a normal distribution whose width represents the pulse duration of the electron bunch. This results in the function

$$f(\tau) = \frac{A}{2}\,\mathrm{erfc}\left(\frac{\tau_0 - \tau}{\sqrt{2}\sigma}\right) \tag{3.25}$$

where $A$ is the amplitude of the step, $\sigma_t$ is the pulse duration, $\tau$ is the delay time between the pump and the probe, and $\tau_0$ is the location of the temporal overlap. This fit is overlaid on the data in Fig. 3.17, and was used to identify the location of the temporal overlap.

As a result of this fitting, a pulse duration of $\sigma_t \approx 30$ ps is recovered. This is significantly larger than the sub-picosecond value predicted by the ASTRA simulations in Section 3.4. However, it is well known that plasma formation is not instantaneous[129–132]; in fact, the rise time is on the order of a few tens of picoseconds, which is on the same order as what was observed in Fig. 3.17. Therefore, although the value of 30 ps could be taken as an upper limit for the electron pulse duration, it is thought that this value is heavily dominated by the time-scale of the plasma formation and not the pulse duration. Because the simulations

matched the transverse coherence length extremely well, the pulse duration of $\sim 500\,\mathrm{fs}$ from the simulations will be taken as the estimated pulse duration of the UED setup.

## 3.6. Outlook

The measured and simulated characteristics of the experimental system presented in this chapter suggest it possesses sub-picosecond resolution, while demonstrating the ability to produce TEM-quality diffraction patterns from atomically thin samples. These are the ingredients required to perform ultrafast electron diffraction of thin films and monolayers.

The machine could benefit from further characterization, in particular, from an experimental measurement of the pulse duration. However, since ASTRA is a well-vetted software, and its predictions were validated against the coherence length measurements, it is expected that the simulated pulse durations are likely close to the true pulse durations.

The next step is to demonstrate the functionality of this setup by performing UED experiments to study the dynamics of a transient phenomenon. This is precisely what is presented in the following chapter, which used UED to study transient electric fields from a laser-irradiated graphene surface.

# 4. Evolution of the Transient Electric Fields produced by the Photoionization of Graphene

*"With four parameters I can fit an elephant, and with five I can make him wiggle his trunk."*

— John von Neumann

## 4.1. Introduction

The development of the ultrafast structural probe presented in Chapter 3 provides a tool capable witnessing transient structural dynamics in the thinnest possible materials. This opens the door to innumerable prospective experiments, driven by the ability to produce new two-dimensional materials. Hopefully this potential will be fully realized in the near future. As a preliminary demonstration of the capability of this new system, this chapter will use ultrafast electron diffraction to study the production of Transient Electric Fields (TEFs) due to the irradiation of thin films.

It is well known that the illumination of a metal surface by an intense femtosecond laser results in complex and diverse physical processes[127,133,134]. One of the most prominent resulting effects is photoionization, which produces a plume of electrons propagating away from the surface. Associated with these liberated electrons is a strong electric field, whose transient dynamics are determined by the spatial and temporal evolution of the charge distribution of the plume. Photoionization is a ubiquitous phenomenon in physics, and contributes to various applications[135,136], fundamental processes[137,138], and experimental techniques[139–141]. From a fundamental point-of-view, ionization is an enticing combination of solid-state physics, electrodynamics, and photon-matter interactions. It is also an important process from an applied perspective, as it constitutes the first step in some photodetectors, and plays the lead role in certain physical techniques such as photoelectron spectroscopy. Furthermore, photoionization is significant for a more practical reason: because it is fairly straight-forward to implement from an experimental point-of-view (requiring only the focusing of a high-powered laser) it has been studied by many different techniques under many experimental conditions. This makes it a good "benchmark" experiment for new techniques such as low-energy ultrafast electron diffraction.

For these reasons, the photoionization of graphene was selected to be the first experiment

performed with the ultrafast electron diffraction system presented in Chapter 3. Graphene itself is an exciting topic of research, and its properties were introduced in Section 2.1. In relevance to photoionization, there is a recent effort to incorporate graphene into extremely sensitive photodetectors[142–145], and so it is important to have a thorough understanding of the underlying physics of the interaction between light and graphene. Additionally, in the last few years graphene has served as a substrate for biological samples in electron microscopy[7,146–148], and there is a similar effort to use graphene as a substrate in UED experiments. Because UED experiments are initialized by an intense femtosecond laser pulse, it is important to understanding the behaviour of graphene under such experimental conditions.

TEFs produced by the photoionization of various samples and substrates have been examined in several ultrafast electron diffraction experiments in the literature[129–132,149–151]. This chapter extends this line of research by adding graphene by the list of materials which have been studied. Although this experiment may shed light on the interaction between laser light and the electrons in graphene, its primary purpose is to demonstrate and validate the successful performance of the novel UED system presented in Chapter 3.

## 4.2. Experimental Details

The induced TEFs act as an electron lens, which transversely deflects the probe electron pulses. The graphene was tilted slightly relative to the axis of the chamber so that the TEFs were not parallel to the propagation direction of the probe electrons. In the following sections, the details of the experimental parameters will be presented.

### 4.2.1. Free-Standing Graphene

Single-layer graphene supported by a lacey carbon film on a 300 lines/inch copper TEM mesh was purchased from Ted Pella, Inc. and used as received. Bright-field TEM images of representative sample areas are shown in Fig. 4.1 A and B, measured in a Philips CM12 microscope operating at 80 kV ($\lambda = 0.0418$ Å). It was observed that the graphene was a single-crystal over large areas (hundreds of micrometers), as evident by the diffraction pattern shown in Fig. 4.1 C.

### 4.2.2. Sample Tilt

Knowledge of the sample tilt relative to the direction of the probe electrons beam is important to have a realistic estimation of the strength of the TEFs. Unfortunately, the intensities of the diffraction peaks of graphene hardly vary with the tilt angle[152], and so the traditional

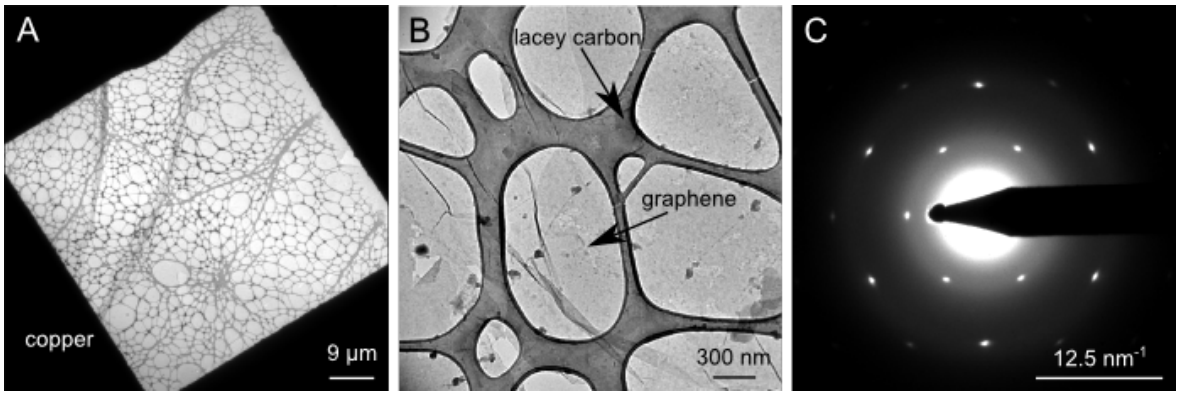


Figure 4.1.: *(A) Low-magnification and (B) high-magnification bright-field transmission electron microscope images of graphene supported by a lacey carbon film on a copper mesh. (C) Typical selected area electron diffraction pattern of graphene measured in a transmission electron microscope at* 80 kV.

method of using diffraction to measure the tilt is not possible. Instead, the angle was carefully measured using a protractor, leading to a value of approximately 10°.

### 4.2.3. Ultrafast Electron Diffraction

Time-resolved experiments were performed on the ultrafast electron diffraction setup described thoroughly in Chapter 3. Probe electrons with an energy of 6 keV were used to provide the best compromise between temporal resolution and sensitivity to the thin graphene films. Each diffraction pattern was accumulated for 0.5 s at a repetition rate of 1000 Hz, and each time-dependent measurement sequence was usually repeated 10 times and then averaged to improve the signal-to-noise ratio. Thus each diffraction pattern was typically collected with $\sim 10^7$ electrons.

### 4.2.4. Optical Excitation

Since the work function of graphene is 4.57 eV (ref. 153), it would be ideal to use pump light of 266.$\overline{6}$ nm (4.65 eV). However, it has been demonstrated that multiphoton ionization is much more efficient at extracting charge from thin films[127,128], and so it was decided to excite the sample with an 800 nm pump. The experiments were repeated with pump powers between 1 mW and 30 mW. Since the pump beam $1/e^2$ radius was measured to be $\sim 260$ µm (see Section 3.3.2), this corresponds to excitation fluences* of 1 – 30 mJ/cm$^2$.

* The fluence of a Gaussian beam with a $1/e^2$ radius of $w$ and pulse energy $E$ is $F = 2E/\pi w^2$ (ref. 116)

### 4.2.5. Measurement and Analysis Procedure

Prior to any measurement, both the spatial and temporal overlap were checked and adjusted if necessary, using the methods presented in Section 3.5.3. Care was taken to find a region of the sample that consisted of single-crystalline graphene (that is, not multiple domains). Once a suitable region was found, measurements were performed using the sequence described in Section 3.3.6. After background subtraction, each diffraction peak was identified and fit with a two-dimensional asymmetric Gaussian, allowing for the time dependence of the amplitude, position, and shape of each diffraction spot to be determined.

Because the electrons pass through a region containing TEFs after the sample, their trajectory is slightly deflected from what is predicted by the Bragg condition. The transient angular deflection, $\Delta\alpha(\tau)$, where $\tau$ is the time delay between the pump and the probe, can be used to estimate the strength and dynamics of the TEF generated by the emitted electrons from the ionization.

In the experiment, the transient deflection angle of the $(m, n)$ diffraction peak was calculated as

$$\Delta\alpha(\tau) = \tan^{-1}\left[\tan\theta_{m,n} + \frac{R(\tau)}{L}\right] - \theta_{m,n} \tag{4.1}$$

where $\theta_{m,n}$ is the Bragg angle and $R(\tau)$ is the transient displacement of the probe beam centroid relative to its initial position before laser irradiation, and $L$ is the camera length (the distance between the sample and the detector). This expression follows from the scattering geometry illustrated in Fig. 4.2. The camera length is carefully calibrated using a procedure outlined in the following section.

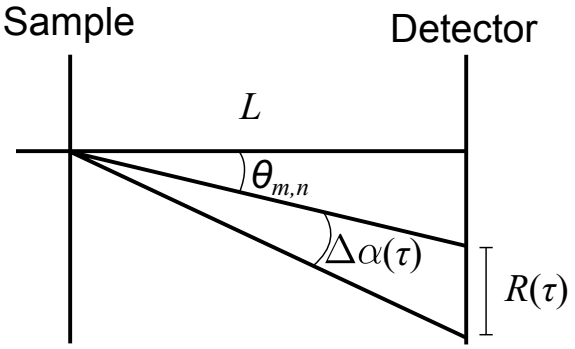


Figure 4.2.: *Illustration of the geometry used to relate the transient deflection angle $\Delta\alpha(\tau)$ to the experimentally measured displacement $R(\tau)$ of the $(m, n)$ diffraction order. The distance between the sample and the detector, $L$, is known as the camera length.*

The scattering angles are given by Bragg's law, which can be expressed as[95]

$$\theta_{m,n} = 2\sin^{-1}\left(\frac{\lambda|\mathbf{G}_{m,n}|}{2}\right) \tag{4.2}$$

where $\lambda$ is the probe electron's wavelength, and $|\mathbf{G}_{m,n}|$ is the magnitude of the reciprocal lattice vector for the $(m,n)$ plane. From the lattice structure of graphene, it can be found that[154]

$$|\mathbf{G}_{m,n}| = \frac{4\pi}{2l}\sqrt{m^2 - mn + n^2} \tag{4.3}$$

where $l = 1.42\,\text{Å}$ is the carbon-carbon bond length[154].

## 4.3. Camera Length Calibration

The camera length, $L$, is defined as the distance from the sample to the projected image of the diffraction pattern. In a lensless system, such as the one described in Chapter 3, this corresponds to the true physical distance between the sample and the detector. Although its value can be measured as the mechanical distance between the sample holder and the front MCP plate, a more accurate measurement is required to enable proper assignment of scattering angles in the measured diffraction patterns. This can be done by using a sample with a well-known structure as a reference; such a sample should satisfy the following requirements[155]:

1. many well-defined diffraction spots
2. chemically stable under electron irradiation (no structural changes)
3. structural parameters accurately measured by independent techniques

With these properties in mind, aluminum was chosen as the reference due to its structural robustness, strong scattering, and the fact that the its unit cell parameter $a$ is very thoroughly established[156]. Thus calibration of the camera length is enabled by deriving a relationship between the camera length and the unit cell parameter. To do this, it is noted that electrons scattered through an angle $\theta_{hkl}$ from the $(h,k,l)$ diffracting plane in graphene satisfy Bragg's law[94]:

$$\lambda = 2d_{hkl}\sin\theta_{hkl} \tag{4.4}$$

where $\lambda$ is the electron's wavelength, and $d_{hkl}$ is the spacing between the $(h,k,l)$ planes. Aluminum is well known to form a face-centered cubic (FCC) lattice[156], and so the lattice spacing has the simple expression

$$d_{hkl} = \frac{a}{\sqrt{h^2 + k^2 + l^2}} \tag{4.5}$$

where $a$ is the unit cell parameter. If this is substituted back into Bragg's law, Eq.(4.4), the scattering angle can be expressed as

$$\theta_{hkl} = \sin^{-1}\left(\frac{\lambda}{2d_{hkl}}\right) = \sin^{-1}\left(\frac{\lambda\sqrt{h^2 + k^2 + l^2}}{2a}\right) \tag{4.6}$$

To relate this to the camera length, the geometry of the scattering experiment illustrated in Fig. 4.3 shows that the scattering angle can be determined from the measured radius of the spots in the diffraction pattern from the relation $\tan(2\theta_{hkl}) = R_{hkl}/L$. This then leads to the final expression for the camera length in relation to the unit cell parameter of aluminum:

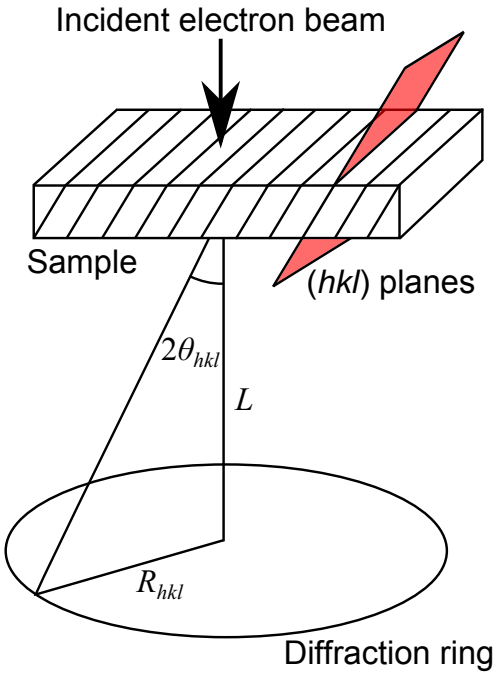


Figure 4.3.: *The geometry of the diffraction mode of a transmission electron microscope showing the relationship between the camera length $L$ and the scattering angle $\theta_{hkl}$ and diffraction ring radius $R_{hkl}$ of the $(hkl)$ reflecting plane.*

$$L = \frac{R_{hkl}}{\tan\left[2\sin^{-1}\left(\frac{\lambda\sqrt{h^2+k^2+l^2}}{2a}\right)\right]} \tag{4.7}$$

Fig. 4.4 shows an example of a typical ultrafast diffraction pattern from 15 nm thick polycrystalline aluminum used to calibrate the camera length of the UED system. The sample was prepared using thermal evaporation deposition, resulting in a polycrystalline sample. Diffraction patterns were recorded at several electron energies, and for each image, the first few diffraction peaks were used to provide some statistics. The peaks were indexed by sorting

the peaks locations in ascending order by radius and matching them with the lowest order allowed Bragg reflections. For aluminum (and other FCC crystals), allowed reflections are whenever $(h, k, l)$ are either all odd or all even, as listed in Table 4.1.

Table 4.1.: *Reflections allowed by the face-centered cubic symmetry of aluminum*

| $(h, k, l)$ | $\sqrt{h^2 + k^2 + l^2}$ |
|---|---|
| (1, 1, 1) | 1.73 |
| (2, 0, 0) | 2.00 |
| (2, 2, 0) | 2.83 |
| (3, 1, 1) | 3.32 |
| (2, 2, 2) | 3.46 |
| (4, 0, 0) | 4.00 |
| (3, 3, 1) | 4.36 |
| (4, 2, 0) | 4.47 |
| (4, 2, 2) | 4.90 |
| (3, 3, 3) | 5.20 |
| (4, 4, 2) | 6.00 |
| (5, 3, 3) | 6.56 |
| ⋮ | ⋮ |

Using the accepted value of $a = 404.95\,\text{pm}$ for aluminum[156], Eq.(4.7) was then used to calculate the camera length for each reflection and electron energy, as shown in Fig. 4.4. These values were averaged to give the calibrated camera length as $L = 53.04 \pm 6.25\,\text{mm}$.

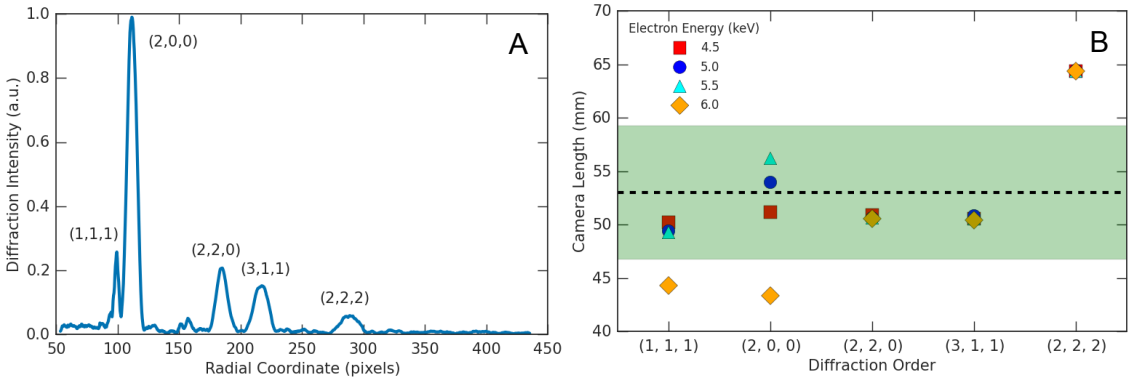


Figure 4.4.: *(A) Radial diffraction pattern of* 15 nm *thick polycrystalline aluminum measured with ultrafast,* 6 keV *electrons, with the peaks used for the camera length calibration identified and indexed. (B) Camera length calculated for each peak identified in (A) for several electron energies, with the average value and standard deviation shown by the dashed line and the shaded region, respectively.*

## 4.4. Model of the Transient Electric Fields Produced by Ultrafast Ionization

This section will introduce a simple model to describe the interaction between the probe electrons and the electric field generated by the negative charge cloud and positive surface charges resulting from the ultrafast ionization of the graphene and the substrate. In this model, the coordinate frame will be aligned so that the probe electrons are traveling along the $z$-axis with an initial velocity of $\mathbf{v}_0 = (0, 0, v_0)$. To account for the tilt between the sample and the probe electron beam, an angle $\gamma$ is introduced between the sample normal vector $\hat{\mathbf{n}}$ and the $z$-axis (see Fig. 4.5 for a schematic illustration of the model presented in this section). The plane containing $\hat{\mathbf{n}}$ and the $z$-axis is used to define the $x$-axis, so that the normal vector is $\hat{\mathbf{n}} = (\sin\gamma, 0, \cos\gamma)$.

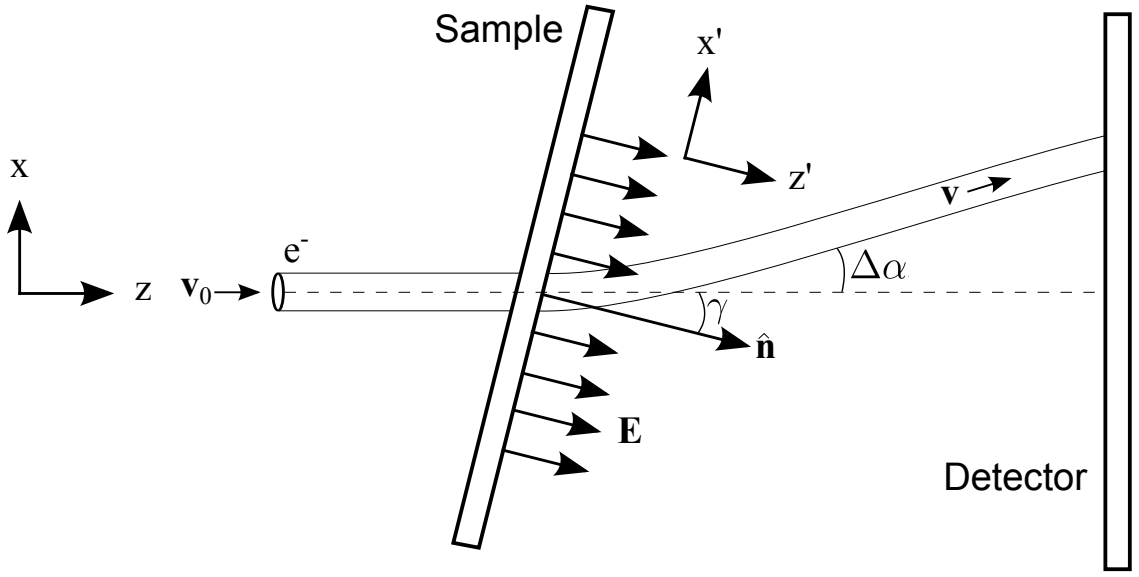


Figure 4.5.: *Illustration of the coordinate system used to model the deflection of the electron beam through a transient electric field*

Due to the symmetry of the optical excitation, the components of the electric field transverse to the sample's normal vanish (in reality there is a little asymmetry which arises from the incidence angle of the pump laser and the inhomogeneity in the excitation profile, but these effects are neglected in this simple model). As such, the electric field is parallel to $\hat{\mathbf{n}}$. This makes it convenient to introduce a coordinate frame relative to the sample, where the $z$-axis is along $\hat{\mathbf{n}}$ (see Fig. 4.5). This frame will be denoted by the primed coordinates $\mathbf{x}'$, and the electric field in this frame is given by $(0, 0, E_n(\mathbf{x}'; t))$. In the system's (unprimed) coordinate frame, this corresponds to a TEF of:

$$\mathbf{E}(\mathbf{x}; t) = \begin{pmatrix} \cos\gamma & 0 & \sin\gamma \\ 0 & 1 & 0 \\ -\sin\gamma & 0 & \cos\gamma \end{pmatrix} \begin{pmatrix} 0 \\ 0 \\ E_n(\mathbf{x}; t) \end{pmatrix} = \begin{pmatrix} E_n(\mathbf{x}; t)\sin\gamma \\ 0 \\ E_n(\mathbf{x}; t)\cos\gamma \end{pmatrix} \tag{4.8}$$

Because the temporal evolution is triggered by the arrival of the pump pulse, the TEF only exists for positive times and so $E_n(\mathbf{x}';t) = 0$ for $t < 0$.

The velocity of a probe electron propagating through this field in the post-sample region obeys

$$\frac{\mathrm{d}\mathbf{v}(t;\tau)}{\mathrm{d}t} = \frac{q}{m}\mathbf{E}(\mathbf{x};t-\tau) \tag{4.9}$$

where $m = m_e/\sqrt{1-v_0^2/c^2}$ is the electron's relativistic mass and $\tau$ is the temporal delay between the arrivals of the probe electrons and the pump laser. The final velocity $\mathbf{v}(t_0;\tau)$ of the electron (outside of the region of the electric field) can be used to calculate the transient deflection angle at a delay time $\tau$, since

$$\Delta\alpha(\tau) = \tan^{-1}\left[\frac{v_x(t_0;\tau)-v_x(0)}{v_0}\right] \approx \frac{v_x(t_0;\tau)-v_x(0)}{v_0} \tag{4.10}$$

In this expression, $t_0$ is interaction time between the probe electrons and the electric field (that is, the propagation time of the probe electrons from the sample to the detector). To find this final velocity, Eq.(4.9) can be integrated to give the solution

$$\mathbf{v}(t_0;\tau) = \mathbf{v}(0) + \frac{q}{m}\int_0^{t_0}\mathbf{E}(\mathbf{x};\xi-\tau)\,\mathrm{d}\xi \tag{4.11}$$

The initial condition $\mathbf{v}(0) = \mathbf{v}(0;\tau)$ specifies the initial velocity of the electrons in the post-sample region, accounting for the diffraction angles. For example, the unscattered electrons ($0^{\text{th}}$ order diffraction) have $\mathbf{v}(0) = \mathbf{v}_0$. For an $(m,n)$ order diffracted electron, taken to be scattered along the $x$-axis for simplicity, then $\mathbf{v}(0) = (v_0\sin\theta_{m,n}, 0, v_0\cos\theta_{m,n})$.

To fit experimental data to Eq.(4.10), one would need an explicit model of the TEF, $\mathbf{E}(\mathbf{x};t)$. Various such models have been proposed in the literature[129–132,149–151], with differing degrees of complexity. Perhaps the most sophisticated model, the so-called "three-layer model" (ref. 132), involves 7 fitting parameters, representing variables such as the speed of the emitted electron cloud, the total charge of emitted electrons, and the fraction of the electrons that fall back to the sample due to the positive mirror charges at the surface of the sample. Although this model might offer the most physically realistic description of the photoionization dynamics, it contains so many parameters that it is difficult to trust and interpret the results of fitting it to one-dimensional data.

With this in mind, this chapter will instead make a simplifying approximation to provide an estimation of the strength of the TEF. This approach has been adopted in several past studies[129,131,149–151], and has been found to be highly successful. The approximation is motivated by two facts:

1. At 6 kV, the probe electrons travel at $v_0 = 4.6 \times 10^7\,\mathrm{m/s}$ along the $z$-axis, whereas the electron cloud responsible for the TEFs leaves the graphene surface at about $10^6\,\mathrm{m/s}$ (ref. 129, 132). This order of magnitude difference in speed suggests that the TEFs hardly change during the interaction time, so that the probe effectively sees a "snapshot" of the TEF at a specific delay time.

2. The measured deflection angles are extremely small ($\ll 1\,\mathrm{rad}$), implying that the probe electrons hardly deviate from their unperturbed trajectory. Because the probe electrons are essentially parallel to the $z$-axis (since the diffraction angles are small), this means that they hardly experience the spatial distribution of the TEF. Instead, they see a fairly constant field along $z$ at their transverse location.

These statements suggest the following approximation of replacing the transient field with its temporal and spatial average at each time delay:

$$\begin{aligned}
\mathbf{E}(\mathbf{x}; t-\tau) &\approx \iint \left[\frac{1}{t_0}\int_0^{t_0} \mathbf{E}(x_0, y, z; t-\tau)\,\mathrm{d}t\right] \mathrm{d}y\,\mathrm{d}z && \text{(4.12a)}\\
&\equiv \langle \mathbf{E}\rangle_{x_0,t_0}(\tau) && \text{(4.12b)}\\
&= \langle E_n\rangle_{x_0,t_0}(\tau) \begin{pmatrix}\sin\gamma\\ 0\\ \cos\gamma\end{pmatrix} && \text{(4.12c)}
\end{aligned}$$

where the notation $\langle \mathbf{E}\rangle_{x_0,t_0}(\tau)$ for the spatial and temporal average of the electric field at time delay $\tau$ and transverse coordinate $x_0$ has been introduced. With this approximation, the transverse velocity of the probe electrons is

$$\begin{aligned}
v_x(t_0;\tau) &= v_x(0) + \int_0^{t_0} E_n(\mathbf{x}; \xi-\tau)\sin(\gamma)\,\mathrm{d}\xi && \text{(4.13a)}\\
&\approx v_x(0) + \frac{q}{m}\langle E_n\rangle_{x_0,t_0}(\tau)\sin(\gamma)\int_0^{t_0}\mathrm{d}\xi && \text{(4.13b)}\\
&= v_x(0) + \frac{q}{m}\langle E_n\rangle_{x_0,t_0}(\tau)\sin(\gamma)\,t_0 && \text{(4.13c)}
\end{aligned}$$

which leads to a final deflection angle of

$$\Delta\alpha(\tau) \approx \frac{q\sin(\gamma)\,t_0}{m v_0}\langle E_n\rangle_{x_0,t_0}(\tau) \qquad (4.14)$$

Thus the measured deflection angle is proportional to the strength of the average TEF.

## 4.5. Experimental Results

The results of the UED experiments of photoionized free-standing graphene are shown in Fig. 4.6 A, which shows the difference in the diffraction patterns with an 800 nm pump and without any pump. It is evident that all the diffraction peaks are deflected along the same axis; this allows for the transient displacement of all peaks of the same order to be averaged, resulting in the traces shown in Fig. 4.6 B. It is evident that the lower order diffraction peaks are deflected more than higher order peaks, with the $0^{\text{th}}$ order (unscattered) electrons exhibiting the largest amount of deflection.

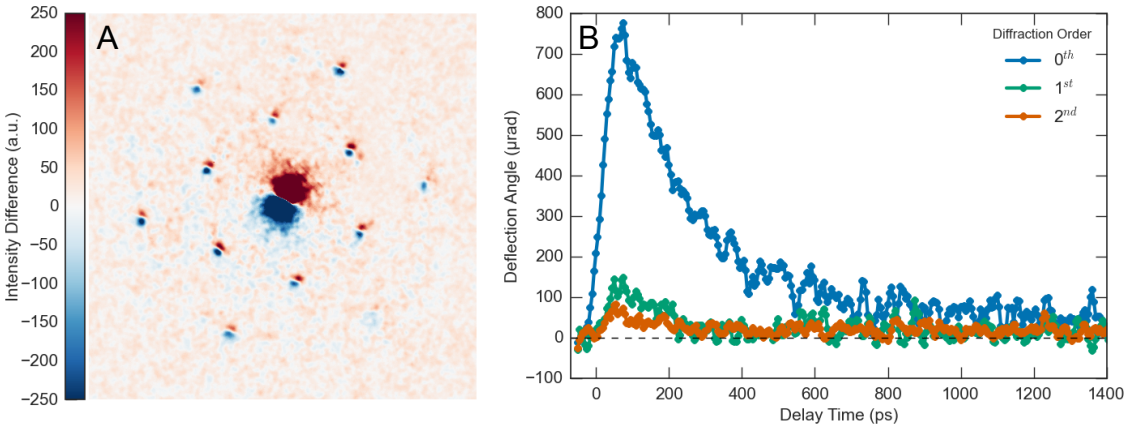


FIGURE 4.6.: *(A) Deflection angles of several diffraction orders for electrons passing through a transient electric field from graphene. The graphene was excited with an* 800 nm *pump and a fluence of about* 22 mJ/cm$^2$. *(B) Difference diffraction image at an* 80 ps *time delay*

The order-dependence of the transient deflections can be interpreted in terms of the simple model outlined in Section 4.4. The culminating equation, Eq.(4.14), states that the deflection angle is proportional to the average TEF, i.e. $\Delta\alpha(\tau) \propto \langle E_n \rangle_{x_0,t_0}(\tau)$. The field is averaged over two parameters: the interaction time $t_0$ and the transverse location of the scattered beam $x_0$ (refer to Fig. 4.7 A). Because the diffracted beams travel at an angle, they sample the field at different transverse locations. For instance, the $(m, n)$ diffraction beam passes through the shaded region shown in Fig. 4.7 A, and so experiences a different field than, for instance, the undiffraction beam. Very roughly, the $(m, n)$ diffraction order approximately samples the TEF at the transverse location

$$x_{m,n} = \frac{1}{2} z_0 \tan \theta_{m,n} \tag{4.15}$$

In this expression, $z_0$ is the distance between the electron cloud and the sample surface (Fig. 4.7 A). Using the fact that the electron cloud propagates with a speed on the order of 1 µm/ps (ref. 129, 132) and the TEF reaches its maximum around 100 ps, the distance at the peak is about $z_0 \approx 100$ µm.

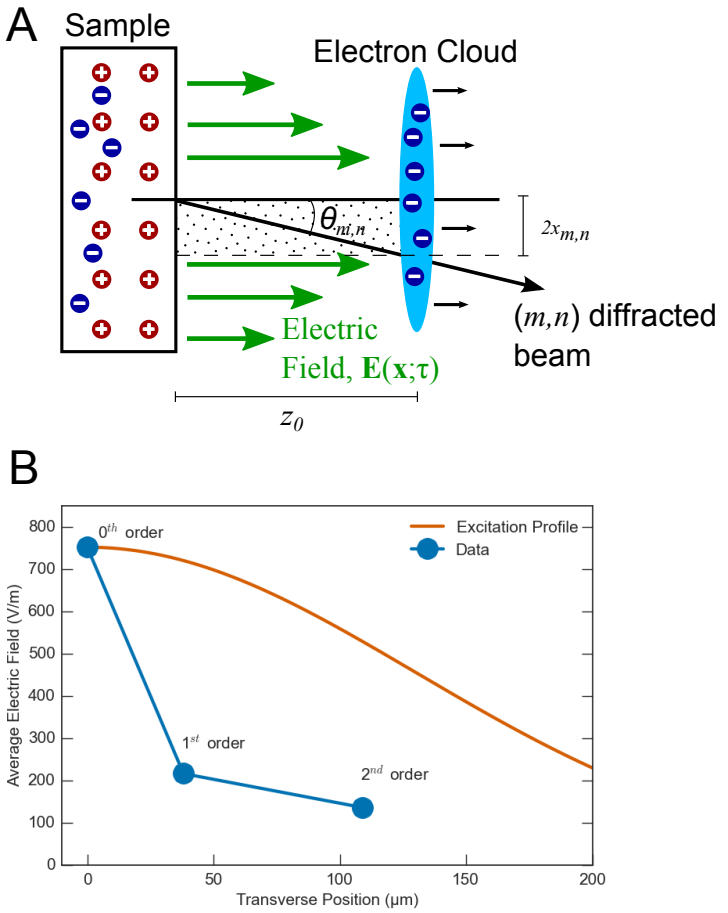


Figure 4.7.: *(A) Illustration of how different diffraction orders sample the spatial dependence of the transient electric field. In the drawing in the* $(m, n)$ *diffraction order experiences the average electric field in the shaded region. (B) The peak average electric field felt by several diffraction orders. Overlaid is excitation profile of the* 800 nm *pump laser.*

Using the transient deflection data shown in Fig. 4.6 the maximum average electric field $\langle E_n \rangle_{x_{m,n},t_0}$ was calculated and is plotted in Fig. 4.7 B. A significant spatial variation in the TEF is observed, with the strength of the field decreasing further away from central axis. Overlaid on this plot is the excitation profile of the 800 nm pump laser. Evidently, the electric field falls off significantly faster than the excitation, and has a width of around 50 µm compared with the 260 µm width of the pump.

Initially, it is expected that the spatial distribution of the TEF matches the pump's profile, since the number of ejected electrons is proportional to the number of photons. Since Fig. 4.7 B occurs about 100 ps after the arrival of the pump, the data implies that the TEF becomes more narrow as time progresses. This can be explained by two phenomena: the contraction of the positive surface charges due to neutralization and degradation of mirror-charge effects, and the expansion of the emitted electron cloud due to space-charge broadening. The combined result of these two effects is that the TEF becomes more and more narrowly

concentrated in the middle of the excitation profile.

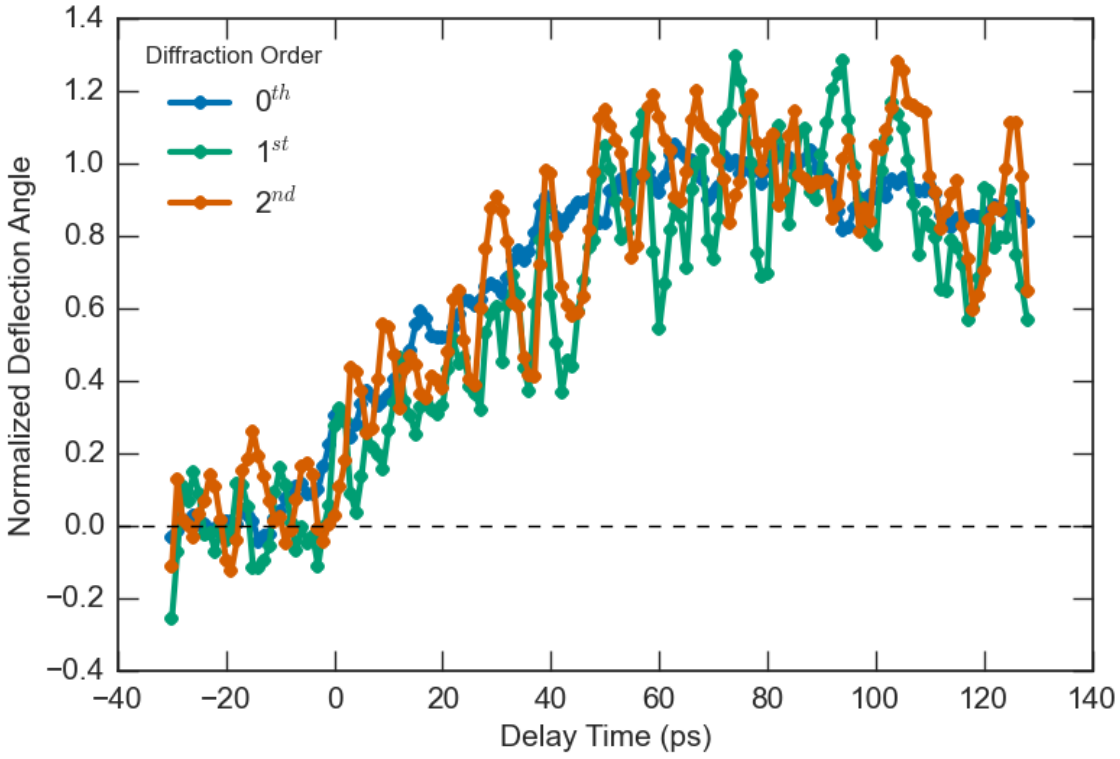


Figure 4.8.: *Transient deflection angles of several diffraction orders, normalized to the maximum angle.*

The trajectories were normalized to the peak deflection angle, resulting in the traces shown in Fig. 4.8. It is evident that, within the limits of experimental error, the different diffraction orders show identical transient behaviour. This indicates that the TEF has a spatially-independent time-dependence. This has similarly been identified in other samples, such as thin films of aluminum[150].

The peak amplitude of the TEF (i.e. the maximum field felt by the $0^{\text{th}}$ order peak) is around 750 V/m. This is significantly lower that what has been observed in other samples with a similar excitation fluence (see, for instance, ref. 129–132, 149, 150). This is likely due to the comparatively low absorbance of graphene, which is roughly 2.3 % at 800 nm (ref. 157). When this is taken into account, the TEF strength is the same order of magnitude as what has been reported, for instance, for silicon[129]. This implies that the physics of photoionization of graphene is similar to that of other thin film. Alternatively, the difference in the peak field strength might suggest that the approximate analysis represented by Eq.(4.14) does not provide an adequate model of the effects of the TEF. Although it is beyond the scope of this chapter, which only serves to demonstrate the capability of the UED setup of Chapter 3, further experimentation is required to clarify these points.

## 4.6. Closing Remarks

In summary, the preliminary experiment presented here tracked the positions of the diffraction peaks from graphene, which were deflected due to the production of transient electric fields. A very simple and approximate analysis was developed to relate the magnitude of the transient deflection angles to the strength and spatial distributions of the TEFs.

Although these results serve the purpose of verifying the potential of UED for studying thin films, it is possible that more information could be extracted from the experimental data presented here. For instance, it might be enlightening to try fitting the data with the aforementioned "three-layer model" (ref. 132) to see if it complements the simple analysis presented here. However, such a sophisticated analysis might require further experimentation than what is appropriate for the verification of UED setup of Chapter 3.

Although brief, this chapter demonstrated the capability of low-energy UED to measure time-dependent changes in thin films. However, TEFs constitute a reversible reaction; that is, the system returns to its initial state after the dynamics are over. Unfortunately, the stroboscopic procedure of the low-energy UED machine is ill-suited for studying irreversible reactions. The following chapter is devoted to solving this problem, and enables UED to have access to both reversible and irreversible reactions in thin films.

# 5. The Physics of Transient Diffraction with Ultrafast Streak Cameras

*"If a picture is worth a thousand words, then a video is worth a million."*
— Troy Olson and Jeff Loquist

## 5.1. Introduction

Most of the processes studied to date with UED have had a key experimental detail in common: they involved reversible reactions. For example, in the experiment presented in Chapter 4, the plasma formed by ultrafast ionization was short-lived and caused minimal lasting damage to the underlying graphene. This allowed the same area of graphene to be repeatedly pumped and probed. However, the reduction of graphene oxide presented in Chapter 2 would be classified as irreversible since it could not be undone: the newly formed graphene (rGO) was a new species, with no hope of re-oxidation.

Reversible reactions form a small subset of the chemical reactions of interest. In fact, most of the reactions that occur in chemistry and biology are irreversible. This proves to be a hindering step when attempting to bring the spatial and temporal resolution offered by a technique such as UED to such fields. The challenge lies in the fact that, in the pump-probe paradigm, the sample must be moved between each pump shot so that the reaction has a fresh starting point. This not only limits the repetition rate of the experiment (which would be determined by the time required to translate the sample), but also requires extremely large homogeneous sample areas, which might not be possible for all types of materials. Graphene oxide is a perfect example of this; while the global structure can be described by an average oxidation level, the local structure can vary quite dramatically in terms of oxygen content from one spot to the next[158].

Ultrafast streaking is a technique that bypasses these hurdles by offering the unprecedented opportunity to record an entire time-dependent diffraction pattern with a single probe pulse. This is extremely appealing for irreversible reactions, as even if the sample is completely destroyed by the reaction, a full time series has already been recorded. The measurement may be repeated with new starting sample positions to improve signal-to-noise by averaging, but new machines are coming online[159–163] capable of true single-shot measurements. Ultrafast streaking is an established technique in time-resolved x-ray diffraction[164–167], and has recently been applied to ultrafast electron diffraction[168,169]. Modern advances in x-ray[170–176] and electron[177–180] streak cameras have reported temporal resolution in the femtosecond regime,

making streaking an attractive alternative to the traditional stroboscopic method of time-resolved diffraction.

Ultrafast streaking works by the following principle: the probe pulse (be it x-rays or electrons) is stretched to the order of a few picoseconds, and the resulting diffraction pattern from a pumped sample is detected with an ultrafast streak camera. The long probe pulse captures the transient dynamics of the sample as it diffracts, and the streak camera uses a rapidly oscillating electric field to map the temporal coordinate of the diffraction pattern to a spatial one on the detector. (In the case of an x-ray probe, a photocathode is used to convert the x-rays to electrons prior to the streak camera.) The resulting streaked diffraction pattern then contains the temporal dynamics along one of its spatial dimensions. An illustration of a typical setup is shown in Fig. 5.1

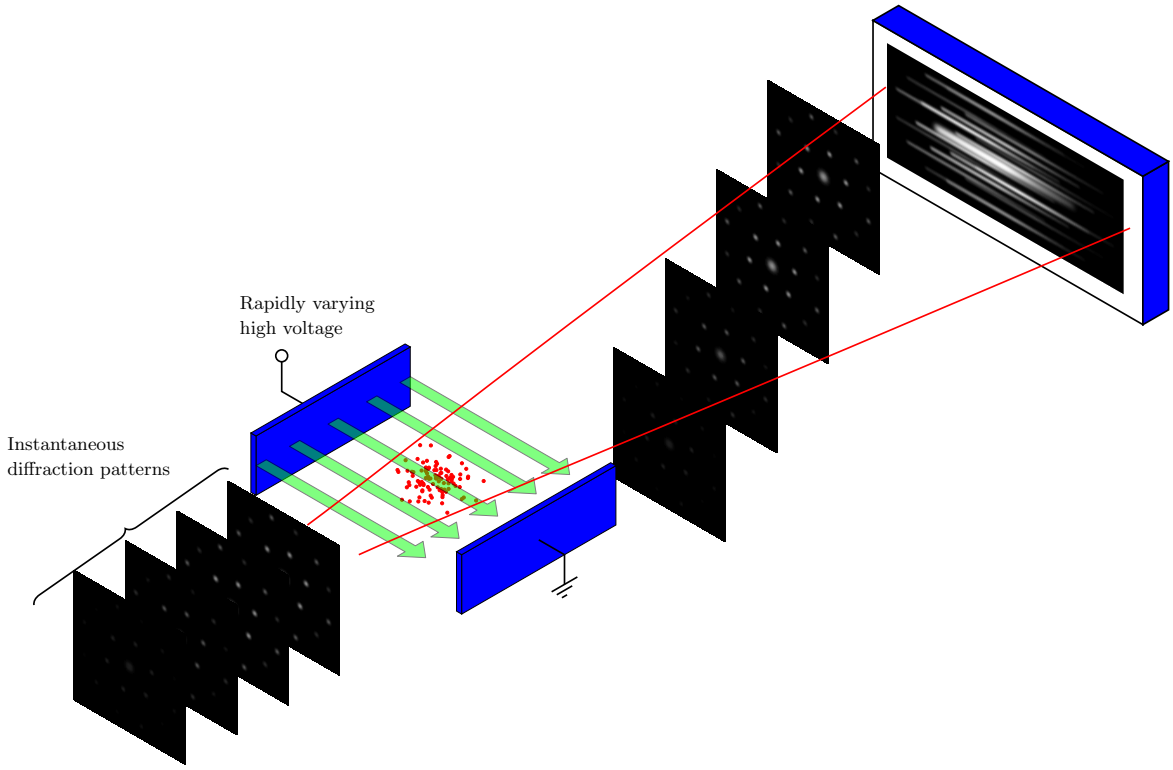


Figure 5.1.: *An illustration of the general principles behind ultrafast streaking of transient diffraction patterns. The probe pulse records the time-dependent diffraction as it propagates, and a streak camera after the sample maps this temporal coordinate to a spatial one on the camera.*

While this technique has many challenges, one of the hindering restrictions is the lack of a rig-

orous, quantitative analysis of the streaked diffraction patterns. All previous studies[164–167,169] have adopted the same approach: for each streaked diffraction spot, the image is averaged over the transverse coordinate to the streaking direction to obtain a one-dimensional trajectory of intensity along the streaking direction. While this is the most straight-forward approach, it obviously constitutes a loss of information; instead of a two-dimensional diffraction image at each time point, all that is left is one-dimensional data. A slight improvement was made by segmenting the streaked diffraction pattern into boxes along the streaking direction and then fitting to obtain the characteristics of each box[168]. However, both these methods suffer from the same fundamental flaw; they subtly assume that the intensity along the streak of a diffraction spot is equal to the time-dependent intensity of that spot. This can lead to significantly erroneous results when used to analyze even the simplest of dynamics.

In this chapter, this problem will be addressed by the development of a general theory of streaking of time-dependent diffraction patterns. The presented analysis technique provides a way to recover the two-dimensional diffraction image at each time point from the streaked image alone. In addition, it is demonstrated the proposed approach works on diffraction peaks that overlap when streaked, which not only removed the necessity of carefully choosing the streaking direction, but also extends the streaking technique to study polycrystalline samples and materials with complex crystalline structures.

## 5.2. General Streaking Theory

As stated above, the goal of this chapter is to outline a method to recover the time-dependent diffraction pattern $u(x, y; t)$ from a streaked image $s(x, y)$. Here, $x$ and $y$ are the detector coordinates and $t$ is the time-dependence due to the sample dynamics. The relationship between $s$ and $u$ can be arrived at by considering what the streaking process actually entails. Probe electrons (or electrons produced from probe x-rays) are given a transverse momentum kick so that electrons arriving at the sample at different times are deflected to different spatial locations on the detector. This causes the diffraction pattern to be "smeared" along the streaking direction. The streaked diffraction pattern can thus be pictured as being formed by overlapping the instantaneous diffraction patterns during the dynamics recorded by each temporal slice of the electron pulse. Mathematically, this means that for each time $t$, the instantaneous diffraction pattern $u(x, y; t)$ is shifted spatially by the appropriate displacement $v_s t$, where $v_s$ is known as the streaking velocity or the sweep speed*. Of course, some parts of the electron pulse will contain more electrons than others, and so each instantaneous diffraction pattern must be weighted by the appropriate temporal electron density $\rho(t)$. The contribution from each temporal slice is then integrated at the detector, resulting in the streaked diffraction pattern

* It has been implicitly assumed that the streak camera works in a linear regime where the spatial position on the detector is related to the temporal coordinate in the pulse by $x = v_s t$. Nonlinearities in this expression resulting from, for instance, poor alignment and space-charge effects, are negligible in most experiments[181].

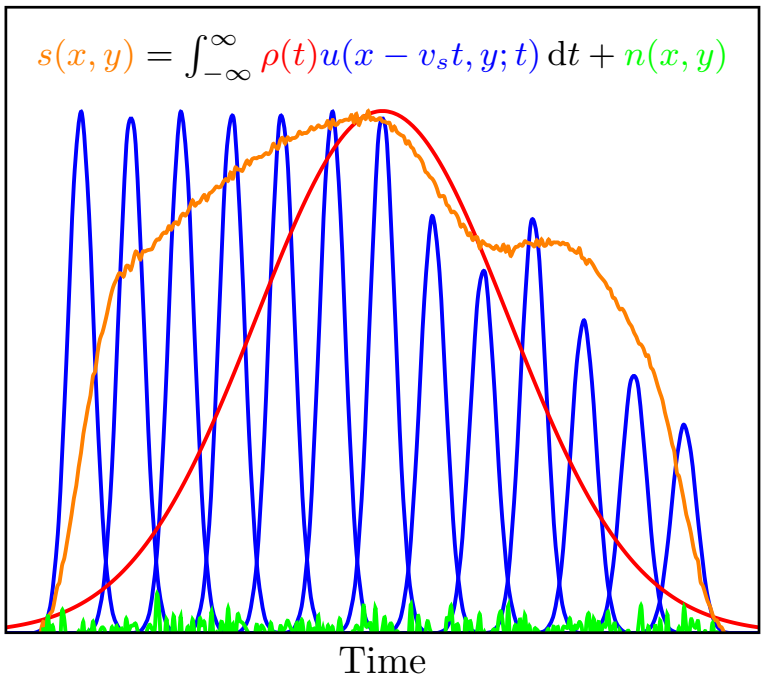


Figure 5.2.: *Illustration of the contributing terms to the equation governing the streaking of time-dependent diffraction*

$$s(x,y) = \int_{-\infty}^{\infty} \rho(t)u(x - v_s t, y; t)\,\mathrm{d}t \tag{5.1}$$

The incorporation of noise into this equation will be left until Section 5.2.2. The way the various terms contribute to this equation is illustrated in Fig. 5.2. The $x$ and $y$ axes are arbitrary, but for convenience the $x$ axis has been defined along the streaking direction. In practice it is preferable for this direction be chosen to avoid the collision of the trajectories of various diffraction orders (choosing the streaking direction is not an issue in the case of polycrystalline samples). This point will be discussed in further detail in Section 5.5.

The first term on the right-hand side of Eq.(5.1) is sometimes known as *spatially-varying convolution*, due to its formal similarity to the conventional convolution operator. In fact, if the diffraction pattern is not changing (i.e. $u(x,y;t) = u_{\mathrm{static}}(x,y)$), then $s = \rho * u_{\mathrm{static}}$, where $*$ denotes the convolution operator. This simple relationship can be used to recover $\rho(t)$ in a separate experiment by streaking the direct probe beam or a static (un-pumped) diffraction pattern[178]. In the case where dynamics are present, by measuring a single streaked diffraction pattern $s(x,y)$ and with prior knowledge of the electron density $\rho(t)$, it will be shown in the following sections that it is possible to recover the time-dependent diffraction pattern $u(x,y;t)$ by "spatially-varying deconvolution".

### 5.2.1. Discretization

Before presenting the deconvolution algorithm, attention should be drawn to the fact that although each image has been presented as a continuous function, this is not the case in a real experiment due to the discrete nature of the detector (e.g. camera sensor). The discrete version of Eq.(5.1) is

$$s_{i,j} = \sum_{k=0}^{L-1} \rho_k u_{i,j-k,k} \tag{5.2}$$

where $L$ is the length of the vector $\boldsymbol{\rho}$ representing the electron pulse profile. The temporally evolving diffraction pattern takes the form of a stack of images with elements $u_{i,j,k}$. The discretization of the time coordinate of $\boldsymbol{u}$ occurs by sampling $u(\cdot,\cdot;t)$ at the pixel locations along the $x$-axis due to the streaking. This linear model is represented in Fig. 5.3, which also accounts for the additive noise that will be discussed in the following section.

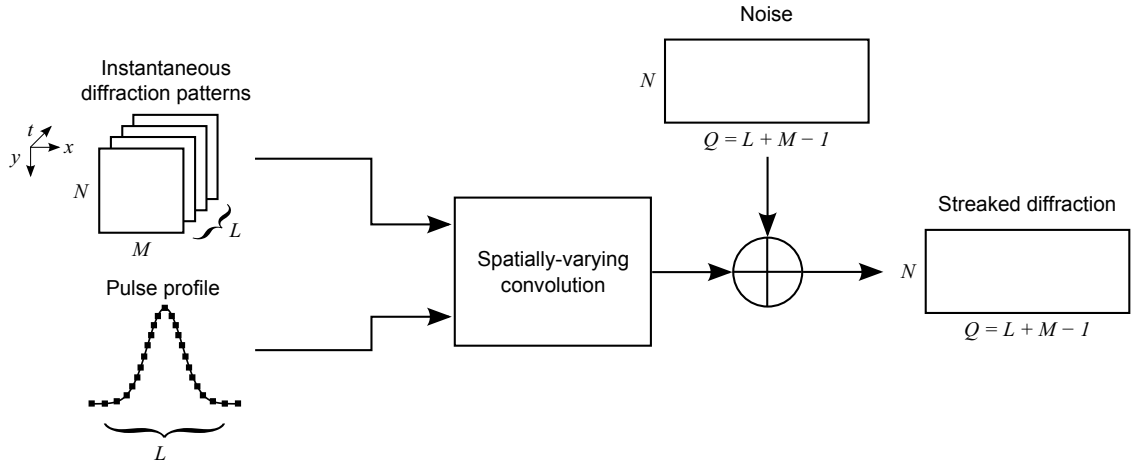


FIGURE 5.3.: *Block schematic of the linear space-variant image degradation model, with the image dimensions shown*

The pertinent image dimensions are:

- $\boldsymbol{\rho} \in \mathbb{R}^{L\times 1}$
- $\boldsymbol{u} \in \mathbb{R}^{N\times M\times L}$
- $\boldsymbol{s} \in \mathbb{R}^{N\times Q}$, where $Q = L+M-1$ (note that the full convolution needs to be considered)

In writing Eq.(5.2) it has been implicitly assumed the streaking direction (specified by the $x$ axis) lies along on a detector pixel axis. This is, however, difficult to achieve in practice, and so all images must be re-sampled on the grid defined by the streaking axis.

Also, because the streaking is solely along the $x$-axis, the spatially-varying convolution along each row of the streaked image can be considered independently. That is, Eq.(5.2) can be written as $N$ independent equations of the form

$$s_j = \sum_{k=0}^{L-1} \rho_k u_{j-k,k} \tag{5.3}$$

Given this information, there are two ways to proceed: the first and most obvious approach would be to loop over the $i$ index and apply spatially-varying deconvolution to solve for $u_{j,k}$ on each pixel row using Eq.(5.3). Alternatively, the images could be stacked lexicographically (row-wise) and the spatially-varying deconvolution algorithm would only need to be performed once. The former was chosen because it dramatically decreases the memory requirements of the algorithm, as well as enabling multi-threaded or parallel implementations. For the remainder of this chapter, the $i$ (or $y$) dependence will be dropped and all equations and quantities will refer to a single pixel row.

The fact that each pixel row in the streaked image can be considered separately is an important results since it opens up the streaked diffraction technique to the class of materials that produce diffraction patterns which contain rings, such as polycrystalline or amorphous samples. This is a category of materials that has been thought to be inaccessible to the streaking technique, and so has gone unexplored in the past. Although this point will not be explored further in this chapter, the results on the overlapping spots presented in Section 5.5 corroborate this claim.

The computation of Eq.(5.3) is quite computationally demanding; if $u$ were constant in time, then the right-hand side is simply a regular convolution, and could be computed in $O(w \log_2 w)$, where $w = \max(M, L)$. Unfortunately, the spatially-varying nature of the convolution due to the temporal evolution of the diffraction pattern requires straight-forward arithmetic operations, and so occurs in $O(ML)$*. Although this computation might be feasible, it is extremely intensive (since the product $ML$ is large), and so a simplifying approximation known as the "spatially-varying overlap-add method" will be used[182]. To motivate this approximation, the time-dependent diffraction pattern will be re-written in the familiar "overlap-add" framework that is commonly used in the computation of discrete convolutions[183]. The idea is to break the time-dependence of the image into discrete, overlapping "chunks" that are sliced from the full image stack by a set of $W \leq L$ windowing functions $\{\alpha^{(r)}(t)\}_{r=0}^{W-1}$. The windows are only non-zero in a small temporal window, that is, for each $r$, there exists a temporal domain $\Omega_r \subset [0, \infty)$ such that $\alpha^{(r)}(t) = 0$ for all $t \notin \Omega_r$. In the continuous representation, windowing $u(x; t)$ takes the form

* The calculation of the $j^{th}$ element of $\boldsymbol{s}$ by Eq.(5.3) requires $L$ multiplications and $(L-1)$ additions, and thus occur in $O(L)$. Obtaining the complete vector $\boldsymbol{s}$ requires this computation to occur $M$ times, and so the total complexity is $O(ML)$.

$$u(x;t) = \sum_{r=0}^{W-1} u(x;t)\alpha_r(t - rT) \tag{5.4}$$

where $T$ is the so-called "hop size", which is the temporal spacing between adjacent windows. Equality is ensured by enforcing the windows to satisfy the condition:

$$\sum_{r=0}^{W-1} \alpha_r(t - rT) = 1 \tag{5.5}$$

The approximation now comes in the form of replacing each $u(x;t)$ on the right-hand side of Eq.(5.4) with a constant value in time; this constant value is chosen as the value of $u(x;t)$ at the center of the temporal window, so that $u(x;t)\alpha_r(t - rT) \approx u(x;rT)\alpha_r(t - rT)$. That is,

$$u(x;t) \simeq \sum_{r=0}^{W-1} u(x;rT)\alpha_r(t - rT) \tag{5.6}$$

where equality holds when $W = L$. In this way, the windowing functions act as interpolants between the set of discrete points $\{u(x;rT)\}_{r=0}^{W-1}$ which approximates the continuous function $u(x;t)$. These points are still continuous in their spatial coordinate, and in the discrete representation will be represented as a set of vectors $\{\boldsymbol{u}^{(r)}\}_{r=0}^{W-1}$. This allows for the space-variant convolution to be reduced to a linear combination of regular convolutions. With this approximation Eq.(5.3) becomes

$$s_j = \sum_{k=0}^{L-1} \sum_{r=0}^{W-1} \rho_k \alpha_k^{(r)} u_{j-k}^{(r)} \tag{5.7}$$

where the discrete version of the interpolants is the same length as the pulse profile; that is, $\boldsymbol{\alpha}^{(r)} \in \mathbb{R}^{L\times 1}$ for $r = 0 \dots W-1$. In a slight abuse of notation, if a vector $\boldsymbol{u}$ is constructed by sequentially stacking the vectors $\boldsymbol{u}^{(r)}$, then the above expression is linear in $\boldsymbol{u}$ and can be written succinctly as

$$\boldsymbol{s} = \boldsymbol{A}\boldsymbol{u} \tag{5.8}$$

where $\boldsymbol{A}$ is a matrix representing the convolution with the product of the discrete temporal pulse profile $\boldsymbol{\rho}$ and the discrete interpolants $\{\boldsymbol{\alpha}^{(r)}(t)\}_{r=0}^{W-1}$. The matrix $\boldsymbol{A}$ can be efficiently calculated in the Fourier domain by modifying the so-called "efficient filter flow" method [182]:

$$\boldsymbol{A} = \sum_{r=0}^{W-1} \boldsymbol{I}_{Q,Q+1} \boldsymbol{F}^H \operatorname{diag}\left(\boldsymbol{F}\boldsymbol{Z}_\rho \operatorname{diag}(\boldsymbol{\alpha}_r)\boldsymbol{\rho}\right) \boldsymbol{F}\boldsymbol{Z}_u \boldsymbol{P}_r \tag{5.9}$$

There are many terms in this expression, defined as follows:

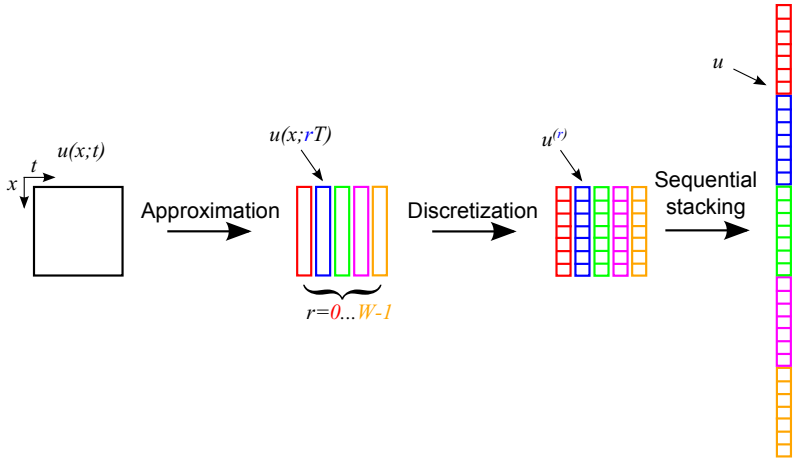


Figure 5.4.: *Illustration of the steps and approximations that lead to the formation of the vector u. First, the temporal coordinate is sampled at W points according to Eq.(5.6) to allow for interpolation. Next, the spatial coordinate is discretized. Finally, the set of W vectors is sequentially stacked to form the vector u.*

- $\boldsymbol{I}_{m,n}$ is an $m \times n$ matrix with "1"s along its diagonal
- $\boldsymbol{F}$ and $\boldsymbol{F}^H$ are the discrete Fourier transform matrix and the discrete inverse Fourier transform matrix, respectively
- $\boldsymbol{Z}_\rho$ is a matrix that appends zeros to $\boldsymbol{\rho}$ such that its length equals $Q$
- $\boldsymbol{Z}_u$ is a matrix that appends zeros to the vector $\boldsymbol{u}^{(r)}$ such that its length equals $Q$
- $\boldsymbol{P}_r$ is a matrix that chops $\boldsymbol{u}^{(r)}$ from $\boldsymbol{u}$
- $\mathrm{diag}(\boldsymbol{x})$ is a square matrix with the vector $\boldsymbol{x}$ along its diagonal

The computation of Eq.(5.8) with $\boldsymbol{A}$ expressed as in Eq.(5.9) can be performed quite quickly, on the order of $O(MW \log_2 MW)$ (ref. 182), which is significantly faster than the naïve implementation in Eq.(5.3) when $W \ll L$.

As pointed out by Hirsch *et al.* (ref. 182), this construction is extremely expressive; when $W < L$, Eq.(5.6) consists of sampling the temporal dynamics with a period of $T$ and using the $\alpha$s to interpolate between these discrete values. However, when $W = L$, the interpolants can be set to delta functions, i.e. $\boldsymbol{\alpha}_r[i] = \begin{cases} 1/L & \text{when } i = r \\ 0 & \text{otherwise} \end{cases}$, and so the full temporal dynamics are recovered. Thus the choice of $W/L$ can be used to tune the degree of approximation. Here it is recommended that $W$ is chosen as the smallest value that does not decrease the temporal resolution of the experiment. This encourages the most significant computational performance gain, while the approximation does not constitute a real loss of information

because little can be said about dynamics occurring faster than the temporal resolution anyway.

For example, representative machines have a temporal resolution of around 250 fs (ref. 168, 169, 179), and streaking typically occurs for $\sim 10\,\text{ps}$ with a streak velocity on the order of $v_s = 1\,\mu\text{m/fs}$. For standard detector pixels, means that the streak spans between 500–700 pixels with a temporal resolution between 10–20 pixels. The precision in the temporal coordinate is thus a few tens of pixels, and so $W$ would be chosen around 25.

### 5.2.2. Statistical Theory of Image Formation in UED

While Eq.(5.8) relates the "true" streaked diffraction image to the underlying time-dependent diffraction pattern, the measured streaked diffraction pattern is contaminated by measaurement noise, and it is important that this noise be properly accounted when developing the spatially-varying deconvolution algorithm. As such, this section will use the statistical framework of image formation to model the noise present in diffraction images recorded with CCD cameras.

In general, the intensity of the $(i, j)$ pixel in a CCD image is[184]

$$x_{\text{measured}}(i,j) = x_{\text{diff}}(i,j) + x_{\text{bkg}}(i,j) + x_{\text{rdn}}(i,j) \tag{5.10}$$

where $x_{\text{diff}}(i,j)$ is the intensity due to the diffracted electrons, $x_{\text{bkg}}(i,j)$ is the intensity due to the background electrons, and $x_{\text{rdn}}$ is the readout noise. This equation can be expressed more succinctly in matrix-vector notation* as $\boldsymbol{x}_{\text{measured}} = \boldsymbol{x}_{\text{diff}} + \boldsymbol{x}_{\text{bkg}} + \boldsymbol{x}_{\text{rdn}}$. Each of these intensities are random variables with different distributions. Both the diffracted and background images are limited by shot noise in the number of electrons, and so are best described by Poisson distributions, i.e. $\boldsymbol{x}_{\text{diff}} \sim \text{Poisson}(\boldsymbol{x}_{\text{diff}}; \boldsymbol{x}_{\text{true}})$ where $x_{\text{true}}(i,j)$ is the "true" image intensity of that pixel (that is, in the absence of noise), and $\text{Poisson}(x|k)$ represents a Poisson distribution over the variable $x$ with the parameters $k$. Readout noise is typically modeled by a zero-mean normal distribution[184]. These distributions will be accounted for using the following

* In matrix-vector notation, images are represented by column vectors and are designated by boldface symbols. The notation $\boldsymbol{x} \sim F(\boldsymbol{x}|\boldsymbol{k})$, where $F$ is a probability density/mass function with parameter $\boldsymbol{k}$, means that each element of $\boldsymbol{x}$ is distributed according to $F$ with the corresponding parameter from the vector $\boldsymbol{k}$. That is, $x_i \sim F(x_i|k_i)\,\forall\, x_i \in \boldsymbol{x}$. This notation is widely-used in the image-processing community.

notation:

$$\boldsymbol{x}_{\text{measured}} = \underbrace{\text{Poisson}(\boldsymbol{x}_{\text{diff}}|\boldsymbol{x}_{\text{true}})}_{\text{diffracted electrons}} + \underbrace{\text{Poisson}(\boldsymbol{x}_{\text{bkg}}|\beta\cdot\mathbf{1})}_{\text{background}} + \underbrace{\boldsymbol{\mathcal{N}}(\boldsymbol{x}_{\text{rdn}}|0,\sigma^2)}_{\text{readout noise}} \tag{5.11a}$$

$$= \text{Poisson}(\boldsymbol{x}_{\text{true}} + \beta\cdot\mathbf{1}) + \boldsymbol{\mathcal{N}}(0,\sigma^2) \tag{5.11b}$$

where the arguments have been dropped in the distributions for brevity. In this expression, $\boldsymbol{x}_{\text{true}}$ is the true image, $\mathbf{1}$ is a vector of ones, $\mathcal{N}(x|\mu,\sigma^2)$ is a normal distribution with mean $\mu$ and variance $\sigma^2$, and $\beta > 0$ and $\sigma > 0$ are sample-independent parameters that determine the noise level from background electrons and the readout of the CCD, respectively. If the scattered signal is sufficiently large, the approximation[185] $\text{Poisson}(x;k) \approx \mathcal{N}(x;k,k)$ can be used to obtain $\boldsymbol{x}_{\text{measured}} \approx \boldsymbol{x}_{\text{true}} + \beta\cdot\mathbf{1} + \boldsymbol{\mathcal{N}}(0,\delta^2)$, or, if the image is background-subtracted,

$$\boldsymbol{x}_{\text{measured}} \approx \boldsymbol{x}_{\text{true}} + \boldsymbol{\mathcal{N}}(0,\delta^2) \tag{5.12}$$

where $\delta$ is the standard deviation of the total noise. Thus the image data from a CCD array can be approximated as being corrupted additive Gaussian noise*. The assumption of Gaussian noise has been shown to be more robust for deconvolution algorithms[188], such as that presented in Section 5.3.

In reference to the formation of the streaked diffraction image, the "true" image is a pixel row from the streaked image, and so $\boldsymbol{x}_{\text{true}} = \boldsymbol{s}$, where $\boldsymbol{s}$ is given by Eq.(5.8). Therefore the streaked image formed in a UED experiment is modeled by

$$\boldsymbol{s} = \boldsymbol{A}\boldsymbol{u} + \boldsymbol{n} \tag{5.13}$$

where $\boldsymbol{n} \sim \boldsymbol{\mathcal{N}}(0,\delta^2)$ is a random variable describing the measurement noise. This relation will be used in the following section to introduce the best estimate of the time-resolved diffraction pattern from the streaked image.

## 5.3. Spatially-Varying Deconvolution

Now armed with an understanding of the underlying physics behind the streaking process, an appropriate method to analyze such experiments can be developed. The problem at hand

* The approximation of additive Gaussian noise is valid for most UED experiments, which typically have a sufficiently high signal-to-noise ratio. If one does not wish to make this approximation, the generalized Anscombe transformation $\mathbb{A} : s \mapsto 2\sqrt{s + 3/8 + \sigma^2}$ (ref. 186) can be used so that $\mathbb{A}s$ is asymptotically normally distributed. However, obtaining an unbiased inverse of this transform is challenging[187], and so the approximation in Eq.(5.12) is preferable.

can be encapsulated as follows: given a streaked image $\boldsymbol{s}$ and the matrix $\boldsymbol{A}$, constructed from the temporal pulse profile, how can the time-dependent, unstreaked diffraction pattern $\boldsymbol{u}$ be recovered from Eq.(5.13)? This is an inverse problem that is ubiquitous in imaging applications, which is unfortunate, since such problems are typically ill-posed[189]. This means that directly inverting the equation, i.e. by trying something like $\boldsymbol{u} = \boldsymbol{A}^{-1}\boldsymbol{s}$ (given an appropriate inverse $\boldsymbol{A}^{-1}$), results in an extremely large error in $\boldsymbol{u}$. As such, this section will introduce an alternative, probabilistic approach to obtain the "best" estimate of $\boldsymbol{u}$ given the structure of the measurement noise in $\boldsymbol{s}$ based on the discussion in Section 5.2.2.

Although there are several possible ways to tackle this problem, a model free approach will be adopted to limit the possibility of biasing the reconstruction*. The best estimate of the time-dependent diffraction pattern $\boldsymbol{u}$ will be chosen as the value $\hat{\boldsymbol{u}}$ that maximizes the conditional probability $p_{\boldsymbol{u}|\boldsymbol{s}}(\boldsymbol{u}|\boldsymbol{s})$, which is the probability of a certain time-dependent diffraction pattern $\boldsymbol{u}$ given the observed streaked diffraction image $\boldsymbol{s}$. According to Bayes' theorem[190], this probability, also known as the *posterior*, can be expressed as

$$p_{\boldsymbol{u}|\boldsymbol{s}}(\boldsymbol{u}|\boldsymbol{s}) = \frac{p_{\boldsymbol{s}|\boldsymbol{u}}(\boldsymbol{s}|\boldsymbol{u})\, p_{\boldsymbol{u}}(\boldsymbol{u})}{p_{\boldsymbol{s}}(\boldsymbol{s})} \tag{5.14}$$

where

- $p_{\boldsymbol{s}|\boldsymbol{u}}(\boldsymbol{s}|\boldsymbol{u})$ is the *likelihood*, which provides a measurement model for the streaked diffraction image given a proposed time-dependent diffraction pattern
- $p_{\boldsymbol{u}}(\boldsymbol{u})$ is the *prior*, which gives the probability of a proposed time-dependent diffraction pattern
- $p_{\boldsymbol{s}}(\boldsymbol{s})$ is the *evidence*, which gives the distribution of the observed streaked diffraction image

The choice of $\hat{\boldsymbol{u}} = \arg\max_{\boldsymbol{u}} p_{\boldsymbol{u}|\boldsymbol{s}}(\boldsymbol{u}|\boldsymbol{s})$ is called the *maximum a posteriori* (MAP) estimate

* An example of a model-based approach would be, for instance, assuming that $u$ is of the form $u(x, y; t) = A(t) \exp\left[-\frac{(x-x_0(t))^2+(y-y_0(t))^2}{2\sigma^2(t)}\right]$

for $\boldsymbol{u}$. Following from Eq.(5.14), this estimate is given by

$$\hat{\boldsymbol{u}} = \arg\max_{\boldsymbol{u}} \frac{p_{\boldsymbol{s}|\boldsymbol{u}}(\boldsymbol{s}|\boldsymbol{u})\, p_{\boldsymbol{u}}(\boldsymbol{u})}{p_{\boldsymbol{s}}(\boldsymbol{s})} \tag{5.15a}$$

$$= \arg\max_{\boldsymbol{u}} p_{\boldsymbol{s}|\boldsymbol{u}}(\boldsymbol{s}|\boldsymbol{u})\, p_{\boldsymbol{u}}(\boldsymbol{u}) \tag{5.15b}$$

$$= \arg\max_{\boldsymbol{u}} \log\left[p_{\boldsymbol{s}|\boldsymbol{u}}(\boldsymbol{s}|\boldsymbol{u})\, p_{\boldsymbol{u}}(\boldsymbol{u})\right] \tag{5.15c}$$

$$= \arg\max_{\boldsymbol{u}} \left\{\log\left[p_{\boldsymbol{s}|\boldsymbol{u}}(\boldsymbol{s}|\boldsymbol{u})\right] + \log\left[p_{\boldsymbol{u}}(\boldsymbol{u})\right]\right\} \tag{5.15d}$$

$$= \arg\min_{\boldsymbol{u}} \left\{-\log\left[p_{\boldsymbol{s}|\boldsymbol{u}}(\boldsymbol{s}|\boldsymbol{u})\right] - \log\left[p_{\boldsymbol{u}}(\boldsymbol{u})\right]\right\} \tag{5.15e}$$

where the introduction of the logarithms is a common approach to simplify the expressions, and is valid since logarithms are monotonically increasing. Since image formation in UED streaking experiments follows the model $\boldsymbol{s} = \boldsymbol{A}\boldsymbol{u} + \boldsymbol{n}$, and the expectation value of the noise is zero, it follows that*

$$p_{\boldsymbol{s}|\boldsymbol{u}}(\boldsymbol{s}|\boldsymbol{u}) = p_{\boldsymbol{n}}(\boldsymbol{s} - \boldsymbol{A}\boldsymbol{u}) \tag{5.16}$$

where $p_{\boldsymbol{n}}(\boldsymbol{n}) = \boldsymbol{\mathcal{N}}(0, \delta^2) = (2\pi\delta^2)^{-Q/2} \exp\left(-\|\boldsymbol{n}\|_2^2 / 2\delta^2\right)$ is the distribution of the noise†. If this is substituted back into Eq.(5.15e), then

$$\hat{\boldsymbol{u}} = \arg\min_{\boldsymbol{u}} \left\{-\log\left[p_{\boldsymbol{s}|\boldsymbol{u}}(\boldsymbol{s}|\boldsymbol{u})\right] - \log\left[p_{\boldsymbol{u}}(\boldsymbol{u})\right]\right\} \tag{5.17a}$$

$$= \arg\min_{\boldsymbol{u}} \left\{-\log\left[\frac{1}{(2\pi\delta^2)^{Q/2}} \exp\left(-\frac{1}{2\delta^2}\|\boldsymbol{s} - \boldsymbol{A}\boldsymbol{u}\|_2^2\right)\right] - \log\left[p_{\boldsymbol{u}}(\boldsymbol{u})\right]\right\} \tag{5.17b}$$

$$= \arg\min_{\boldsymbol{u}} \left\{-\log\left[\frac{1}{(2\pi\delta^2)^{Q/2}}\right] + \frac{1}{2\delta^2}\|\boldsymbol{s} - \boldsymbol{A}\boldsymbol{u}\|_2^2 - \log\left[p_{\boldsymbol{u}}(\boldsymbol{u})\right]\right\} \tag{5.17c}$$

$$= \arg\min_{\boldsymbol{u}} \left\{\frac{1}{2\delta^2}\|\boldsymbol{s} - \boldsymbol{A}\boldsymbol{u}\|_2^2 - \log\left[p_{\boldsymbol{u}}(\boldsymbol{u})\right]\right\} \tag{5.17d}$$

$$= \arg\min_{\boldsymbol{u}} \left\{\|\boldsymbol{s} - \boldsymbol{A}\boldsymbol{u}\|_2^2 - 2\delta^2 \log\left[p_{\boldsymbol{u}}(\boldsymbol{u})\right]\right\} \tag{5.17e}$$

The best estimate of the time-dependent diffraction pattern $\boldsymbol{u}$ is chosen as the familiar least-squares solution, modified by the *prior* distribution over $\boldsymbol{u}$. The most straight-forward choice

* Although this equality might not be obvious, it can be arrived at by the following steps: if $\boldsymbol{s} = \boldsymbol{y} + \boldsymbol{n}$, the distribution of $\boldsymbol{s}$ can be computed by integrating the joint probability $p_{\boldsymbol{y},\boldsymbol{n}}(\boldsymbol{y}, \boldsymbol{n})$ along the line $\boldsymbol{s} = \boldsymbol{y} + \boldsymbol{n}$. That is, $p_{\boldsymbol{s}}(\boldsymbol{s}) = \int p_{\boldsymbol{y},\boldsymbol{n}}(\boldsymbol{y}, \boldsymbol{n})\, \mathrm{d}\boldsymbol{y} = \int p_{\boldsymbol{y}}(\boldsymbol{y}) p_{\boldsymbol{n}}(\boldsymbol{s} - \boldsymbol{y})\, \mathrm{d}\boldsymbol{y}$, where the second equality follow from the assumption that $\boldsymbol{y}$ and $\boldsymbol{n}$ are independent. Alternatively, $p_{\boldsymbol{s}}(\boldsymbol{s}) = \int p_{\boldsymbol{y}}(\boldsymbol{y}) p_{\boldsymbol{s}|\boldsymbol{y}}(\boldsymbol{s}|\boldsymbol{y})\, \mathrm{d}\boldsymbol{y}$, where $p_{\boldsymbol{s}|\boldsymbol{u}}$ is the conditional probability, and comparing these two expressions results in Eq.(5.16).

† The notation $\|\boldsymbol{x}\|_2 = \sqrt{\sum_{i=1}^{n} |x_i|^2}$, where $x$ is a vector of $n$ elements, will be used to represent the $\ell^2$-norm.

for $p_{\boldsymbol{u}}$ would be a uniform prior, i.e. assuming all values of $\boldsymbol{u}$ are equally likely and choosing the value $\hat{\boldsymbol{u}}_{\mathrm{ML}} = \arg\min_{\boldsymbol{u}} \|\boldsymbol{s} - \boldsymbol{A}\boldsymbol{u}\|_2^2$ which most closely matches the data. This is known as the *maximum likelihood* (ML) estimate, and reflects the desire for a model-free solution as to not bias the choice of $\boldsymbol{u}$. Unfortunately, such estimates often produce physically meaningless results, even if $\boldsymbol{A}\hat{\boldsymbol{u}}_{\mathrm{ML}}$ is very close to the experimental data. As such, in this situation it is preferable to use the full MAP estimate, accounting for some prior knowledge of $\boldsymbol{u}$ which penalizes solutions that are improbable.

Adding a term to the least-squared minimization problem, such as in Eq.(5.17e), is known as *regularization*, and helps stabilize the ill-conditioned inverse problem. When using regularization, it is typical to use a modification of the form $-2\delta^2 \log\left[p_{\boldsymbol{u}}(\boldsymbol{u})\right] = \mu\Omega(\boldsymbol{u})$, giving

$$\hat{\boldsymbol{u}} = \arg\min_{\boldsymbol{u}} \left\{ \|\boldsymbol{s} - \boldsymbol{A}\boldsymbol{u}\|_2^2 + \mu\Omega(\boldsymbol{u}) \right\} \tag{5.18}$$

where $\Omega(\boldsymbol{u})$ is the regularizer and $\mu \geq 0$ is a parameter that allows for tuning the degree of regularization by balancing the fidelity to the data with satisfying the regularizer. There are several potential avenues for $\Omega(\boldsymbol{u})$ to pursue here, all based on physical properties of $u(x, y; t)$ (for the following discussion, it will be more helpful to work with the continuous representation):

1. The most obvious choice would be to use the fact that the time-dependent diffraction pattern should be pretty similar to the unstreaked, unpumped diffraction image $u(x, y; 0)$. This could be accomplished by using a term such as $\Omega(\boldsymbol{u}) = \|\boldsymbol{u} - \boldsymbol{u}_0\|_2^2$, where $\boldsymbol{u}_0$ is the discrete form of $u(x, y; 0)$.

2. Since $u(x, y; t)$ is ultimately a function of the scattering potential, which is a smooth function of space, $u(x, y; t)$ must also vary smoothly in its spatial coordinates. In terms of the approximation, this means each $\boldsymbol{u}^{(r)}$ must be smooth. This can be encouraged through Tikhonov regularization* with the addition of the term $\Omega(\boldsymbol{u}) = \sum_{r=0}^{W-1} \left\| \boldsymbol{D}_1 \boldsymbol{u}^{(r)} \right\|_2^2$ where $\boldsymbol{D}_1$ is a discrete approximation of the first derivative operator. Making use of the projection operator $\boldsymbol{P}_r$ that chops $\boldsymbol{u}^{(r)}$ from $\boldsymbol{u}$, then this term can be written in terms of the total target vector $\boldsymbol{u}$ as $\Omega(\boldsymbol{u}) = \sum_{r=0}^{W-1} \|\boldsymbol{D}_1 \boldsymbol{P}_r \boldsymbol{u}\|_2^2$.

3. By the same argument, $u(x, y; t)$ must vary smoothly in its temporal coordinate. The regularization associated with this encourages similarity between neighbouring vectors $\boldsymbol{u}^{(r)}$, and takes the form $\Omega(\boldsymbol{u}) = \sum_{i=0}^{M-1} \|\boldsymbol{D}_1 \boldsymbol{\Pi}_i \boldsymbol{u}\|_2^2$ where $\boldsymbol{\Pi}_i \boldsymbol{u} = [u_i^{(0)}, u_i^{(1)}, \ldots, u_i^{(W-1)}]^T$ is a vector containing the temporal evolution of the $i^{\text{th}}$ pixel of $u(x; \cdot)$.

4. The temporal changes of the diffraction pattern are small for most experiments, and so it is not unreasonable to think that the total intensity of a diffraction image is constant in time. For instance, if a Bragg peak loses intensity due to the Debye-Waller effect,

* The term Tikhonov regularization is used to describe any regularizer of the form $\Omega(\boldsymbol{u}) = \|\boldsymbol{\Gamma}\boldsymbol{u}\|_2^2$, where $\boldsymbol{\Gamma}$ is a general matrix.

the diffuse background must increase accordingly. To account for this, the condition $||\boldsymbol{u}^{(r)}||_1 = ||\boldsymbol{u}^{(0)}||_1$ for $1 \leq r \leq N-1$ could be enforced. However, depending on the amount of noise in the UED experiment, the condition of constant intensity might be invalid in practice.

5. If the location of $t = 0$ (the arrival of the pump pulse) is known exactly, then the regularization could make use the fact that $u(x, y; t < 0)$ should be constant in time. Differences are thus penalized according to $\Omega(\boldsymbol{u}) = \sum_{i=0}^{\tau-1} \|\boldsymbol{D}_1 \boldsymbol{\Pi}_i \boldsymbol{u}\|_2^2$, where $\tau$ is the pixel location of $t = 0$ along the $x$-axis.

6. Although this does not take the form of regularization, the constraint $\boldsymbol{u} \geq 0$ can be imposed, which follows from the nature of detection.

In various situations, different combinations of these terms may be more suitable than others, although it is recommended that as only one or two of the terms is used to avoid over-regularizing the solution. Regularizer 1 is promising since it uses a key additional piece of information that comes for "free" in UED streaking experiments, although it might penalize time-dependent diffraction patterns which undergo expansions and contractions. In this regard, regularizers 2, 3, and 6 are preferable since they are general properties of any diffraction pattern and so do not penalize any specific dynamics. Regularizer 5 also falls into this category since it applies to all time-dependent diffraction patterns, but since it is difficult to pin-point the location of $t = 0$ precisely, in practice it might penalize rapid dynamics that occur near $t = 0$.

Based on this discussion, various combinations of regularizers 2, 3, and 6 were attempted on the simulated UED data presented in Section 5.5 to find a cursory rule as to which terms are ideal for UED experiments. It was found that encouraging spatial smoothness had little influence on the recovered diffraction pattern, but the positivity constraint and encouraging temporal smoothness promoted a physically realistic solution. Therefore, the recommended regularized least squares problem for streaked UED data is

$$\hat{\boldsymbol{u}} = \underset{\boldsymbol{u} \geq 0}{\arg\min} \left\{ \|\boldsymbol{s} - \boldsymbol{A}\boldsymbol{u}\|_2^2 + \mu \sum_{i=0}^{M-1} \|\boldsymbol{D}_1 \boldsymbol{\Pi}_i \boldsymbol{u}\|_2^2 \right\} \tag{5.19}$$

## 5.4. Practical Aspects of the Reconstruction

There are several necessary practical steps to implement the reconstruction scheme using Eq.(5.19). Each of these will be discussed individually below.

### 5.4.1. Identification of Streaking Direction

The angle between the streaking direction and the pixel axes needs to be accounted for; it could be identified, for instance, as the angle giving the largest value of the radial projection of the Radon transform of the streaked image, i.e.

$$\theta_{\text{streak}} = \arg\max_{\theta} \int_0^{\infty} \int_{-\infty}^{\infty} \int_{-\infty}^{\infty} s(x,y)\delta(\rho - x\cos\theta - y\sin\theta)\,\mathrm{d}x\,\mathrm{d}y\,\mathrm{d}\rho \tag{5.20}$$

The image rotation could then be carried out using area mapping. This approach was taken for the experimental data presented in Section 5.6, but was unnecessary for the simulated data in Section 5.5 since the patterns were intentionally streaked along one of the pixel axes.

### 5.4.2. Computation of the Regularization Matrix

To implement the regularization, it is recommended to use a simple, invertible choice for the discrete first derivative matrix $\boldsymbol{D}_1$, such as

$$\boldsymbol{D}_1 = \begin{pmatrix} -1 & 1 & & & & & \\ & -1 & 1 & & & & \\ & & -1 & 1 & & & \\ & & & \ddots & \ddots & & \\ & & & & & -1 & 1 \end{pmatrix} \tag{5.21}$$

The matrix $\boldsymbol{\Pi}_i$ has dimensions $W \times MW$, and is filled with zeros except when $\boldsymbol{\Pi}_i[r, rM+i] = 1$ for $r \in [0, W-1]$.

### 5.4.3. Choice of the Regularization Parameter

The most important aspect of solving Eq.(5.19) is the choice of the regularization parameter $\mu$, since it controls the balance between matching the experimental data and the smoothness constraint. It must be carefully chosen to ensure a physically relevant solution without over-smoothing the data. Fortunately, UED experiments have access to an extra piece of information that can inform the choice for $\mu$: an estimate of the amount of noise in the images. This suggests using the so-called "discrepancy principle" to choose the regularization parameter[191], which states that, because the measurement is contaminated by an amount $\|\boldsymbol{s} - \boldsymbol{A}\boldsymbol{u}\|_2 = \|\boldsymbol{n}\|_2$, the reconstruction is acceptable if

$$\|\boldsymbol{s} - \boldsymbol{A}\hat{\boldsymbol{u}}(\mu)\|_2 \leq \delta \tag{5.22}$$

where $\delta^2 = \mathbb{E}\left(\|\boldsymbol{n}\|_2^2\right)$ is an estimation of the noise level and $\mathbb{E}(\cdot)$ represents the expectation value. That is, because the experimental data can differ from the "true" streaked diffraction pattern by an amount $\sim \delta$, the regularization parameter is chosen as the largest value that allows the reconstructed streaked image to stay within this noise level. This provides the maximum allowed smoothing while still remaining faithful to the experimental data. Practically, the discrepancy principle is implemented as choosing $\mu$ as the zero of the function $f(\mu) = \|\boldsymbol{s} - \boldsymbol{A}\hat{\boldsymbol{u}}(\mu)\|_2^2 - c^2\delta^2$, where $c \geq 1$ is a small constant (in the results shown below, $c = 1.1$). Since this relies on the solution $\hat{\boldsymbol{u}}$ (which, in turn, relies on the choice of $\mu$), it is preferable to rewrite $f(\mu)$ as

$$f(\mu) = \sum_{i=0}^{q-1} \left(\frac{\mu}{d_i'^2 + \mu}\right)^2 s_i'^2 + \sum_{i=q}^{k-1} s_i'^2 - c^2\delta^2 \tag{5.23}$$

which is derived in Appendix A. The definition of the terms $d_i'$, $q$ and $s_i'$ in this expression are derived from $\boldsymbol{A}$ and $\boldsymbol{s}$, and are also introduced in Appendix A and so will be omitted here for brevity.

To experimentally estimate $\delta$, two streaked images $\boldsymbol{s}^{(1)}$ and $\boldsymbol{s}^{(2)}$ should be measured under the same conditions (i.e. with the same sample, the same excitation fluence, etc.). Since the only difference between these two images is the realization of the noise, some algebra shows that $\delta = \sqrt{Q}\sigma$ where $\sqrt{2}\sigma$ is the standard deviation of the distribution of the pixel intensities in the difference image $\boldsymbol{s}^{(2)} - \boldsymbol{s}^{(1)}$ (see Appendix A).

### 5.4.4. Choice of the Interpolants

The interpolants were chosen to be $K$-point symmetric Hann windows, given by

$$\alpha_r[n] = \begin{cases} \frac{1}{2}\left[1 - \cos\left(\frac{2\pi n}{K-1}\right)\right] & \text{when } rT \leq n \leq rT + K \\ 0 & \text{otherwise} \end{cases} \tag{5.24}$$

To enforce Eq.(5.5), the windows were chosen to overlap by 50 %, so given a streak length $L$ the length of the windows $K$ and the hop size $T$ were chosen accordingly. The results in the following sections used $W = L/8$.

### 5.4.5. Implementation

Once the regularization parameter was aptly chosen, the minimization of Eq.(5.19) was performed by a simple steepest descent algorithm with the step size chosen according to a backtracking line search as implemented in ref. 192. The positivity of $\boldsymbol{u}$ was enforced by a two-point bound projection method. All computations were performed with custom-written software in MATLAB R2015a (The Mathworks, USA).

## 5.5. Results: Simulated Data

The spatially-varying deconvolution approach, which culminates in Eq.(5.19), was applied to simulated streaked time-dependent diffraction patterns. Each diffraction pattern was a $32 \times 32$ image containing a single symmetric Gaussian spot with a standard deviation of 9.6. The spot was streaked over $L = 256$ pixels by a temporally Gaussian pulse profile with a standard deviation of $L/2$. White Gaussian noise was randomly added to the images at a signal-to-noise ratio* of 50, unless otherwise stated.

To demonstrate the versatility and flexibility of this procedure, a wide range of temporal dynamics were simulated to cover the most common behaviour of transient diffraction patterns. In general, the changes in the intensities, positions, and widths of the diffraction peaks incorporate the full range of possible changes that can arise from a laser-irradiated crystal. For instance, changes in peak intensities could be attributed to temperature increases due to the Debye-Waller effect or to the excitation of optical phonons, changes in peak positions are related to expansions/contraction of the unit cells, and changes in the peak widths could result from the presence of acoustic phonons.

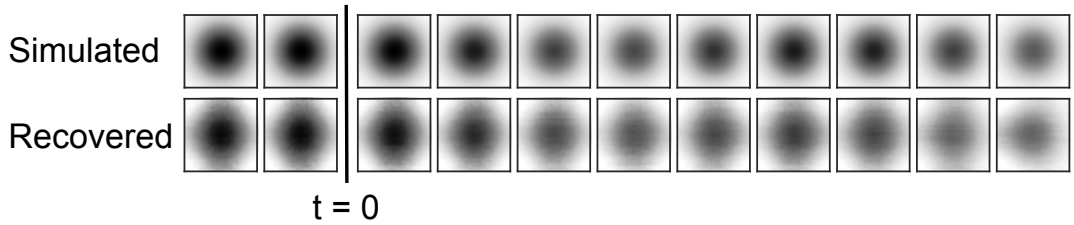


Figure 5.5.: *Demonstration of the spatially-varying deconvolution algorithm's ability to recover a time-dependent diffraction pattern. The upper row contains selected simulated (input) instantaneous diffraction patterns, and the lower row shows the corresponding recovered (output) patterns.*

Shown in the upper row of Fig. 5.5 is a diffraction spot which, after $t = 0$, begins to oscillate and decay in intensity, with an amplitude given by $[1 + 0.1\cos(6\pi t/L)]\exp(-t/1000)$. The

* The signal-to-noise ratio was defined as $\mu/\sigma$, where $\mu$ is the mean intensity of the streaked image and $\sigma$ is standard deviation of the noise.

lower row contains the diffraction images at the corresponding times that were reconstructed using Eq.(5.19). From visually inspecting these images it is evident that the technique developed in this chapter does an extremely good job at recovering the underlying dynamics. Comparing the two sets of images confirms that the shape, position, and intensity of the diffraction spot is fairly accurately reproduced, perhaps with a few small artifacts. The fidelity of the recovered diffraction images to the input, simulated images persists both before and after $t = 0$, which is indicative of the spatially-varying deconvolution algorithm's ability to catch the onset of the dynamics.

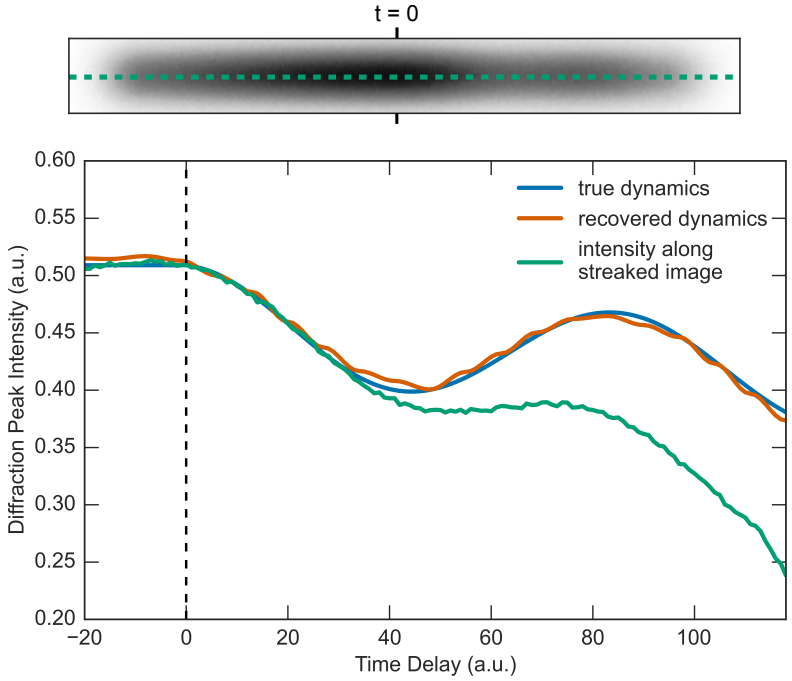


Figure 5.6.: *Comparison between the time-dependent amplitude of a simulated diffraction spot recovered by the spatially-varying deconvolution algorithm and the traditional approach to analyze streaked diffraction (by taking the intensity along the streaked image)*

The successful recovery is even more apparent in Fig. 5.6, which plots the average diffraction spot intensity as a function of the time delay taken from the sequence of images in Fig. 5.5. Qualitatively, the amplitude of the recovered diffraction pattern very closely matches the true (input) dynamics. In fact, the mean error between the two is only $\sim 1\,\%$. This result reassures that the spatially-varying deconvolution algorithm introduced in this chapter is capable of retrieving the underlying dynamics.

Also shown in Fig. 5.6 is the diffraction peak amplitude measured by the traditional approach of taking the intensity profile along the streaked image (which, in this case, is indicated by the dashed line in the streaked image shown over the figure). The traditional method both severely underestimates the amplitude and the period of the oscillations, as well as overestimating the decay time of the dynamics. Thus using this approach could lead to erroneous conclusions about the time-scales of the dynamics measured with streaked diffraction tech-

niques. The novel analysis tool presented in this chapter successfully and accurately recovers the true dynamics, and so it is important to emphasize that it is the *correct and only* way that streaked diffraction patterns should be analyzed. This highlights the importance of using Eq.(5.19) as opposed to traditional, naïve approaches.

To investigate the applicability of Eq.(5.19) to different types of dynamics, two further simulations were performed: one of a diffraction spot that oscillates in size (due to, for instance, acoustic phonons), and another of a diffraction spot that changes its position (due to, for instance, lattice contractions/expansions). The results of these two cases are shown in Fig. 5.7 and Fig. 5.8, respectively. The top portion of these figures show the streaked diffraction image, and the bottom shows a comparison between some of the instantaneous diffraction patterns. In the case where the spot width changes, it is evident that again the spatially-varying deconvolution approach does a decent job at recovering the underlying dynamics. There appears to be a bit of asymmetry in the recovered diffraction spot shape that has a slight time-dependence, but the overall spot width closely matches the input data. A similar result is observed for the situation in which the diffraction spot changes its position. Although the time-dependent position of the peak is fairly well reproduced, the recovered diffraction pattern appears to match more closely along one axis than the other. It in unclear if this is a systematic discrepancy or is an artifact of the data input here. This result needs further investigation into how to address the issue and what effects it has on the interpretation of the time-dependent diffraction pattern.

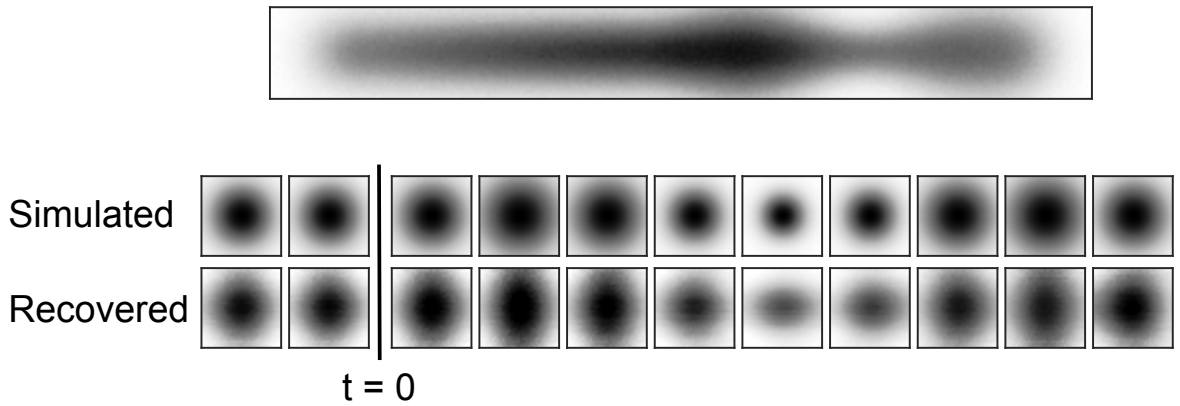


Figure 5.7.: *Simulated streaked image of a diffraction spot undergoing oscillations in its width after $t = 0$. The lower panel compares the simulated and recovered instantaneous diffraction patterns taken at selected times throughout the dynamics.*

One final case was simulated, involving two small diffraction peaks with overlapping streaked trajectories. After $t = 0$ the two peaks oscillate in intensity. In previous experiments, this is a situation that has been carefully avoided since with the traditional analysis technique it is impossible to separate the dynamics of the two spots individually. However, as UED is being applied to samples with more complicated crystal structures, overlapping diffraction spots might be unavoidable in future streaking experiments. Because of this, it is interesting to see how the spatially-varying deconvolution of this chapter performs on such cases.

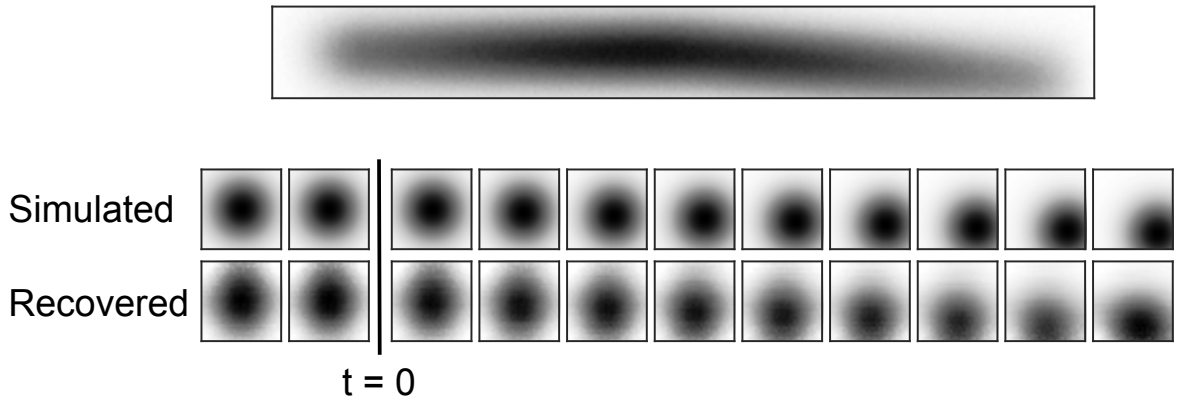


Figure 5.8.: *Simulated streaked image of a diffraction spot undergoing a time-dependent shift in its position after $t = 0$. The lower panel compares the simulated and recovered instantaneous diffraction patterns taken at selected times throughout the dynamics.*

Fig. 5.9 shows the results of applying the algorithm to the streaked data shown in the upper portion of the figure. The recovered instantaneous diffraction patterns indicate that that the algorithm presented here is powerful enough to consider overlapping diffraction spots. The presence of two diffraction spots are successfully reproduced, and qualitatively it appears that the time-dependent amplitudes of the two peaks corresponds to the input dynamics. Although preliminary, the results suggested by this figure indicate that the spatially-varying deconvolution opens up the streaked diffraction technique to a new broad class of samples.

In all of the cases presented above the regularization parameter computed by the discrepancy principle was very small, i.e. $\mu \approx 0.001$ or smaller, which indicates that very little regularization is required to obtain an acceptable reconstruction.

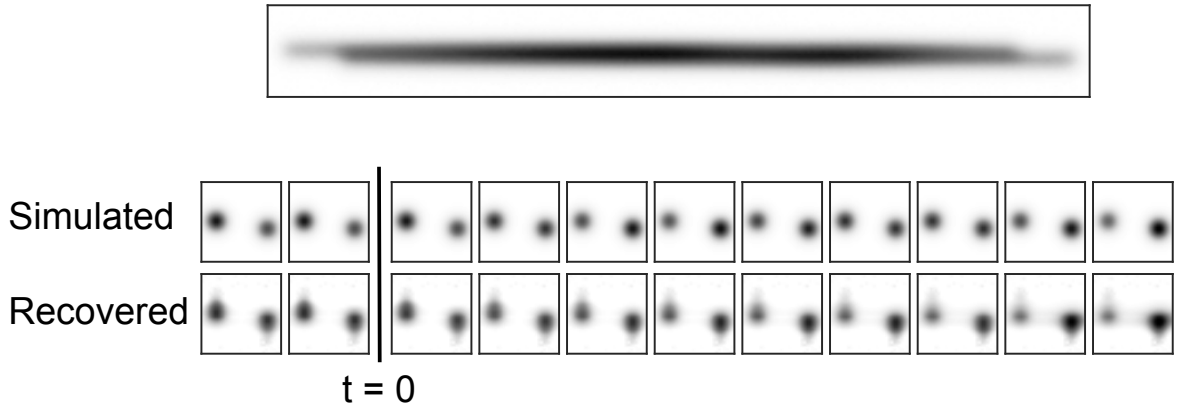


Figure 5.9.: *Simulated streaked image of two diffraction spots with trajectories which overlap during streaking. After $t = 0$, the spots begin to oscillate in intensity. The lower panel compares the simulated and recovered instantaneous diffraction patterns taken at selected times throughout the dynamics.*

## 5.6. Results: Experimental Data

While the results of the preceding section are promising, the true test of the power of this novel analysis technique is the successful demonstration of its applicability to experimental data. This section takes on this foreboding task, using the experimental data of Eichberger, Erasmus, *et al.* (ref. 169). This data was acquired using a state-of-the-art ultrafast electron diffractometer equipped with one of the fastest modern streak cameras which is capable of obtaining sub-250 fs temporal resolution[169]. The sample which they studied was the charge-density wave compound $4H_b$-$TaSe_2$ which undergoes a photo-induced commensurate to incommensurate phase transition when pumped with a near-infrared laser. These dynamics are associated with a diffraction peak with an amplitude that decays exponentially on a time-scale of $\sim 550$ fs (ref. 169).

The top panel of Fig. 5.10 displays the experimental data both pumped and unpumped by the excitation laser. The diffraction patterns were streaked over a range of $\sim 6$ ps, and it is evident from the pumped image that the decaying amplitude starts part way through the streak. With the available experimental data, the temporal electron pulse profile is unknown, and so must be determined before Eq.(5.1) can be applied to recover the underlying diffraction pattern. Fortunately, the same equation governs the streaking process, and the unpumped image can be written as $s_{\text{unpumped}}(x, y) = \int_{-\infty}^{\infty} \rho(t) u(x - v_s t, y; 0)\, \mathrm{d}t$. Since this is a straightforward convolution, traditional deconvolution methods can be used to obtain $\rho(t)$ from both $s_{\text{unpumped}}(x, y)$ and $u(x, y; 0)$. It should be noted that this has been previously identified in ref. 178, 181. After the pulse profile was recovered, Eq.(5.1) was applied on the pumped streaked image shown in Fig. 5.10 to obtain the retrieve the underlying time-dependent diffraction pattern. The recovered time-dependent diffraction peak is not quite circular, and it maintains this shape throughout the dynamics. This could be improved upon, perhaps, by using a different regularization term or a combination of terms. The dynamics are as one would expect, with the intensity rapidly decaying after $t = 0$. This is very promising since the same result was obtained with a conventional pump-probe UED setup, as presented in ref. 169.

Fig. 5.11 further investigates the quality of the reconstruction by comparing the recovered amplitude to the intensity profile taken along the streaked image (i.e. the traditional method). Plotted is the fractional intensity change $(I_{\text{pumped}} - I_{\text{unpumped}})/I_{\text{unpumped}}$, where $I$ is the image intensity averaged over the transverse axis to the streaking direction. Both approaches show similar dynamics, with the fractional change rapidly dropping to -1 (that is, $I_{\text{pumped}} = 0$). The most striking difference is the timescale on which the decay takes place. The traditional analysis approach results in an intensity that decays on the $\sim 500$ fs timescale whereas the recovered diffraction decays in $\sim 1$ ps. This is the same trend that was identified in the simulated results shown in Fig. 5.6, where the streaked image decayed on a faster timescale, and the recovered amplitude matched the input, true dynamics. While this implies that the true timescale of the charge density wave phase transition is the one recovered by the spatially-varying deconvolution algorithm, the amplitude of the streaked image more closely matches the timescale measured with a conventional stroboscopic UED setup[169]. This observation

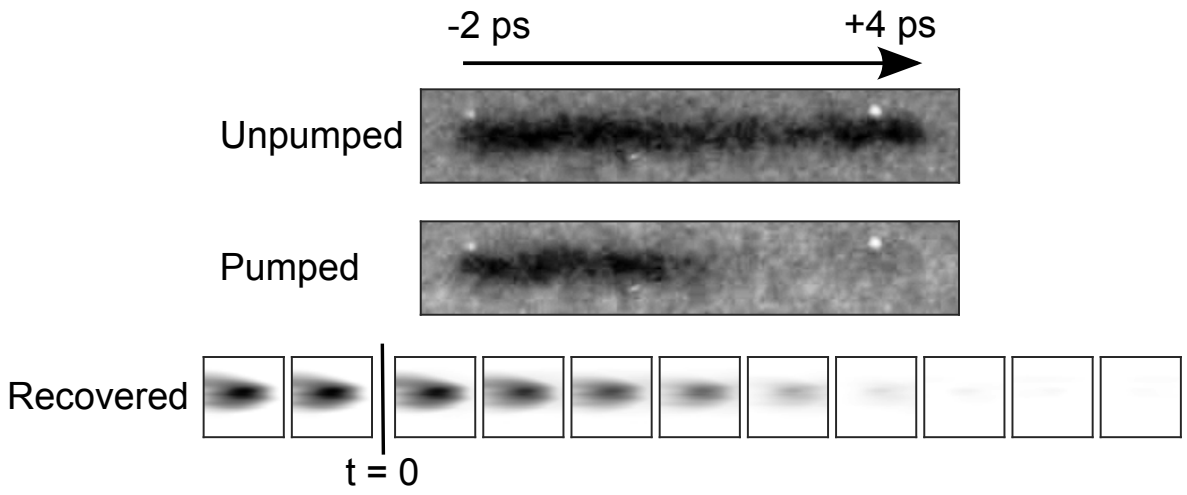


Figure 5.10.: *Experimentally measured streaked diffraction patterns of the charge-density wave compound $4H_b$-$TaSe_2$ both pumped and unpumped with the excitation laser. This data is reproduced from (ref. 169) with permission. The lower panel displays the time-dependent diffraction spot recovered with Eq.*(5.1).

requires a more thorough analysis than will presented here to explore the implications of these results on the interpretation of the dynamics in $4H_b$-$TaSe_2$.

## 5.7. Effect of the Signal-to-Noise Ratio on the Quality of the Reconstruction

Using again the simulated data with the oscillating and decaying amplitude, this section will investigate how effectively the reconstruction algorithm works in the presence of significant noise contamination. Inset in Fig. 5.12 are several of the streaked diffraction images with different Signal-to-Noise Ratio (SNR) values. These images were processed by Eq.(5.19), resulting in the recovered time-dependent amplitudes shown in Fig. 5.12 B. Unexpectedly, the images with higher noise resulted in a worse reconstruction. This is highlighted in Fig. 5.12 A, which plots the percent error mean($|\boldsymbol{u}_{\text{recovered}} - \boldsymbol{u}_{\text{true}}|/\boldsymbol{u}_{\text{true}}$) for several SNR values. Interestingly, even in situations severely contaminated with noise, such as SNR = 1, the reconstruction technique works quite well. This is likely due to the combined effects of an effective initial guess of the solution and the fact that these dynamics solely consisted of amplitude changes. Fortunately, typical UED experiments work in the SNR $> 50$ regime[193], with modern machines even operating with SNR values of a few hundred[162,193]. This is an encouraging results that speaks to the practicality of analysis approach presented in this chapter.

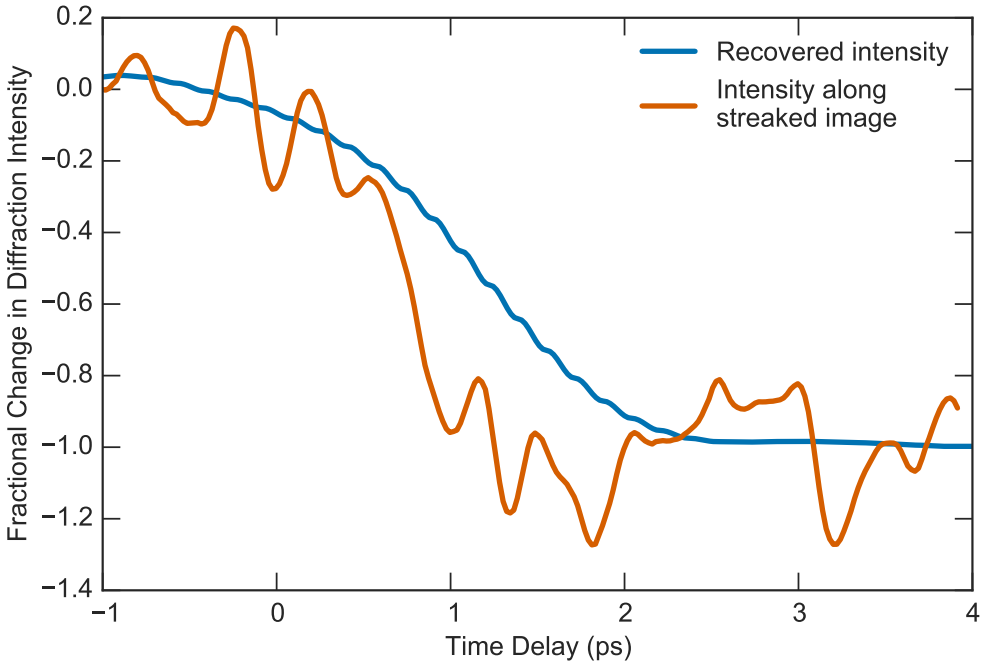


FIGURE 5.11.: *Transient fractional change in intensity* $((I_{pumped} - I_{unpumped})/I_{unpumped})$ *of the charge density wave diffraction peak in photo-irradiated* $4H_b$*-*$TaSe_2$ *measured by two methods: the traditional approach, by taking the intensity along the streaking direction of the streaked image, and the intensity recovered by the spatially-varying deconvolution algorithm*

## 5.8. Open Questions and Future Directions

Although the UED chamber introduced in Chapter 3 was intentionally optimized for studying thin films, it is inherently limited to the subset of species that exhibit reversible reactions. Because of this, it cannot be used, for example, to experiment on the GO system presented in Chapter 2. To this end, this chapter expanded upon the ultrafast streaking technique, and presented an analysis procedure that allows for the full time-dependent diffraction pattern to be recovered from a single streaked image. This opens up the UED method to study the full range of possible dynamics. Combined with the innovative design principles presented in Chapter 3, it should now be possible to design a low-energy UED setup equipped with an ultrafast streak camera to study irreversible reactions in thin films.

While this chapter has laid the foundation of the analysis of ultrafast streaked diffraction patterns, there are still a few open questions that need to be addressed: in conventional streaking experiments, the temporal resolution is limited by the spatial resolution of the image, which is usually taken to be the width of the unstreaked diffraction peak. However, with the novel algorithm presented here the recovered time-dependent diffraction pattern is not limited by the spatial resolution of the streaking; in fact, a unique instantaneous diffraction pattern is returned for each pixel along the streaked image. Accordingly, it is

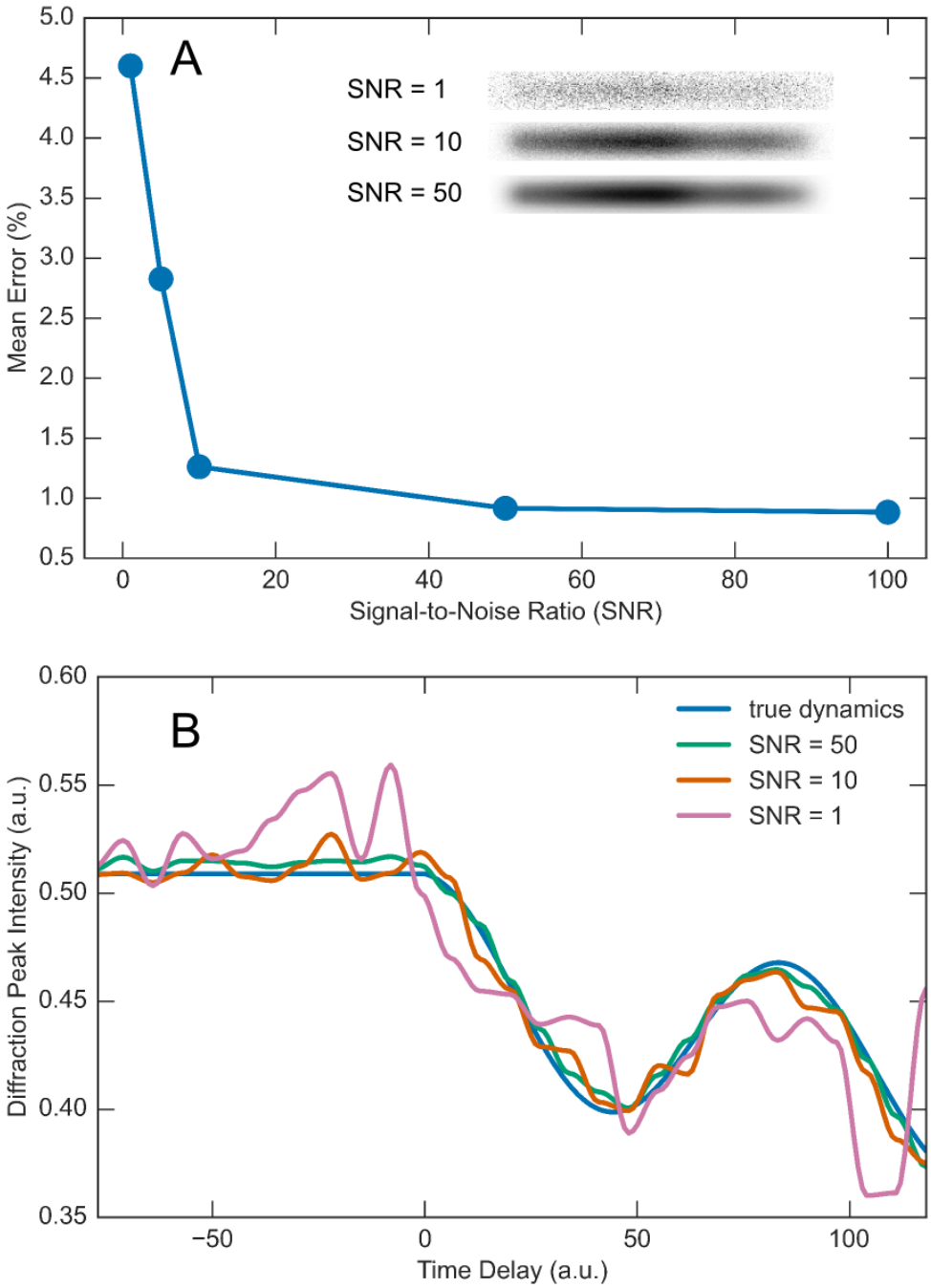


Figure 5.12.: *(A) Mean percent error in the recovered diffraction patterns for various signal-to-noise ratios (SNR). Inset are examples of streaked diffraction spots with different SNR values. (B) Comparison of the recovered diffraction spot amplitudes for various SNR values.*

speculated that the temporal resolution of the deconvolution approach is instead limited by the temporal overlap of the pump and probe pulses. If true, this would dramatically improve the temporal resolution of such experiments. This proposition begs for further exploration.

Also, as previously noted, it is unclear how the analysis of the experimental data in Section 5.6 influences the interpretation of the dynamics in $4H_b$-$TaSe_2$. It would be of interest to conduct controlled streaking experiments of a simpler, well-known material to provide a stepping stone toward samples with complex structures such as charge density wave materials.

There are additionally some refinements that could improve the quality and speed of the reconstruction of the instantaneous diffraction pattern. For instance, instead of using fixed windows as the interpolants, it is possible to alternatively solve Eq.(5.19) for $\hat{\boldsymbol{u}}$ and $\hat{\boldsymbol{\alpha}} = \arg\min_{\boldsymbol{\alpha}\geq 0}\|\boldsymbol{s} - \boldsymbol{A}(\boldsymbol{\alpha})\hat{\boldsymbol{u}}\|_2^2$ where $\boldsymbol{\alpha} = [\boldsymbol{\alpha}^{(0)}; \boldsymbol{\alpha}^{(1)}; \ldots \boldsymbol{\alpha}^{(W-1)}]$ is a vector formed by stacking the individual discrete interpolants and $\boldsymbol{A}(\boldsymbol{\alpha})$ is given by Eq.(5.9). This approach has been used in ref. 194 to address a similar problem, and the authors found that it significantly improved the quality of the reconstruction by reducing the root-mean squared error by a factor of 4.

Another possible avenue to explore would be the parallel implementation of the spatially-varying deconvolution algorithm either on multi-threaded CPUs or on GPUs. As this would dramatically reduce the computation time (since each row in the image could be analyzed in parallel instead of serially), the number $W$ of interpolants could be larger, producing a better quality reconstruction.

It is worth noting that the analysis of streaked, time-dependent diffraction is formally analogous to the processing of blurry photographs. As such, the contents of this chapter could benefit from borrowing from results developed in that field (see, as a selection, ref. 195–200). For example, an approximation similar to the one employed in Eq.(5.6) is among the most promising and popular approaches to address spatially-varying blur and so it is worthwhile to keep abreast of progress on that front.

These enhancements, and the many possible others, would serve to further extend the utility of the results presented in this chapter.

# 6. Summary and Future Outlook

> *"I have gotten a lot of results! I know several thousand things that won't work."*
>
> — Thomas Edison

Each chapter of this thesis tackled very different aspects of the challenging endeavour to measure structural dynamics of thin films, so it is important to step back and review the big picture:

Thin films are prevalent in all aspects of technology, and are responsible for making modern electronics as small and cheap as they are today. This is in no small part due to the success of academic research at developing new tools to study and produce thin films, and the insight gained by probing their properties under a variety of circumstances.

Two of such tools played a prominent role in this thesis: transient spectroscopy, and ultrafast electron diffraction (UED). Transient spectroscopy was used in Chapter 2 to begin the exploration into thin film dynamics by investigating the production of graphene via the reduction from an oxidized precursor. The rest of the thesis was devoted to the optimization of UED to study thin films, resulting in a means to measure structural information beyond what is accessible to spectroscopy. In particular, Chapters 3 and 4 presented a low-energy UED setup that was designed to combat the strong space-charge effects that are dominant in the low energy regime. Chapter 5 developed a novel analysis methodology that equips UED with the ability to study irreversible reactions with the ultrafast streaking technique.

These results have left some exciting avenues of research unexplored. For instance, the UED technique has yet to be used to study the reduction of graphene oxide. This would be an ideal candidate to demonstrate the power of the ultrafast streaking technique, since it is an irreversible reaction and significant changes in the diffraction pattern are expected to occur. UED would provide meaningful insight into what is truly happening on the GO surface on a chemical level. For instance, how does the average size of the graphitic domains change during the reduction? And how does the initial oxygen content (either the degree of oxidation or the form of the oxygen-containing moities) influence the reduction dynamics?

Beyond atomic crystals such as graphene, there is an unexplored corner of the two-dimensional world that has potential to further our understanding of life as we know it: biomolecular crystals. While biomolecules themselves are not two-dimensional, many, in particular membrane-bound proteins, form one-molecule-thick monolayer crystals. A perfect example of this is bacteriorhodopsin, a proton-pump that is responsible for converting light into chem-

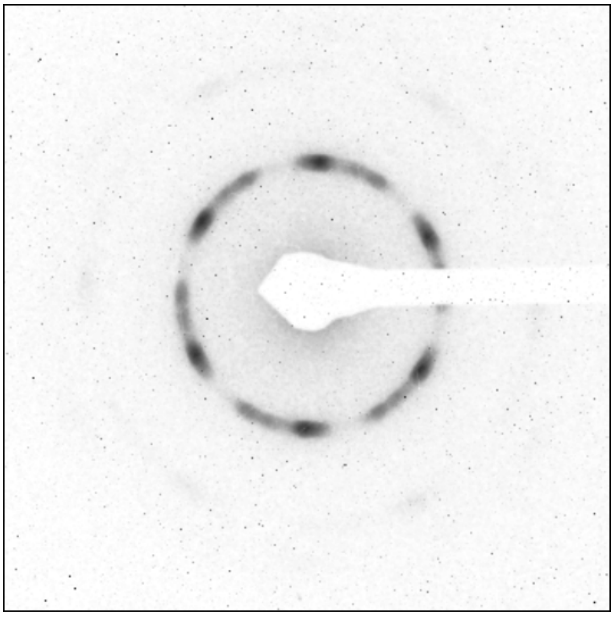

Figure 6.1.: *Ultrafast electron diffraction pattern of a monolayer bacteriorhodopsin crystal, measured at* 90 kV *with a temporal resolution better than* 500 fs.

ical energy in Archaea (see, for example, ref. 201–203). Fig. 6.1 shows a UED image from a monolayer bacteriorhodopsin crystal taken with a 90 kV electron gun*. The presence of the diffraction peaks suggests that performing time-resolved crystallography experiments on membrane-bound proteins is feasible, and that perhaps bacteriorhodopsin is a good first candidate. However, better quality images are required to draw any conclusions about structural changes in such a large and complex molecule. While it is anticipated that the quality of the diffraction images could be improved by using a UED setup that is optimized for monolayer crystals, such as the machine presented in Chapter 3, further development is needed to achieve the $\sim 10$ nm transverse coherence desired to produce sharp diffraction peaks from biomolecular crystals.

While the work presented in this thesis has contributed to the foundation of the exploration of structural of dynamics of thin films, this is merely the beginning of what promises to be an extensive research program. The immense number of monolayer and thin film materials that have been discovered since graphene is astounding, in addition to the plethora of biomolecular crystals, and each deserves to be thoroughly examined for unique physics or potential uses in future technology. Overall, thin films, be they inorganic or biological, present an arduous and exciting frontier which challenges the capabilities of modern technology. But, if it was not for such challenges, the two-dimensional world would remain a fictitious place rather than the daily playground of scientists all over the world.

* Measured at the Miller Group at the University of Toronto; see http://lphys.chem.utoronto.ca/

# Appendices

# A. Practical details of using the discrepancy principle to choose regularization parameters

This section is concerned with using the discrepancy principle to choose the regularization parameter $\mu \geq 0$ in the least squares problem $\hat{\boldsymbol{u}}(\mu) = \arg\min_{\boldsymbol{u}} F(\boldsymbol{u}; \mu)$, where

$$F(\boldsymbol{u}; \mu) = \|\boldsymbol{s} - \boldsymbol{A}\boldsymbol{u}\|_2^2 + \mu \|\boldsymbol{L}\boldsymbol{u}\|_2^2 \tag{A.1a}$$

$$= \|\boldsymbol{s}\|_2^2 + \boldsymbol{u}^T \boldsymbol{A}^T \boldsymbol{A}\boldsymbol{u} - 2\boldsymbol{u}^T \boldsymbol{A}^T \boldsymbol{s} + \mu \boldsymbol{u}^T \boldsymbol{L}^T \boldsymbol{L}\boldsymbol{u} \tag{A.1b}$$

and $\boldsymbol{L}$ is the regularization matrix. The regularized solution thus solves

$$0 = \frac{\partial F(\boldsymbol{u}; \mu)}{\partial \boldsymbol{u}} \tag{A.2a}$$

$$= 2\left(\boldsymbol{A}^T \boldsymbol{A} + \mu \boldsymbol{L}^T \boldsymbol{L}\right)\boldsymbol{u} - 2\boldsymbol{A}^T \boldsymbol{s} \tag{A.2b}$$

and so $\hat{\boldsymbol{u}}(\mu) = \left(\boldsymbol{A}^T \boldsymbol{A} + \mu \boldsymbol{L}^T \boldsymbol{L}\right)^{-1} \boldsymbol{A}^T \boldsymbol{s}$. If $\boldsymbol{L}$ is invertible the substitution $\boldsymbol{u}' = \boldsymbol{L}\boldsymbol{u}$ can be made to rewrite this regularized solution as

$$\hat{\boldsymbol{u}}'(\mu) = \left(\boldsymbol{A}'^T \boldsymbol{A}' + \mu \boldsymbol{I}\right)^{-1} \boldsymbol{A}'^T \boldsymbol{s} \tag{A.3}$$

where $\boldsymbol{A}' = \boldsymbol{A}\boldsymbol{L}^{-1}$.

The discrepancy principle makes use of the knowledge that the measurement is contaminated by an amount $\|\boldsymbol{s} - \boldsymbol{A}\boldsymbol{u}\|_2 = \|\boldsymbol{n}\|_2$, and so the reconstruction is acceptable if

$$\|\boldsymbol{s} - \boldsymbol{A}\hat{\boldsymbol{u}}(\mu)\|_2^2 = \|\boldsymbol{s} - \boldsymbol{A}'\hat{\boldsymbol{u}}'(\mu)\|_2^2 \leq \delta^2 \tag{A.4}$$

where $\delta^2 = \mathbb{E}\left(\|\boldsymbol{n}\|_2^2\right)$ is an estimation of the noise level. Practically, this inequality is implemented by choosing $\mu$ as the zero of the function

$$f(\mu) = \|\boldsymbol{s} - \boldsymbol{A}'\hat{\boldsymbol{u}}'(\mu)\|_2^2 - c^2\delta^2 \tag{A.5}$$

where $c \geq 1$ is a small constant.

There are two issues inhibiting Eq.(A.5) to choose $\mu$: the first is that the obtaining $\hat{\boldsymbol{u}}(\mu)$ from Eq.(A.3) already requires a choice of the value of $\mu$, and the second is finding how to experimentally estimate the noise level $\delta$.

The former point can be addressed by making use of the singular value decomposition (SVD) of $\boldsymbol{A}'$, $\boldsymbol{A}' = \boldsymbol{U}'\boldsymbol{D}'\boldsymbol{V}'^T$, where the diagonal elements $d_i'$ of $\boldsymbol{D}'$ are non-negative and in decreasing order. Using the SVD Eq.(A.3) can be simplified as

$$\begin{aligned}
\hat{\boldsymbol{u}}'(\mu) &= \left(\boldsymbol{A}'^T\boldsymbol{A}' + \mu\boldsymbol{I}\right)^{-1}\boldsymbol{A}'^T\boldsymbol{s} && \text{(A.6a)}\\
&= \left(\left(\boldsymbol{U}'\boldsymbol{D}'\boldsymbol{V}'^T\right)^T\boldsymbol{U}'\boldsymbol{D}'\boldsymbol{V}'^T + \mu\boldsymbol{I}\right)^{-1}\left(\boldsymbol{U}'\boldsymbol{D}'\boldsymbol{V}'^T\right)^T\boldsymbol{s} && \text{(A.6b)}\\
&= \left(\boldsymbol{V}'\boldsymbol{D}'^T\boldsymbol{U}'^T\boldsymbol{U}'\boldsymbol{D}'\boldsymbol{V}'^T + \mu\boldsymbol{V}'\boldsymbol{I}\boldsymbol{V}'^T\right)^{-1}\boldsymbol{V}'\boldsymbol{D}'^T\boldsymbol{U}'^T\boldsymbol{s} \quad \text{since } \boldsymbol{I} = \boldsymbol{V}'\boldsymbol{I}\boldsymbol{V}'^T && \text{(A.6c)}\\
&= \left(\boldsymbol{V}'\left(\boldsymbol{D}'^T\boldsymbol{D}' + \mu\boldsymbol{I}\right)\boldsymbol{V}'^T\right)^{-1}\boldsymbol{V}'\boldsymbol{D}'^T\boldsymbol{U}'^T\boldsymbol{s} && \text{(A.6d)}\\
&= \boldsymbol{V}'\left(\boldsymbol{D}'^T\boldsymbol{D}' + \mu\boldsymbol{I}\right)^{-1}\boldsymbol{V}'^T\boldsymbol{V}'\boldsymbol{D}'^T\boldsymbol{U}'^T\boldsymbol{s} && \text{(A.6e)}\\
&= \boldsymbol{V}'\left(\boldsymbol{D}'^T\boldsymbol{D}' + \mu\boldsymbol{I}\right)^{-1}\boldsymbol{D}'^T\boldsymbol{U}'^T\boldsymbol{s} && \text{(A.6f)}
\end{aligned}$$

Therefore,

$$\begin{aligned}
\|\boldsymbol{s} - \boldsymbol{A}'\hat{\boldsymbol{u}}'(\mu)\|_2^2 &= \left\|\boldsymbol{s} - \boldsymbol{U}'\boldsymbol{D}'\boldsymbol{V}'^T\boldsymbol{V}'\left(\boldsymbol{D}'^T\boldsymbol{D}' + \mu\boldsymbol{I}\right)^{-1}\boldsymbol{D}'^T\boldsymbol{U}'^T\boldsymbol{s}\right\|_2^2 && \text{(A.7a)}\\
&= \left\|\boldsymbol{U}'\boldsymbol{U}'^T\boldsymbol{s} - \boldsymbol{U}'\boldsymbol{D}'\left(\boldsymbol{D}'^T\boldsymbol{D}' + \mu\boldsymbol{I}\right)^{-1}\boldsymbol{D}'^T\boldsymbol{U}'^T\boldsymbol{s}\right\|_2^2 && \text{(A.7b)}\\
&= \left\|\boldsymbol{U}'\left(\boldsymbol{s}' - \boldsymbol{D}'\left(\boldsymbol{D}'^T\boldsymbol{D}' + \mu\boldsymbol{I}\right)^{-1}\boldsymbol{D}'^T\boldsymbol{s}'\right)\right\|_2^2 \quad \text{where } \boldsymbol{s}' = \boldsymbol{U}'^T\boldsymbol{s} && \text{(A.7c)}\\
&= \left\|\boldsymbol{s}' - \boldsymbol{D}'\left(\boldsymbol{D}'^T\boldsymbol{D}' + \mu\boldsymbol{I}\right)^{-1}\boldsymbol{D}'^T\boldsymbol{s}'\right\|_2^2 \quad \text{since } \boldsymbol{U}' \text{ is unitary and so preserves norms} && \text{(A.7d)}\\
&= \left\|\left(\boldsymbol{I} - \boldsymbol{D}'\left(\boldsymbol{D}'^T\boldsymbol{D}' + \mu\boldsymbol{I}\right)^{-1}\boldsymbol{D}'^T\right)\boldsymbol{s}'\right\|_2^2 && \text{(A.7e)}
\end{aligned}$$

Since the matrix $\left(\boldsymbol{I} - \boldsymbol{D}'\left(\boldsymbol{D}'^T\boldsymbol{D}' + \mu\boldsymbol{I}\right)^{-1}\boldsymbol{D}'^T\right)$ is diagonal, the $i^{\text{th}}$ element of the vector $\left(\boldsymbol{I} - \boldsymbol{D}'\left(\boldsymbol{D}'^T\boldsymbol{D}' + \mu\boldsymbol{I}\right)^{-1}\boldsymbol{D}'^T\right)\boldsymbol{s}'$ is

$$\begin{cases} \left(1 - \frac{d_i'^2}{d_i'^2+\mu}\right) s_i' = \left(\frac{\mu}{d_i'^2+\mu}\right) s_i', & \text{if } 0 \leq i \leq \min(k,n) \\ s_i', & \text{if } \min(k,n) < i \leq k \end{cases}$$

where $k \times n$ is the dimension of $\boldsymbol{A}'$. If $q = \min(k,n)$ is introduced, the norm is thus

$$\|\boldsymbol{s} - \boldsymbol{A}'\hat{\boldsymbol{u}}'(\mu)\|_2^2 = \sum_{i=0}^{q-1} \left(\frac{\mu}{d_i'^2+\mu}\right)^2 s_i'^2 + \sum_{i=q}^{k-1} s_i'^2 \tag{A.8}$$

Therefore, the practical implementation of the discrepancy principle is to choose $\mu$ as the zero of the function

$$f(\mu) = \|\boldsymbol{s} - \boldsymbol{A}\hat{\boldsymbol{u}}(\mu)\|_2^2 - c^2\delta^2 \tag{A.9a}$$

$$= \sum_{i=0}^{q-1} \left(\frac{\mu}{d_i'^2+\mu}\right)^2 s_i'^2 + \sum_{i=q}^{k-1} s_i'^2 - c^2\delta^2 \tag{A.9b}$$

Since $f(\mu)$ is monotonically increasing, if it crosses zero then the location of this crossing will be unique. This is important, because it establishes that the discrepancy principle results in a unique choice for $\mu$.

An estimate of the value of the amount of noise, $\delta$, can be made by relating $\delta$ to $\sigma$, the standard deviation of the noise in the streaked diffraction image. The relationship between these two quantities can be arrived at by examining the difference between two streaked images $\boldsymbol{s}^{(1)} = \boldsymbol{A}\boldsymbol{u} + \boldsymbol{n}^{(1)}$ and $\boldsymbol{s}^{(2)} = \boldsymbol{A}\boldsymbol{u} + \boldsymbol{n}^{(2)}$, measured under identical conditions:

$$\mathbb{E}\left(\left\|\boldsymbol{s}^{(2)} - \boldsymbol{s}^{(1)}\right\|_2^2\right) = \mathbb{E}\left(\left\|\boldsymbol{A}\boldsymbol{u} + \boldsymbol{n}^{(2)} - \left(\boldsymbol{A}\boldsymbol{u} + \boldsymbol{n}^{(1)}\right)\right\|_2^2\right) \tag{A.10a}$$

$$= \mathbb{E}\left(\left\|\boldsymbol{n}^{(2)} - \boldsymbol{n}^{(1)}\right\|_2^2\right) \tag{A.10b}$$

$$= \mathbb{E}\left(\left\|\boldsymbol{n}^{(1)}\right\|_2^2\right) + \mathbb{E}\left(\left\|\boldsymbol{n}^{(2)}\right\|_2^2\right) - 2\,\mathbb{E}\left(\boldsymbol{n}^{(2)T}\boldsymbol{n}^{(1)}\right) \tag{A.10c}$$

$$= \delta^2 + \delta^2 - 2\sum_{i=0}^{Q-1} \mathbb{E}\left(n_i^{(2)} n_i^{(1)}\right) \tag{A.10d}$$

$$= 2\delta^2 - 2\sum_{i=0}^{Q-1} \mathbb{E}\left(n_i^{(2)}\right)\mathbb{E}\left(n_i^{(1)}\right) \tag{A.10e}$$

$$= 2\delta^2 \tag{A.10f}$$

The last equality follows from the assumption that each element of each noise vector $\boldsymbol{n}$ is a random variable distributed according to $n_j^{(i)} \sim \mathcal{N}(0, \sigma^2)$, and so $\mathbb{E}\left(n_j^{(i)}\right) = 0$. Additionally,

since $\left\|\boldsymbol{s}^{(2)}-\boldsymbol{s}^{(1)}\right\|_2^2=\left\|\boldsymbol{n}^{(2)}-\boldsymbol{n}^{(1)}\right\|_2^2$ and $n_j^{(2)}-n_j^{(1)}\sim\mathcal{N}(0,2\sigma^2)$, each pixel of the difference image is also normally distributed. This suggests that fitting the histogram of pixel intensities in the difference image is a simple way of experimentally measuring $\sigma$. It follows that the square of the normed difference of the streaked images has a chi-squared distribution, i.e. $\left\|\boldsymbol{s}^{(2)}-\boldsymbol{s}^{(1)}\right\|_2^2\sim 2\sigma^2\chi^2(Q)$. Making use of the fact that $\mathbb{E}\left(\chi^2(Q)\right)=Q$, the relation $\delta=\sqrt{Q}\sigma$ is obtained.

Finally, to relate $\boldsymbol{L}$ to the temporal smoothness regularizer used in Section 5.3 (see Eq.(5.19)), the matrix $\boldsymbol{\Lambda}_{\text{temporal}}=\sum_{i=0}^{M-1}\boldsymbol{\Pi}_i^T\boldsymbol{D}_1^T\boldsymbol{D}_1\boldsymbol{\Pi}_i$ will be introduced such that $\boldsymbol{u}^T\boldsymbol{L}^T\boldsymbol{L}\boldsymbol{u}=\boldsymbol{u}^T\boldsymbol{\Lambda}_{\text{temporal}}\boldsymbol{u}$. Upon inspection it is evident that $\boldsymbol{\Lambda}_{\text{temporal}}=\boldsymbol{\Lambda}_{\text{temporal}}^T$, and so $\boldsymbol{\Lambda}_{\text{temporal}}$ is symmetric. This implies that, in its eigen-decomposition $\boldsymbol{\Lambda}_{\text{temporal}}=\boldsymbol{Q}\boldsymbol{S}\boldsymbol{Q}^T$, where $\boldsymbol{S}$ is diagonal, the eigenvector matrix $\boldsymbol{Q}$ is necessarily unitary. Therefore,

$$\begin{aligned}
\boldsymbol{\Lambda}_{\text{spatial}} &= \boldsymbol{Q}\boldsymbol{S}\boldsymbol{Q}^T && \text{(A.11a)}\\
&= \boldsymbol{Q}\boldsymbol{W}^T\boldsymbol{W}\boldsymbol{Q}^T \quad \text{where } \boldsymbol{W} \text{ is the square root of } \boldsymbol{S} \text{ so that } \boldsymbol{S}=\boldsymbol{W}^T\boldsymbol{W} && \text{(A.11b)}\\
&= \boldsymbol{Q}\boldsymbol{W}^T\boldsymbol{Q}^T\boldsymbol{Q}\boldsymbol{W}\boldsymbol{Q}^T \quad \text{since } \boldsymbol{Q} \text{ is unitary} && \text{(A.11c)}\\
&= \left(\boldsymbol{Q}\boldsymbol{W}\boldsymbol{Q}^T\right)^T\left(\boldsymbol{Q}\boldsymbol{W}\boldsymbol{Q}^T\right) && \text{(A.11d)}
\end{aligned}$$

thus arriving at the decomposition $\boldsymbol{\Lambda}_{\text{temporal}}=\boldsymbol{L}^T\boldsymbol{L}$, where $\boldsymbol{L}=\boldsymbol{Q}\boldsymbol{W}\boldsymbol{Q}^T$.

# Bibliography


[1] M. H. Weik, "Ballistic Research Laboratories Report no. 971: A survey of domestic electronic digital computing systems," tech. rep., United States Department of Commerce Office of Technical Services, Aberdeen Proving Ground, MD, 1955.

[2] E. Rex, "IBM POWER8." *IBM Power Systems*, 2014.

[3] J. Turley, "The two percent solution." *Embedded Systems Design*, December 2002.

[4] M. Dubash, "Moore's Law is dead, says Gordon Moore." *Techworld*, April 2010.

[5] K. S. Novoselov, A. K. Geim, S. V. Morozov, D. Jiang, Y. Zhang, S. V. Dubonos, I. V. Grigorieva, and A. A. Firsov, "Electric field effect in atomically thin carbon films," *Science*, vol. 306, pp. 666–669, 2004.

[6] A. K. Geim and K. S. Novoselov, "The rise of graphene," *Nat. Mater.*, vol. 6, pp. 183–191, 2007.

[7] A. K. Geim, "Graphene: status and prospects," *Science*, vol. 324, no. 5934, pp. 1530–1534, 2009.

[8] C. N. R. Rao, A. K. Sood, K. S. Subrahmanyam, and A. Govindaraj, "Graphene: the new two-dimensional nanomaterial," *Angew. Chem. Int. Ed.*, vol. 48, pp. 7752–7777, 2009.

[9] M. J. Allen, V. C. Tung, and R. B. Kaner, "Honeycomb carbon: a review of graphene," *Chem. Rev.*, vol. 110(1), pp. 132–145, 2010.

[10] V. N. Kotov, B. Uchoa, V. M. Pereira, F. Guinea, and A. H. Castro Neto, "Electron-electron interactions in graphene: current status and perspectives," *Rev. Mod. Phys.*, vol. 84, pp. 1067–1125, 2012.

[11] D. Ahlstrom, "Flat out: being two-dimensional isn't always a bad thing." *The Irish Times*, July 2014.

[12] V. Nicolosi, M. Chhowalla, M. G. Kanatzidis, M. S. Strano, and J. N. Coleman, "Liquid exfoliation of layered materials," *Science*, vol. 340, no. 6139, p. 1226419, 2013.

[13] D. C. Mattis, "How to reduce practically any problem to one dimension," in *Physics in One Dimension* (J. Bernasconi and T. Schneider, eds.), Berlin: Springer-Verlag, 1981.

[14] M. B. Green, J. H. Schwarz, and E. Witten, *Superstring Theory*. Cambridge: Cambridge University Press, 1988.

[15] Z. Hu and X. Lu, "Mechanical properties of carbon nanotubes and graphene," in *Carbon Nanotubes and Graphene* (K. Tanaka and S. Iijima, eds.), Amsterdam: Elsevier, 2014.

[16] X. Wan, Y. Huang, and Y. Chen, "Focusing on energy and optoelectronic applications: A journey for graphene and graphene oxide at large scale," *Acc. Chem. Res.*, vol. 45, pp. 598–607, 2012.

[17] J. C. Polanyi and A. H. Zewail, "Direct observation of the transition state," *Acc. Chem. Res.*, vol. 28, pp. 119–132, 1995.

[18] F. Terova, "Planten un Blomen." Photograph, 2013.

[19] E.-J. Marey, "Des mouvements que certains animaux exécutent pour retomber sur leurs pieds, lorsqu'ils sont précipités d'un lieu élevé," *C. R. Acad. Sci.*, vol. 119, pp. 714–717, 1894.

[20] L. de Broglie, *Recherches sur la théorie des quanta*. PhD thesis, L'Université de Paris, Paris, 1924.

[21] J. R. Dwyer, R. E. Jordan, C. T. Hebeisen, M. Harb, R. Ernstorfer, T. Dartigalongue, and R. J. D. Miller, "Experimental basics for femtosecond electron diffraction studies," *J. Mod. Opt.*, vol. 54(7), pp. 923–942, 2007.

[22] G. Sciaini and R. J. D. Miller, "Femtosecond electron diffraction: heralding the era of atomically resolved dynamics," *Rep. Proj. Phys.*, vol. 74, p. 096101, 2011.

[23] R. J. D. Miller, "Mapping atomic motions with ultrabright electrons: the chemists' Gedanken experiment enters the lab frame," *Ann. Rev. Phys. Chem.*, vol. 65, pp. 583–604, 2014.

[24] R. J. D. Miller, "Femtosecond crystallography using ultrabright electron and x-ray sources: Capturing chemistry in action," *Science*, vol. 343, pp. 1108–1116, 2014.

[25] T. P. Wangler, *RF Linear Accelerators*. New York: Wiley-VCH, 1997.

[26] R. Y. N. Gengler, D. S. Badali, D. Zhang, K. Dimos, K. Spyrou, D. Gournis, and R. J. D. Miller, "Revealing the ultrafast process behind the photoreduction of graphene oxide," *Nat. Comm.*, p. 2560, 2013.

[27] Y. Zhang, Y.-W. Tan, H. L. Stormer, and P. Kim, "Experimental observation of the quantum hall effect and Berry's phase in graphene," *Nature*, vol. 438, pp. 201–204, 2005.

[28] K. S. Novoselov, Z. Jiang, S. V. Zhang, Y.and Morozov, H. L. Stormer, U. Zeitler, J. C. Maan, G. S. Boebinger, P. Kim, and A. K. Geim, "Room-temperature quantum hall effect in graphene," *Science*, vol. 315(5817), p. 1379, 2007.

[29] K. S. Novoselov, A. K. Geim, S. V. Morozov, D. Jiang, M. I. Katsnelson, I. V. Grigorieva, S. V. Dubonos, and A. A. Firsov, "Two-dimensional gas of massless Dirac fermions in graphene," *Nature*, vol. 438, pp. 197–2000, 2005.

[30] N. Tombros, C. Jozsa, M. Popinciuc, H. T. Jonkman, and B. J. van Wees, "Electron spin transport and spin precession in single graphene layers at room temperature," *Nature*, vol. 448, pp. 571–574, 2007.

[31] P. Blake, E. W. Hill, A. H. Castro Neto, K. S. Novoselov, D. Jiang, R. Yang, T. J. Booth, and A. K. Geim, "Making graphene visible," *Appl. Phys. Lett.*, vol. 91, pp. 063124–3, 2007.

[32] K. S. Kim, Y. Zhao, H. Jang, S. Y. Lee, J. M. Kim, K. S. Kim, J.-H. Ahn, P. Kim, J.-Y. Choi, and B. H. Hong, "Large-scale pattern growth of graphene films for stretchable transparent electrodes," *Nature*, vol. 457, pp. 706–710, 2009.

[33] M. Yi and Z. Shen, "A review on mechanical exfoliation for the scalable production of graphene," *J. Mater. Chem. A*, vol. 3, pp. 11700–11715, 2015.

[34] Y. Zhang, L. Zhang, and C. Zhou, "Review of chemical vapor depostion of graphene and related applications," *Acc. Chem. Res.*, vol. 46(10), pp. 2329–2339, 2013.

[35] I. Forbeaux, J.-M. Themlin, and J.-M. Debever, "Heteroepitaxial graphite on 6H-SiC(0001): interface formation through conduction-band electronic structure," *Phys. Rev. B*, vol. 58, p. 16396, 1998.

[36] C. Riedl and U. Coletti, C. Starke, "Structural and electronic properties of epitaxial graphene on SiC(0001): a review of growth, characterization, transfer doping and hydrogen intercalation," *J. Phys. D*, vol. 43(37), p. 374009, 2010.

[37] W. S. Hummers, Jr. and R. E. Offeman, "Preparation of graphitic oxide," *J. Am. Chem. Soc.*, vol. 80(6), p. 1339, 1958.

[38] L. Staudenmaier, "Verfahren zur Darstellung der Graphitsäure," *Berichte der deutschen chemischen Gesellschaft*, vol. 31(2), pp. 1481–1487, 1898.

[39] N. Krane, "Preparation of graphene." University Lecture, http://www.physik.

fu-berlin.de/einrichtungen/ag/ag-reich/lehre/Archiv/ss2011/docs/Nils_Krane-Handout.pdf, 2011. Accessed: 2015-07-04.

[40] A. Lerf, H. He, M. Forster, and J. Klinowski, "Structure of graphite oxide revisited," *J. Phys. Chem. B*, vol. 102, pp. 4477–4482, 1998.

[41] W. Gao, L. B. Alemany, L. Ci, and P. M. Ajayan, "New insights into the structure and reduction of graphite oxide," *Nat. Chem.*, vol. 1, pp. 403–408, 2009.

[42] D. R. Dreyer, S. Park, C. W. Bielawski, and R. S. Ruoff, "The chemistry of graphene oxide," *Chem. Soc. Rev.*, vol. 39, pp. 228–240, 2010.

[43] G. Eda and M. Chhowalla, "Chemically derived graphene oxide: towards large-area thin-film electronics and optoelectronics," *Adv. Mater.*, vol. 22, pp. 2392–2415, 2010.

[44] S. You, L. S. M., T. Szabó, and A. V. Talyzin, "Effect if synthesis method on solvation and exfoliation of graphite oxide," *Carbon*, vol. 52, pp. 171–180, 2013.

[45] S. Park and R. S. Ruoff, "Chemical methods for the production of graphenes," *Nat. Nanotech.*, vol. 4, pp. 217–224, 2009.

[46] C. Gómez-Navarro, J. C. Meyer, R. S. Sundaram, A. Chuvilin, S. Kurasch, M. Burghard, K. Kern, and U. Kaiser, "Atomic structure of reduced graphene oxide," *Nano. Lett.*, vol. 10, pp. 1144–1148, 2010.

[47] V. López, R. S. Sundaram, C. Gómez-Navarro, D. Olea, M. Burghard, J. Gómez-Herrero, F. Zamora, and K. Kern, "Chemical vapor deposition repair of graphene oxide: a route to highly conductive graphene monolayers," *Adv. Mater.*, vol. 21, pp. 4683–4686, 2009.

[48] M. Cheng, R. Yang, L. Zhang, Z. Shi, W. Yang, D. Wang, G. Xie, D. Shi, and G. Zhang, "Restoration of graphene from graphene oxide by defect repair," *Carbon*, vol. 50, pp. 2581–2587, 2012.

[49] R. Rozada, J. I. Paredes, S. Villar-Rodil, A. Martínez-Alonso, and J. M. D. Tascón, "Towards full repair of defects in reduced graphene oxide films by two-step graphitization," *Nano Res.*, vol. 6(3), pp. 216–233, 2013.

[50] S. Pei and H.-M. Cheng, "The reduction of graphene oxide," *Carbon*, vol. 50, pp. 3210–3228, 2012.

[51] H. A. Becerril, J. Mao, Z. Liu, R. M. Stoltenberg, Z. Bao, and Y. Chen, "Evaluation of solution-processed reduced graphene oxide films as transparent conductors," *ACS Nano*, vol. 2(3), pp. 463–470, 2008.

[52] X. Wang, L. Zhi, and K. Mullen, "Transparent, conductive graphene electrodes for dye-sensitized solar cells," *Nano Lett.*, vol. 8(1), pp. 323–327, 2008.

[53] M. C. Kim, G. S. Hwang, and R. S. Ruoff, "Epoxide reduction with hydrazine on graphene: a first principles study," *J. Chem. Phys.*, vol. 131, p. 064704, 2009.

[54] G. Eda, Y.-Y. Lin, S. Miller, C.-W. Chen, W.-F. Su, and M. Chhowalla, "Transparent and conducting electrodes for organic electronics from reduced graphene oxide," *Appl. Phys. Lett.*, vol. 92, p. 233305, 2008.

[55] A. B. Bourlinos, D. Gournis, D. Petridis, T. Szabó, A. Szeri, and I. Dékány, "Graphite oxide: chemical reduction to graphite and surface modification with primary aliphatic amines and amino acids," *Langmuir*, vol. 19, pp. 6050–6055, 2003.

[56] D. A. Sokolov, K. R. Shepperd, and T. M. Orlando, "Formation of Graphene Features from Direct Laser-Induced Reduction of Graphite Oxide," *J. Phys. Chem. Lett.*, vol. 1, no. 18, pp. 2633–2636, 2010.

[57] Y. Zhang, L. Guo, S. Wei, Y. He, H. Xia, Q. Chen, H.-B. Sun, and F.-S. Xiao, "Direct imprinting of microcircuits on graphene oxides film by femtosecond laser reduction," *Nano Today*, vol. 5, no. 1, pp. 15–20, 2010.

[58] Y. Zhou, Q. Bao, B. Varghese, L. A. L. Tang, C. K. Tan, C.-H. Sow, and K. P. Loh, "Microstructuring of graphene oxide nanosheets using direct laser writing," *Adv. Mater.*, vol. 22, no. 1, pp. 67–71, 2010.

[59] P. Kumar, K. S. Subrahmanyam, and C. N. R. Rao, "Graphene patterning and lithography employing laser/electron-beam reduced graphene oxide and hydrogenated graphene," *Mater. Express*, vol. 1, no. 3, pp. 252–256, 2011.

[60] H. Fatt Teoh, Y. Tao, E. Soon Tok, G. Wei Ho, and C. Haur Sow, "Direct laser-enabled graphene oxide-reduced graphene oxide layered structures with micropatterning," *J. Appl. Phys.*, vol. 112, no. 6, p. 064309, 2012.

[61] X.-F. Jiang, L. Polavarapu, S. T. Neo, T. Venkatesan, and Q.-H. Xu, "Graphene oxides as tunable broadband nonlinear optical materials for femtosecond laser pulses," *J. Phys. Chem. Lett.*, vol. 3, no. 6, pp. 785–790, 2012.

[62] S. Prezioso, F. Perrozzi, M. Donarelli, F. Bisti, S. Santucci, L. Palladino, M. Nardone, E. Treossi, V. Palermo, and L. Ottaviano, "Large area extreme-UV lithography of graphene oxide via spatially resolved photoreduction," *Langmuir*, vol. 28, no. 12, pp. 5489–5495, 2012.

[63] C. Petridis, Y.-H. Lin, K. Savva, G. Eda, E. Kymakis, T. D. Anthopoulos, and

E. Stratakis, "Post-fabrication, in situ laser reduction of graphene oxide devices," *Appl. Phys. Lett.*, vol. 102, no. 9, p. 093115, 2013.

[64] D. A. Sokolov, C. M. Rouleau, D. B. Geohegan, and T. M. Orlando, "Excimer laser reduction and patterning of graphite oxide," *Carbon*, vol. 53, pp. 81–89, 2013.

[65] V. Abdelsayed, S. Moussa, H. M. Hassan, H. S. Aluri, M. M. Collinson, and M. S. El-Shall, "Photothermal deoxygenation of graphite oxide with laser excitation in solution and graphene-aided increase in water temperature," *J. Phys. Chem. Lett.*, vol. 1, no. 19, pp. 2804–2809, 2010.

[66] Y. Matsumoto, M. Koinuma, S. Y. Kim, Y. Watanabe, T. Taniguchi, K. Hatakeyama, H. Tateishi, and S. Ida, "Simple photoreduction of graphene oxide nanosheet under mild conditions," *ACS Appl. Mater. Interfaces*, vol. 2, no. 12, pp. 3461–3466, 2010.

[67] K. Subrahmanyam, P. Kumar, A. Nag, and C. Rao, "Blue light emitting graphene-based materials and their use in generating white light," *Solid State Commun.*, vol. 150, no. 37âĂŞ38, pp. 1774–1777, 2010.

[68] L. Huang, Y. Liu, L.-C. Ji, Y.-Q. Xie, T. Wang, and W.-Z. Shi, "Pulsed laser assisted reduction of graphene oxide," *Carbon*, vol. 49, no. 7, pp. 2431–2436, 2011.

[69] L. Guardia, S. Villar-Rodil, J. Paredes, R. Rozada, A. MartÃŋnez-Alonso, and J. TascÃşn, "UV light exposure of aqueous graphene oxide suspensions to promote their direct reduction, formation of graphene-metal nanoparticle hybrids and dye degradation," *Carbon*, vol. 50, no. 3, pp. 1014–1024, 2012.

[70] R. Mukherjee, A. V. Thomas, A. Krishnamurthy, and N. Koratkar, "Photothermally reduced graphene as high-power anodes for lithium-ion batteries," *ACS Nano*, vol. 6, no. 9, pp. 7867–7878, 2012.

[71] S. R. Kim, M. K. Parvez, and M. Chhowalla, "UV-reduction of graphene oxide and its applications as an interfacial layer to reduce the back-transport reactions in dye-sensitized solar cells," *Chem. Phys. Lett.*, vol. 483, pp. 124–127, 2009.

[72] J. I. Paredes, S. Villar-Rodil, A. Martínez-Alonso, and J. M. D. Tascón, "Graphene oxide dispersions in organic solvents," *Langmuir*, vol. 24, pp. 10560–10564, 2008.

[73] D. A. Skoog, F. J. Holler, and T. A. Nieman, *Principles of Instrumental Analysis*. Philadelphia: Hartcourt Brace & Company, 1998.

[74] O. Akhavan and E. Ghaderi, "*Escherichia coli* bacteria reduce graphene oxide to bactericidal graphene in a self-limiting manner," *Carbon*, vol. 50(5), pp. 1853–1860, 2012.

[75] D. Yang, A. Velamakanni, G. Bozoklu, S. Park, M. Stoller, R. D. Piner, S. Stankovish,

I. Jung, D. A. Field, C. D. Ventrice, Jr., and R. S. Ruoff, "Chemical analysis of graphene oxide films after heat and chemical treatments by X-ray photoelectron and micro-Raman spectroscopy," *Carbon*, vol. 47(1), pp. 145–152, 2009.

[76] C. Gómez-Navarro, R. T. Weitz, A. M. Bittner, M. Scolari, A. Mews, M. Burghard, and K. Kern, "Electronic transport properties of individual chemically reduced graphene oxide sheets," *Nano. Lett.*, vol. 7(11), pp. 3499–3503, 2007.

[77] C. Mattevi, G. Eda, S. Agnoli, S. Miller, K. A. Mkhoyan, O. Celik, D. Mastrogiovanni, G. Granozzi, E. Garfunkel, and M. Chhowalla, "Evolution of electrical, chemical, and structural properties of transparent and conducting chemically derived graphene thin films," *Adv. Funct. Mater.*, vol. 19, pp. 2577–2583, 2009.

[78] S. Stankovich, D. A. Dikin, R. D. Piner, K. A. Kohlhaas, A. Kleinhammes, Y. Jia, Y. Wu, S. T. Ngujen, and R. S. Ruoff, "Synthesis of graphene-based nanosheets via chemical reduction of exfoliated graphite oxide," *Carbon*, vol. 45(7), pp. 1558–1565, 2007.

[79] F. Tuinstra and J. L. Koenig, "Raman spectrum of graphite," *J. Chem. Phys.*, vol. 53, pp. 1126–1130, 1970.

[80] C. L. Thomsen, D. Madsen, S. R. Keiding, J. Thøgersen, and O. Christiansen, "Two-photon dissociation and ionization of liquid water studied by femtosecond transient absorption spectroscopy," *J. Chem. Phys.*, vol. 110, pp. 3453–3462, 1999.

[81] R. A. Crowell and D. M. Bartels, "Multiphoton ionization of liquid water with 3.0 – 5.0 eV photons," *J. Phys. Chem.*, vol. 100, pp. 17940–17949, 1996.

[82] M. U. Sander, M. S. Gudiksen, K. Luther, and J. Troe, "Liquid water ionization: mechanistic implications of H/D isotope effect in geminate recombination of hydrated electrons," *Chem. Phys.*, vol. 258, pp. 257–265, 2000.

[83] C. G. Elles, I. A. Shkrob, R. A. Crowell, and S. E. Bradforth, "Excited state dynamics of liquid water: insight from the dissociation reaction following two-photo excitation," *J. Chem. Phys.*, vol. 126, p. 164503, 2007.

[84] J. T. Allan and G. Scholes, "Effects of ph and the nature of the primary species in the radiolysis of aqueous solutions," *Nature*, vol. 126, p. 164503, 1960.

[85] M. J. McAllister, D. H. Li, J.-L. Adamson, H. C. Schniepp, A. A. Abdala, J. Liu, M. Herrera-Alonso, D. L. Milius, R. Car, R. K. Prud'homme, and I. A. Aksay, "Single sheet functionalized graphene by oxidation and thermal expansion of graphite," *Chem. Mater.*, vol. 19, p. 4396, 2007.

[86] A. T. D. Butland and R. J. Maddison, "The specific heat of graphite: an evaluation of measurements," *J. Nucl. Mater.*, vol. 49, pp. 45–56, 1973.

[87] S.-S. Li, K.-H. Tu, C.-C. Lin, C.-W. Chen, and M. Chhowalla, "Solution-processable graphene oxide as an efficient hole transport layer in polymer solar cells," *ACS Nano*, vol. 4, pp. 3169–3174, 2010.

[88] M. Hada, D. Zhang, A. Casadruc, R. J. D. Miller, Y. Hontani, J. Matsuo, R. E. Marvel, and R. F. Haglund, Jr., "Hot electron injection driven phase transitions," *Phys. Rev. B*, vol. 86, p. 134101, 2012.

[89] X. Zou, S. Hovmöller, and P. Oleynikov, *Electron Crystallography: Electron Microscopy and Electron Diffraction*. Oxford: Oxford University Press, 2011.

[90] L. M. Peng, S. L. Dudarev, and M. J. Whelan, *High Energy Electron Diffraction and Microscopy*. Oxford: Oxford University Press, 2004.

[91] P. E. Champness, *Electron Diffraction in the Transmission Electron Microscope*. New York: Taylor & Francis, 2001.

[92] H. Alloul, *Introduction to the Physics of Electrons in Solids*. Berlin: Springer, 2011.

[93] A. Guinier, *X-ray Diffraction in Crystals, Imperfect Crystals, and Amorphous Bodies*. New York: Dover Publications, 1994.

[94] W. H. Bragg and W. L. Bragg, "The reflexion of x-rays by crystals," *Proc R. Soc. Lond. A*, vol. 88, no. 605, pp. 428–438, 1913.

[95] D. B. Williams and C. B. Carter, *Transmission Electron Microscopy: A Textbook for Materials Science*. Berlin: Springer, 2009.

[96] T. van Oudheusden, E. F. de Jong, S. B. van der Geer, W. P. E. M. Op't Root, O. J. Luiten, and B. J. Siwick, "Electron source concept for single-shot sub-100 fs electron diffraction in the 100 keV range," *J. Appl. Phys.*, vol. 102, p. 093501, 2007.

[97] A. Gahlmann, S. T. Park, and A. H. Zewail, "Ultrashort electron pulses for diffraction, crystallography and microscopy: theoretical and experimental resolutions," *Phys. Chem. Chem. Phys.*, vol. 10, pp. 2894–2909, 2008.

[98] A. M. Michalik and J. E. Sipe, "Evolution of non-Gaussian electron bunches in ultrafast electron diffraction experiments: Comparison to analytic model," *J. Appl. Phys.*, vol. 105, p. 084913, 2009.

[99] C. Gerbig, A. Senftleben, S. Morgenstern, C. Sarpe, and T. Baumert, "Spatio-temporal

resolution studies on a highly compact ultrafast electron diffractometer," *New J. Phys.*, vol. 17, p. 043050, 2015.

[100] C. Colliex, "Electron energy-loss spectroscopy imaging," in *Electron Microscopy: Principles and Fundamentals* (S. Amelinckx, D. van Dyck, J. van Landuyt, and G. van Tendeloo, eds.), Weinheim: VCH Verlagsgesellschaft mbH, 1997.

[101] R. Henderson, "The potential and limitations of neutrons, electrons and X-rays for atomic resolution microscopy of unstained biological molecules," *Q. Rev. Biophys.*, vol. 28, pp. 171–193, 1995.

[102] A. Jablonski, F. Salvat, and C. J. Powell, *NIST Electron Elastic-Scattering Cross-Section Database - Version 3.2.* Gaithersburg, MD: National Institute of Standards and Technology, 2010.

[103] S. Tanuma, C. J. Powell, and D. R. Penn, "Calculations of electron inelastic mean free paths. IX. data for 41 elemental solids over the 50 eV to 30 keV range," *Surf. Interface Anal.*, vol. 43, pp. 689–713, 2011.

[104] R. S. of Chemistry, "Periodic Table." http://www.rsc.org/periodic-table, 2015.

[105] W. E. Spicer, "Photoemissive, photoconductive, and optical absorption studies of alkali-antimony compounds," *Phys. Rev.*, vol. 112, p. 114, 1958.

[106] R. Brogle, P. Muggli, P. Davis, G. Hairapetian, and C. Joshi, "Studies of linear and nonlinear photoelectric emission for advanced accelerator applications," *Proceedings of the 1995 Particle Accelerator Conference*, vol. 2, pp. 1039–1042, 1995.

[107] X. Jiang, C. N. Berglund, A. E. Bell, and W. A. Mackie, "Photoemission from gold thin films for application in multiphotocathode arrays for electron beam lithography," *J. Vac. Sci. Technol. B*, vol. 16, p. 3374, 1998.

[108] A. Janzen, B. Krenzer, O. Heinz, P. Zhou, D. Thien, A. Hanisch, F. J. Meyer zu Heringdorf, D. von der Linde, and M. Horn von Hoegen, "A pulsed electron gun for ultrafast electron diffraction at surfaces," *Rev. Sci. Instrum.*, vol. 78, p. 013906, 2007.

[109] M. Aidelsburger, F. O. Kirchner, F. Krausz, and P. Baum, "Single-electron pulses for ultrafast diffraction," *PNAS*, vol. 107(46), pp. 19714–19719, 2010.

[110] H. B. Michaelson, "The work function of the elements and its periodicity," *J. Appl. Phys.*, vol. 48, p. 4729, 1977.

[111] S. Humphries, Jr., *Principles of Charged Particle Acceleration.* New York: Wiley-Interscience, 1986.

[112] D. Zhang, *Femtosecond Structural Dynamics on the Atomic Length Scale*. PhD thesis, Universität Hamburg, Hamburg, 2013.

[113] AS-Photonics, "Snlo." http://www.as-photonics.com/snlo, 2015.

[114] I. H. Malitson, "Interspecimen comparison of the refractive index of fused silica," *J. Opt. Soc. Am.*, vol. 55, pp. 1205–1208, 1965.

[115] A. E. Siegman, *Lasers*. University Science Books, 1986.

[116] F. L. Pedrotti, L. M. Pedrotti, and L. S. Pedrotti, *Introduction to Optics, 3rd edition*. Boston: Addison-Wesley, 2006.

[117] H. D. Young and R. A. Freedman, *University Physics, 11th edition*. London: Pearson, 2004.

[118] K. W. Kolasinski, *Surface Science: Foundations of Catalysis and Nanoscience, 3ed edition*. New York: Wiley-Interscience, 2012.

[119] R. M. Nix, "An Introduction to Surface Chemistry." http://www.chem.qmul.ac.uk/surfaces/scc/. Accessed: 2015-06-27.

[120] P. Musumeci, J. T. Moody, C. M. Scoby, M. S. Gutierrez, H. A. Bender, and N. S. Wilcox, "High quality single shot diffraction patterns using ultrashort megaelectron volt electron beams from a radio frequency photoinjector," *Rev. Sci. Instrum.*, vol. 81, p. 013306, 2010.

[121] H. Liu, A. Karellas, L. J. Harris, and C. J. D'Orsi, "Methods to calculate the lens efficiency in optically coupled CCD X-ray imaging systems," *Med. Phys.*, vol. 21, p. 1193, 1994.

[122] E. I. Gorokhova, V. A. Demidenko, S. B. Mikhrin, P. A. Rodnyi, and C. W. E. van Eijk, "Luminescence and scintillation properties of $Gd_2O_2S$:Tb,Ce ceramics," *IEEE Transactions On Nuclear Science*, vol. 52, pp. 3129–3132, 2005.

[123] H. Graafsma and T. Martin, "Detectors for synchrotron tomography," in *Advanced Tomographic Methods in Materials Research and Engineering* (J. Banhart, ed.), Oxford: Oxford University Press, 2008.

[124] K. Flöttmann, "Astra." http://www.desy.de/~mpyflo/, 2000.

[125] D. H. Dowell and J. F. Schmerge, "Quantum efficiency and thermal emittance of metal photocathodes," *Phys. Rev. ST Accel. Beams*, vol. 12, p. 074201, 2009.

[126] J. R. Dwyer, C. T. Hebeisen, R. Ernstorfer, M. Harb, V. B. Deyirmenjian, R. E. Jordan,

and R. J. D. Miller, "Femtosecond electron diffraction: 'making the molecular movie'," *Phil. Trans. R. Soc. A*, vol. 364, pp. 741–778, 2006.

[127] C. M. Scoby, R. K. Li, and P. Musumeci, "Effect of an ultrafast laser induced plasma on a relativistic electron beam to determine temporal overlap in pump-probe experiments," *Ultramicroscopy*, vol. 127, pp. 14–18, 2013.

[128] P. Musumeci, L. Cultrera, M. Ferrario, D. Filippetto, G. Gatti, M. S. Gutierrez, J. T. Moody, N. Moore, J. B. Rosenzweig, C. M. Scoby, G. Travish, and C. Vicario, "Multiphoton photoemission from a copper cathode illuminated by ultrashort laser pulses in an rf photoinjector," *Phys. Rev. Lett.*, vol. 104, p. 084801, 2010.

[129] H. Park and J. M. Zuo, "Direct measurement of transient electric fields induced by ultrafast pulsed laser irradiation of silicon," *Appl. Phys. Lett.*, vol. 94, p. 251103, 2009.

[130] S. Schäfer, W. Liang, and A. H. Zewail, "Structural dynamics and transient electric-field effects in ultrafast electron diffraction from surfaces," *Chem. Phys. Lett.*, vol. 493, pp. 11–18, 2010.

[131] P. Zhu, Z. Zhang, L. Chen, J. Zheng, R. Li, W. Wang, J. Li, X. Wang, J. Cao, D. Qian, Z. Sheng, and J. Zhang, "Four-dimensional imaging of the initial stage of fast evolving plasmas," *Appl. Phys. Lett.*, vol. 97, p. 211501, 2010.

[132] R.-Z. Li, P. Zhu, L. Chen, T. Xu, J. Chen, J. Cao, Z.-M. Sheng, and J. Zhang, "Investigation of transient surface electric field induced by femtosecond laser irradiation of aluminum," *New J. Phys.*, vol. 16, p. 103013, 2014.

[133] M. M. Murnane, H. C. Kapteyn, and R. W. Falcone, "High-density plasmas produced by ultrafast laser pulses," *Phys. Rev. Lett.*, vol. 62, no. 2, pp. 155–158, 1989.

[134] P. Gibbon and E. Förster, "Short-pulse laser-plasma interactions," *Plasma Phys. Control. Fusion*, vol. 38, p. 769, 1996.

[135] M. Liess and M. Leonhardt, "New operation principle for ultra-stable photo-ionization detectors," *Meas. Sci. Technol.*, vol. 14(4), p. 427, 2003.

[136] R. Paschotta, "Avalanche photodiodes." http://www.rp-photonics.com/avalanche_photodiodes.html. Accessed: 2015-07-16.

[137] C.-D. Lin, *Review of Fundamental Processes and Applications of Atoms and Ions*. Singapore: World Scientific Publishing, 1993.

[138] G. B. Armen, H. Aksela, T. Åberg, and S. Aksela, "The resonant Auger effect," *J. Phys. B: At. Mol. Opt. Phys.*, vol. 33(2), p. R49, 2000.

[139] V. S. Letokhov, *Laser photoionization spectroscopy*. Waltham: Academic Press, 1987.

[140] A. Damascelli, Z. Hussain, and Z.-X. Shen, "Angle-resolved photoemission studies of the cuprate superconductors," *Rev. Mod. Phys.*, vol. 75, p. 473, 2003.

[141] S. J. Bos, S. M. van Leeuwen, and U. Karst, "From fundamentals to applications: recent developments in atmospheric pressure photoionization mass spectrometry," *Anal. Bioanal. Chem.*, vol. 384(1), pp. 85–99, 2006.

[142] F. Xia, T. Mueller, Y.-m. Lin, A. Valdes-Garcia, and P. Avouris, "Ultrafast graphene photodetector," *Nature Nanotechnology*, vol. 4, pp. 839–843, 2009.

[143] M. Furchi, A. Urich, A. Pospischil, G. Lilley, K. Unterrainer, H. Detz, P. Klang, A. M. Andrews, W. Schrenk, G. Strasser, and T. Mueller, "Microcavity-integrated graphene photodetector," *Nano Letters*, vol. 12, pp. 2773–2777, 2012.

[144] B. Y. Zhang, T. Liu, B. Meng, X. Li, G. Liang, X. Hu, and Q. J. Wang, "Broadband high photoresponse from pure monolayer graphene photodetector," *Nature Communications*, vol. 4, p. 1811, 2013.

[145] X. Gan, R.-J. Shiue, Y. Gao, I. Meric, T. F. Heinz, K. Shepard, J. Hone, S. Assefa, and D. Englund, "Chip-integrated ultrafast graphene photodetector with high responsivity," *Nature Photonics*, vol. 7, pp. 883–887, 2013.

[146] R. S. Pantelic, J. W. Suk, C. W. Magnuson, J. C. Meyer, P. Wachsmuth, U. Kaiser, R. S. Ruoff, and H. Stahlberg, "Graphene: substrate preparation and introduction," *J. Struct. Biol.*, vol. 174, no. 1, pp. 234–238, 2011.

[147] R. R. Nair, P. Blake, J. R. Blake, R. Zan, S. Anissimova, U. Bangert, A. P. Golovanov, S. V. Morozov, A. K. Geim, K. S. Novoselov, and T. Latychevskaia, "Graphene as a transparent conductive support for studying biological molecules by transmission electron microscopy," *Appl. Phys. Lett.*, vol. 97, p. 153102, 2010.

[148] C. J. Russo and L. A. Passmore, "Controlling protein adsorption on graphene for cryo-EM using low-energy hydrogen plasmas," *Nature Methods*, vol. 11, pp. 649–652, 2014.

[149] P. F. Zhu, Z. C. Zhang, L. Chen, R. Z. Li, J. J. Li, X. Wang, J. M. Cao, Z. M. Sheng, and J. Zhang, "Ultrashort electron pulses as a four-dimensional diagnosis of plasma dynamics," *Rev. Sci. Instrum.*, vol. 81, no. 10, p. 103505, 2010.

[150] R.-Z. Li, P. Zhu, L. Chen, J. Chen, J. Cao, Z.-M. Sheng, and J. Zhang, "Simultaneous investigation of ultrafast structural dynamics and transient electric field by sub-picosecond electron pulses," *J. Appl. Phys.*, vol. 115, no. 18, p. 183507, 2014.

[151] R. K. Raman, Z. Tao, T.-R. Han, and C.-Y. Ruan, "Ultrafast imaging of photoelectron

packets generated from graphite surface," *Appl. Phys. Lett.*, vol. 95, no. 18, p. 181108, 2009.

[152] J. C. Meyer, A. K. Geim, M. I. Katsnelson, K. S. Novoselov, D. Obergfell, S. Roth, C. Girit, and A. Zettl, "On the roughness of single- and bi-layer graphene membranes," *Solid State Commun.*, vol. 143, pp. 101–109, 2007.

[153] Y.-J. Yu, Y. Zhao, S. Ryu, L. E. Brus, K. S. Kim, and P. Kim, "Tuning the graphene work function by electric field effect," *Nano Letters*, vol. 9, no. 10, pp. 3430–3434, 2009.

[154] R. Saito, G. Dresselhaus, and M. S. Dresselhaus, *Physical Properties of Carbon Nanotubes*. Singapore: World Scientific Publishing, 1998.

[155] L. Reimer and H. Kohl, *Transmission Electron Microscopy: Physics of Image Formation, 5th Edition*. Berlin: Springer, 2008.

[156] W. Witt, "Absolute Präzisionsbestimmung von Gitterkonstanten an Germanium- und Aluminium-Einkristallen mit Elektroneninterferenzen," *Z. Naturforsch. A*, vol. 22A, pp. 92–95, 1967.

[157] K. F. Mak, L. Ju, F. Wang, and T. F. Heinz, "Optical spectroscopy of graphene: From the far infrared to the ultraviolet," *Solid State Commun.*, vol. 152, no. 15, pp. 1341–1349, 2012.

[158] K. Erickson, R. Erni, Z. Lee, N. Alem, W. Gannett, and A. Zettl, "Determination of the local chemical structure of graphene oxide and reduced graphene oxide," *Advanced Materials*, vol. 22, no. 40, pp. 4467–4472, 2010.

[159] J. B. Hastings, F. M. Rudakov, D. H. Dowell, J. F. Schmerge, J. D. Cardoza, J. M. Castro, S. M. Gierman, H. Loos, and P. M. Weber, "Ultrafast time-resolved electron diffraction with megavolt electron beams," *Appl. Phys. Lett.*, vol. 89, p. 184109, 2006.

[160] S. B. van der Geer, M. J. de Loos, E. J. D. Vredenbregt, and O. J. Luiten, "Ultracold electron source for single-shot, ultrafast electron diffraction," *Microsc. Microanal.*, vol. 15(4), pp. 282–289, 2009.

[161] S. Tokita, M. Hashida, S. Inoue, T. Nishoji, K. Otani, and S. Sakabe, "Single-shot femtosecond electron diffraction with laser-accelerated electrons: experimental demonstration of electron pulse compression," *Phys. Rev. Lett.*, vol. 105, p. 215004, 2010.

[162] P. Zhu, Y. Zhu, Y. Hidaka, L. Wu, J. Cao, H. Berger, J. Geck, R. Kraus, S. Pjerov, and Y. Shen, "Femtosecond time-resolved MeV electron diffraction," *New J. Phys.*, vol. 17, p. 063004, 2015.

[163] S. Manz, A. Casandruc, D. Zhang, Y. Zhong, R. A. Loch, A. Marx, T. Hasegawa,

L. C. Liu, S. Bayesteh, H. Delsim-Hashemi, M. Hoffmann, M. Felber, M. Hachmann, F. Mayet, J. Hirscht, S. Keskin, M. Hada, S. W. Epp, K. Flöttmann, and R. J. D. Miller, "Mapping atomic motions with ultrabright electrons: towards fundamental limits in space-time resolution," *Faraday Discuss.*, vol. 177, pp. 467–491, 2015.

[164] A. M. Lindenberg, I. Kang, S. L. Johnson, T. Missalla, P. A. Heimann, Z. Chang, J. Larsson, P. H. Bucksbaum, H. C. Kapteyn, H. A. Padmore, R. W. Lee, J. S. Wark, and R. W. Falcone, "Time-resolved x-ray diffraction from coherent phonons during a laser-induced phase transition," *Phys. Rev. Lett.*, vol. 184, pp. 111–114, 2000.

[165] J. Larsson, A. Allen, P. H. Bucksbaum, R. W. Falcone, A. Lindenberg, G. Naylor, T. Missalla, D. A. Reis, K. Scheidt, A. Sjogren, P. Sondhauss, M. Wulff, and J. S. Wark, "Picosecond x-ray diffraction studies of laser-excited acoustic phonons in InSb," *Appl. Phys. A*, vol. 75(4), pp. 467–478, 2002.

[166] H. Enquist, H. Navirian, T. N. Hansen, A. M. Lindenberg, P. Sondhauss, O. Synnergren, J. S. Wark, and J. Larsson, "Large acoustic transients induced by nonthermal melting of InSb," *Phys. Rev. Lett.*, vol. 98, p. 225502, 2007.

[167] P. Sondhauss, O. Synnergren, T. N. Hansen, S. E. Canton, H. Enquist, A. Srivastava, and J. Larsson, "Metal-like heat conduction in laser-excited insb probed by picosecond time-resolved x-ray diffraction," *Phys. Rev. B*, vol. 78, p. 115202, 2008.

[168] P. Musumeci, J. T. Moody, C. M. Scoby, M. S. Gutierrez, M. Westfall, and R. K. Li, "Capturing ultrafast structural evolutions with a single pulse of MeV electrons: Radio frequency streak camera based electron diffraction," *J. Appl. Phys.*, vol. 108, p. 114513, 2010.

[169] M. Eichberger, N. Erasmus, K. Haupt, G. Kassier, A. von Flotow, J. Demsar, and H. Schwoerer, "Femtosecond streaking of electron diffraction patterns to study structural dynamics in crystalline matter," *J. Appl. Phys.*, vol. 102, p. 121106, 2013.

[170] P. Gallant, P. Forget, F. Dorchies, Z. Jiang, J. C. Kieffer, P. A. Jaanimagi, J. C. Rebuffie, C. Goulmy, J. F. Pelletier, and M. Sutton, "Characterization of a subpicosecond x-ray streak camera for ultrashort laser-produced plasmas experiments," *Rev. Sci. Instrum.*, vol. 71(10), pp. 3627–3633, 2000.

[171] G. A. Naylor, K. Scheidt, J. Larsson, M. Wulff, and J. M. Filhol, "A sub-picosecond accumulating streak camera for x-rays," *Meas. Sci. Technol.*, vol. 12, pp. 1858–1864, 2001.

[172] J. Larsson, "Ultrafast, jitter-free x-ray streak camera that uses single-photon counting," *Opt. Lett.*, vol. 26, pp. 295–297, 2001.

[173] J. Liu, J. Wang, B. Shan, C. Wang, and Z. Chang, "An accumulative x-ray streak

camera with sub-600-fs temporal resolution and 50-fs timing jitter," *Appl. Phys. Lett.*, vol. 82(20), pp. 3553–3555, 2003.

[174] M. M. Shakya and Z. Chang, "Achieving 280 fs resolution with a streak camera by reducing the deflection dispersion," *Appl. Phys. Lett.*, vol. 87, p. 041103, 2005.

[175] J. Feng, H. J. Shin, J. R. Nasiatka, W. Wan, A. T. Young, G. Huang, A. Comin, J. Byrd, and H. A. Padmore, "An x-ray streak camera with high spatio-temporal resolution," *Appl. Phys. Lett.*, vol. 91, p. 134102, 2007.

[176] H. Enquist, H. Navirian, R. Nüske, C. von Korff Schmising, A. Jurgilaitis, M. Herzog, M. Bargheer, P. Sondhauss, and J. Larsson, "Subpicosecond hard x-ray streak camera using single-photon counting," *Opt. Lett.*, vol. 35, pp. 3219–3221, 2010.

[177] P. Musumeci, J. T. Moody, C. M. Scoby, M. S. Gutierrez, and T. Tran, "Rf streak camera based ultrafast relativistic electron diffraction," *Rev. Sci. Instrum.*, vol. 80, p. 013302, 2009.

[178] G. H. Kassier, K. Haupt, N. Erasmus, E. G. Rohwer, H. M. von Bergmann, H. Schwoerer, S. M. M. Coelho, and F. D. Auret, "A compact streak camera for 150 fs time resolved measurement of bright pulses in ultrafast electron diffraction," *Rev. Sci. Instrum.*, vol. 81, p. 105103, 2010.

[179] R. K. Li, W. Huang, Y. Du, L. Yan, Q. Du, J. Shi, J. Hua, H. Chen, T. Du, H. Xu, and C. Tang, "Note: Single-shot continuously time-resolved MeV ultrafast electron diffraction," *Rev. Sci. Instrum.*, vol. 81, p. 036110, 2010.

[180] T. van Oudheusden, P. L. E. M. Pasmans, S. B. van der Geer, M. J. de Loos, M. J. van der Wiel, and O. J. Luiten, "Compression of subrelativistic space-charge-dominated electron bunches for single-shot femtosecond electron diffraction," *Phys. Rev. Lett.*, vol. 105, p. 264801, 2010.

[181] G. H. Kassier, *Ultrafast Electron Diffraction: Source Development, Diffractometer Design and Pulse Characterisation*. PhD thesis, Stellenbosch University, Stellenbosch, 2010.

[182] M. Hirsch, S. Sra, B. Schölkopf, and H. S., "Efficient filter flow for space-variant multiframe blind deconvolution," *23rd IEEE Conference on Computer Vision and Pattern Recognition*, 2010.

[183] T. G. Stockham, Jr., "High-speed convolution and correlation," in *Proceedings of the April 26-28, 1966, Spring Joint Computer Conference*, AFIPS '66 (Spring), (New York, NY, USA), pp. 229–233, ACM, 1966.

[184] D. L. Snyder, R. L. White, and A. M. Hammoud, "Image recovery from data acquired

with a charge-coupled-device camera," *J. Opt. Soc. Am. A*, vol. 10, pp. 1014–1023, May 1993.

[185] W. Feller, *An Introduction to Probability Theory and Its Applications*. Philadelphia: Wiley, 1971.

[186] J.-L. Starck, F. Murtagh, and A. Bijaoui, *Image Processing and Data Analysis*. Cambridge: Cambridge University Press, 1998.

[187] M. Mäkitalo and A. Foi, "Optimal inversion of the generalized Anscombe transformation for Poisson-Gaussian noise," *IEEE Transactions on Image Processing*, vol. 22, no. 1, pp. 91–103, 2012.

[188] R. Vio, J. Bardsley, and W. Wamsteker, "Least-squares methods with Poissonian noise: Analysis and comparison with the richardson-lucy algorithm," *Astronom. and Astrophys.*, vol. 436, pp. 741–755, 2005.

[189] M. Kieweg, H. Gross, T. Sievers, and L. Müller, "Ill-posedness of space-variant image deconvolution," *Proc. SPIE 7800, Image Reconstruction from Imcomplete Data VI*, 2010.

[190] E. T. Jaynes, *Probability Theory: The Logic of Science*. Cambridge: Cambridge University Press, 2003.

[191] V. A. Morozov, "On the solution of functional equations by the method of regularization," *Soviet Math. Dokl.*, vol. 7, pp. 414–417, 1966.

[192] M. Schmidt, "minConf – functions for optimization of differentiable real-valued multivariate functions with simple constraints." http://www.cs.ubc.ca/~schmidtm/Software/minConf.html. Accessed: 2014-06-16.

[193] S. Lahme, C. Kealhofer, F. Krausz, and P. Baum, "Femtosecond single-electron diffraction," *Structural Dynamics*, vol. 1, no. 3, pp. –, 2014.

[194] L. Denis, E. Thiébaut, and F. Soulez, "Fast model of space-variant blurring and its application to deconvolution in astronomy," in *ICIP 2011*, (Bruxelles, France), pp. 2873–2876, Sept. 2011.

[195] S. M. Jefferies and J. C. Christou, "Restoration of astronomical images by iterative blind deconvolution," *Astrophys. J.*, vol. 415, pp. 862–874, 1993.

[196] C. Alard and R. H. Lupton, "A method for optimal image subtraction," *Astrophys. J.*, vol. 503, no. 1, pp. 325–331, 1998.

[197] R. Fergus, B. Singh, A. Hertzmann, S. T. Roweis, and W. T. Freeman, "Removing

camera shake from a single photograph," *ACM Trans. Graph.*, vol. 25, pp. 787–794, July 2006.

[198] J. Bardsley, S. Jefferies, J. Nagy, and R. Plemmons, "A computational method for the restoration of images with an unknown, spatially-varying blur," *Opt. Express*, vol. 14, no. 5, pp. 1767–1782, 2006.

[199] M. Šorel and J. Flusser, "Space-variant restoration of images degraded by camera motion blur," *IEEE Transactions on Image Processing*, vol. 17, no. 2, pp. 105–116, 2008.

[200] A. Levin, Y. Weiss, F. Durand, and W. T. Freeman, "Understanding and evaluating blind deconvolution algorithms," in *IEEE Conference on Computer Vision and Pattern Recognition*, pp. 1964–1971, 2009.

[201] U. Haupts, J. Tittor, and D. Oesterhelt, "Closing in on bacteriorhodopsin: Progress in understanding the molecule," *Annu. Rev. Biophys. Biomol. Struct.*, vol. 28, no. 1, pp. 367–399, 1999.

[202] W. Kühlbrandt, "Bacteriorhodopsin – the movie," *Nature*, vol. 406, pp. 569–570, 2000.

[203] J. K. Lanyi, "Bacteriorhodopsin," *Annu. Rev. Physiol.*, vol. 66, no. 1, pp. 665–688, 2004.